Impact of Solar Resource and Atmospheric Constituents on Energy Yield Models for Concentrated Photovoltaic Systems

Thesis submitted to the Faculty of Graduate and Postdoctoral Studies in partial fulfillment of the requirement for a Master's of Applied Science in Electrical and Computer Engineering.

May 2013

School of Electrical Engineering and Computer Science
University of Ottawa

With Effort And Will, You Can Move Mountains.

Anonymous

ABSTRACT

Global economic trends suggest that there is a need to generate sustainable renewable energy to meet growing global energy demands. Solar energy harnessed by concentrated photovoltaic (CPV) systems has a potential for strong contributions to future energy supplies. However, as a relatively new technology, there is still a need for considerable research into the relationship between the technology and the solar resource. Research into CPV systems was carried out at the University of Ottawa's Solar Cells and Nanostructured Device Laboratory (SUNLAB), focusing on the acquisition and assessment of meteorological and local solar resource datasets as inputs to more complex system (cell) models for energy yield assessment.

An algorithm aimed at estimating the spectral profile of direct normal irradiance (DNI) was created. The algorithm was designed to use easily sourced low resolution meteorological datasets, temporal band pass filter measurement and an atmospheric radiative transfer model to determine a location specific solar spectrum. Its core design involved the use of an optical depth parameterization algorithm based on a published objective regression algorithm. Initial results showed a spectral agreement that corresponds to 0.56% photo-current difference in a modeled CPV cell when compared to measured spectrum.

The common procedures and datasets used for long term CPV energy yield assessment was investigated. The aim was to quantitatively de-convolute various factors, especially meteorological factors responsible for error bias in CPV energy yield evaluation. Over the time period from June 2011 to August 2012, the analysis found that neglecting spectral variations resulted in a ~2% overestimation of energy yields. It was shown that clouds have the dominant impact on CPV energy yields, at the 60% level.

STATEMENT OF ORIGINALITY

Except where stated otherwise, the results presented in this thesis were obtained by the author during the period of his MA.Sc. research under the supervision of Dr. Henry Schriemer. They are to the best of his knowledge original.

ACKNOWLEDGMENTS

Dr. Henry Schriemer: Thank you for your patient guidance, your enduring efforts and your attention to detail in supervising my research and thesis. I couldn't have learnt so much in such short time without your help. I'm most grateful.

Dr. Karin Hinzer: Thank you for your patience, your kindness and understanding. You created an environment where I could learn and thrive. My research was made possible under your enabling administration. Thank you for the motivations, I'm extremely grateful. .

Dr. Joan Haysom: Thank you for your assistance and guidance on the energy yield analysis research. Thank you for the opportunity to manage the APECS data acquisition systems; it gave me a sense of belonging and brought me fulfillment.

Mark Yandt: Thank you for your assistance on the concentrated cell model. Your research provided the basic algorithms I needed to perform most of my energy yield analysis.

Sarah and Mohammed Maliki (Mom and Dad): Thank you so much for everything. Words cannot describe the amplitude of gratitude I have for the opportunities you've given me. I cannot thank you enough for the financial, emotional and psychological assistance you've provided over the years. However, in this circumstance, the least I can write is thank you very much.

TABLE OF CONTENTS

LIST OF FIGURES

LIST OF TABLES

LIST OF ACRONYMS

AM	Air Mass
AM0	Air Mass of extraterrestrial insolation
AM1.5d, AM1.5g	Geometric Air Mass value of 1.5 for the direct and global insolation
AOD	Aerosol Optical Depth
APECS Project	Advancing Photovoltaics for Economical Concentrator Systems
ASTM	American Society for Testing and Materials
CPV	Concentrating Photovoltaic(s)
CWEC	Canadian Weather year for Energy Calculation
CWEEDS	Canadian Weather Energy and Engineering Datasets
DNI	Direct Normal Irradiance
EQE	External Quantum Efficiency
FF	Fill Factor
IQE	Internal Quantum Efficiency
ISO	International Organization for Standardization
IV	Current - Voltage
LCOE	Localized Cost of Energy
OD	Optical Depth
OTF	Optical Transfer Function
PV	Photovoltaic(s)
ROI	Return on Investment
SMARTS2	Simple Model of the Atmospheric Radiative Transfer of Sunshine version 2
SUNLAB	Solar Cells and Nanostructured Devices Laboratory
TMY	Typical Meteorological Year

1 Introduction

Industrialization, social and lifestyle demands are factors responsible for increasing energy requirements. With a global population growth rising at rates faster than 2%, there is a clear need for more energy [1]. Energy supply is expected to be proportional to energy demand, but some issues hamper our capability to generate this required energy. There is environmental concern regarding the contribution of energy supply systems to global warming, pollution, ozone depletion, deforestation and radioactive byproducts. Handling such environmental issues places ethical and political constraints on the energy supply system thereby introducing significant cost increase on energy production [1]. Statistics suggest that human population may increase by a factor of two by the mid twenty-first century [2]. Thus, to maintain global economic and technological development, future demands for energy will certainly increase, with some sources suggesting it might rise by high an order of magnitude by year 2050, about 1.5 - 3 times its current rate [1, 2]. Over the last few decades, many jurisdictions have experienced an increase in the cost of energy resources. An ever increasing energy demand combined with increasing energy costs and natural resource depletion renders future energy production problematic.

To meet future energy demands, our energy supply must minimize the costs due to environmental concerns and the resources used must be sustainable. Sustainability has an intimate relationship with the renewability of the energy resource [1]. Hence, the drive to integrate sustainable and renewable energies into the energy supply diet is a positive step towards preparing a viable future energy budget.

Of all energy sources, our sun is the principal supplier to the earth's energy budget [2] and so is of significant interest in our quest for sustainable energy. Powered by continuous thermonuclear reactions resulting from the fusion of hydrogen atoms, the sun emits an estimated at 3.8×10^{20} MW of light as a black body radiation spectrum [3]. Several terawatts of this energy arrives at the earth's surface, spectrally modified by its propagation through the earth's atmosphere, providing energy that heats the land and seas, feeds the plants by photosynthesis, and fuels other climatic components necessary for life on earth. The solar energy incident on the earth's surface has been identified as a prime source for

sustainable and renewable energy. While the science necessary for harnessing the energy into useful form (electricity and heat) is significantly understood [1], "it is the engineering that is difficult to construct" [2, 4].

Harvesting solar energy with PV technologies for electricity generation presently lacks economic grid parity with non-renewable energy sources, limiting its market applicability. This limitation has temporarily been addressed through subsidy and tariff programs driven by the emerging social consensus on the need to develop the necessary future technologies for sustainable and renewable energies. Photovoltaic technologies have received significant global research attention as well as financial investments over recent years. Optimization procedures are required to minimize the cost of energy produced with PV systems. Geographic and meteorological irregularities are some of the factors that might affect the implementation of PV systems, particularly the concentrating photovoltaic (CPV) systems that are the subject of this thesis. With significantly varying global atmospheric conditions, a "one size fits all" optimization routine may be inappropriate, hence understanding the variability of the incident spectrum with atmospheric and meteorological conditions is necessary. Additionally, since the incident solar resource has a temporal and spatial dependence on atmospheric conditions, understanding the impact of local meteorological conditions on the solar resource is necessary for optimal integration of PV systems into the electrical grid [5, 6].

A key topic of this dissertation are the analyses of the solar resource to determine the effects of local spectral variations on energy yield models used to forecast the generation and distribution of PV energy. The effects of temporal and spatial local conditions, such as cloud cover, temperature, aerosols and perceptible water vapour all affect the incident solar resource. Research tools developed to characterise and measure PV systems are also discussed. A case study for a specific site in Ottawa, Ontario, Canada is used since temporal measurements of the direct normal solar spectrum and sky condition were accessible via the University of Ottawa "Advanced Photonics for Economical Systems" project (APECS).

1.1 Background

In the simplest terms, solar energy can be described as the radiative energy, in the form of light and heat, incident on the earth. Solar energy plays a vital role in the earth's energy

budget – for example, sustaining the food chain by providing plants the light needed for photosynthesis. Harnessing the solar resource for various applications has been a goal over the ages. With ever evolving technologies being developed, recent methods for harnessing solar energy allow for direct efficient conversion of the sun's radiation to heat (solar thermal), and electricity (photovoltaics).

1.1.1 History and Evolution of Photovoltaics

The term "photovoltaics" refers to the use of materials that exhibit the photovoltaic effect, where light (photons) is directly converted into electricity. In most scenarios, the materials used for PV are solid state semiconductors. The discovery of this photovoltaic effect was first made in 1839, and is credited to Edmund Becquerel [7, 8]. Becquerel had illuminated silver-chloride in an acidic solution containing platinum electrodes, observing a photo-voltage and photo-current [8]. The photovoltaic effect requires the separation of an electron-hole pair created by photon absorption, pair recombination occurring after current flow through an electric circuit. This requirement is satisfied by a p-n junction where the separation of electron-hole pairs is achieved by an electric field formed within a depletion region, as shown in Figure 1-1. The physics behind the p-n junction is the basic principle of operation for most modern solid state devices.

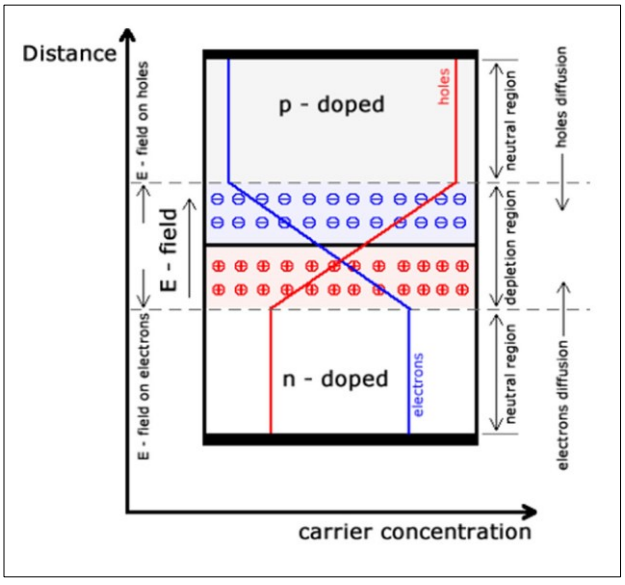

Figure 1-1: A p-n junction in thermal equilibrium and zero bias voltage. Log scaled concentration of electron and hole carriers are represented by the blue and red lines respectively. The two gray regions have neutral charges while the red and blue region are positive and negative charged zones respectively. The direction of flow of the electric field is shown and the direction of the electrostatic forces affecting the diffusion of holes and electrons is illustrated.

A p-n junction is made of two adjacent semiconductor regions with different doping, as diagramed in Figure 1-1. An equilibrium carrier concentration is achieved by diffusion of electrons and holes across the interface, which creates a depletion region maintained by the electric field arising from the exposed donor (n-region) and acceptor (p-region) dopants [9]. Detailed behaviour and characteristics of the p-n junction were first comprehensively understood by William Shockley, and his findings were published by 1949-1950 [10]. Consequently, the understanding of p-n junctions paved the way for growth of the solid state semiconductor industry in developing micro and macro devices such as diodes, transistors and integrated circuits. Exploitation of PV devices advanced more rapidly in the early 1970's when the semiconductor technology had been better understood and methods for design and fabrication of semiconductor devices had advanced significantly [11]. A detailed description of the principles of operation for solar cells is presented in section three of this dissertation.

The literature [12] suggests that silicon PV modules were first designed and fabricated for outdoor use in 1955. This effort was attributed to Bell laboratories in the aim to investigate methods for powering telecommunication systems. These PV modules were restricted to spacecraft applications for about 20 years post 1955 [12]. At this point, the race for terrestrial PV power systems had begun. By the early 1970's, semiconductor technology had advanced enough to allow for the development of very large scale integrated circuits, presaging the development of silicon PV technology for energy use. Increasing demand for electrical energy brought about the re-evaluation of PV systems for terrestrial applications, stimulated rapid development [12]. By 1976, some standardization in the manufacturing of PV modules for terrestrial applications had developed, and PV technology was shown as a viable source of electricity for terrestrial uses in small scale implementations. However, it was also apparent that further development of the silicon PV system was required to improve reliability and efficiency. By 1981, standards had been established for PV module quality control, with the Jet Propulsion Laboratory publishing the first module qualification under the US Department of Energy's (DOE) low-cost solar array program [13]. This set of qualification tests became the de-facto standard following the US government's Block V purchase of modules [11, 14]. Alternative technologies, such as amorphous silicon, cadmium telluride (CdTe) and copper indium diselenide (CIGS)-based solar cells, began to emerge creating a challenge for the utilization of the single qualification standard for all PV modules

[14]. The increased interest and research into PV led to the proposal and implementation of various standards for reliability, safety and qualification for a wider spectrum of PV technologies [13]. Existing standards undergo continuous evolution as technology growth and development occurs. They include the American Society for Testing and Materials (ASTM), and the International Organisation for Standardization (ISO) maintained by the International Electro-technical Commission (IEC) [15].

Despite the relatively poor performance of early PV systems, support continued from government agencies and businesses alike (perhaps influenced by the power crisis of the early 1970's [12]) that perceived solar energy as a clean sustainable and renewable alternative energy resource. By the year 2000, improvements in technology had brought about upgrades in characterization and qualification procedures for PV modules, and the financial value of the industry in the global energy market reached multi-billion dollar values [14, 15]. The average price of solar energy then dropped to $4/W, largely due to increasing system efficiencies and dwindling process cost. Figure 1-2 illustrates the learning curve for solar electric energy cost per watt between 1985 and 2010, projected into the future. Future projection suggests a continuous decrease in cost as the industry continues to mature, but the projection curve is likely to soon trend asymptotic, with suggestions that this may be below $1/W [15–17].

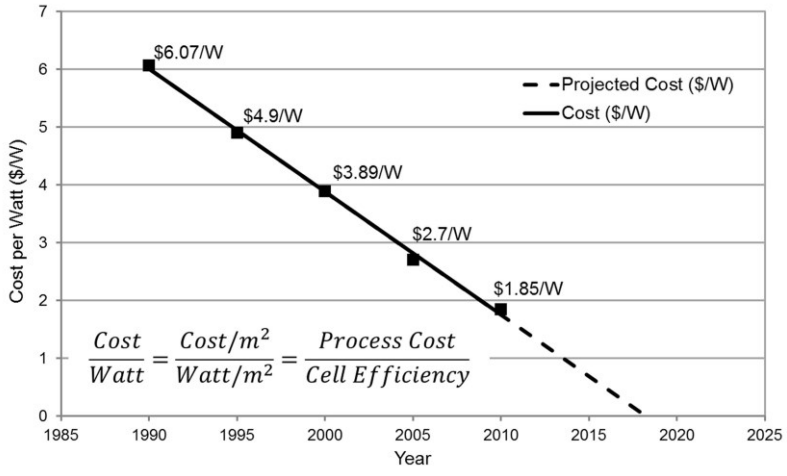

Figure 1-2: Learning curve illustrating cost reduction in installed PV systems between 1990 and 2010. Adapted from [16].

Advances in the design and development of solar cells led to rapid improvements in the conversion efficiency of silicon cells [12] which helped raise expectations for the efficiency

of possible commercial modules. Figure 1-3 illustrates the evolution of commercial silicon modules between 1955 and 2005. The curve indicates the development rate, with a slope variations indicating periods of major breakthrough in silicon cell growth and processing techniques. A burst in improvement is noted in the early 1950s when solar cells were designed for space applications. Another jump is noted in the early 1970s when renewed interest in terrestrial application fueled the research in solar cells. Subsequently, a period of continuous improvement is noted post 1983 [12].

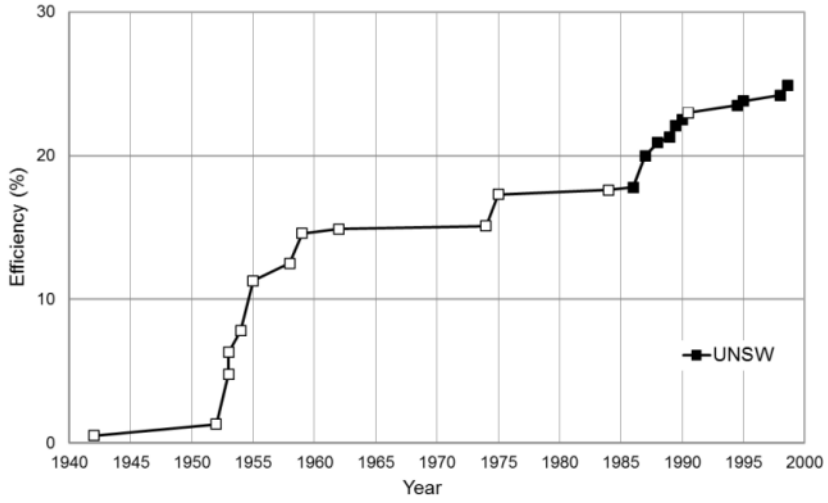

Figure 1-3: Illustration of the evolution of efficiency for silicon cells. The black data points represent data from the University of New South Wales, Australia. Adapted from [12].

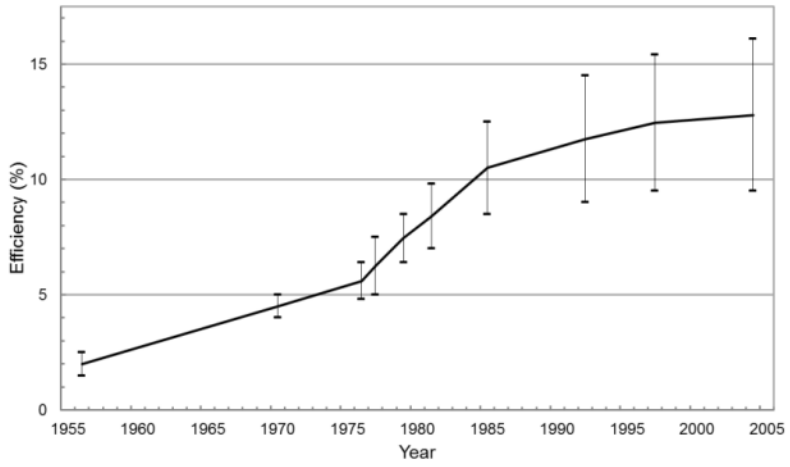

Figure 1-4: Illustration of the evolution of commercial silicon module efficiency. The bars show the upper and lower performance limits of modules commercially available, based on the nominal output of the module as specified by the manufacturer. The solid line is a guide to the eye. Adapted from [12].

Figure 1-4 illustrates the growth of silicon PV module conversion efficiencies between 1940 and 2000. By 1970, high density packaging allowed for nominal module efficiencies of ~4.5% [12], with a reported price of $100/W (1974 Australian dollars). By 1972, a French company (RTC, a subsidiary of Phillips), developed modules with a reported price of US $50/W in small quantities and US$20/W in large quantities. By 1973, a report of prices for modules at US$39/W for 1000 quantities had also been seen [12]. Another report quoted US$20/W for 1000 quantities by 1973 [18]. Following this period, by mid-1970s the US government had begun large scale sponsor programmes [19] and interest had been sparked for terrestrial use of PVs in remote area telecommunications. Consequently, further research led to more reliable modules. By 1975-76, module efficiencies were reported to be between 4.8-6.5%, with module prices of US$20-39/W (1980 dollars) [13, 20]. A "Block II purchase" by the US government between 1976 and 1977 involved modules with efficiencies of 6.0-7.4% with price ranges between US$17-24/W (1980 dollars) [21]. 1978-79 witnessed module efficiencies of 6.5-8.4% with price drops to $US12-18/W (1980 dollars) [13, 20]. By 1980-81, major PV module manufacturers were using a laminated module approach to increase the durability and reliability of modules; and by 1981-85, post "Block V purchase", major modules available exhibited efficiencies above 10%.

By 2005, the photovoltaics industry was on the cusp of exponential growth. Although still expensive due to the high cost of raw materials and relatively low module efficiencies, modules were manufactured in large quantities and their design was made to allow productive operation over twenty year periods. Governments aided this effort in countries like Spain, Germany and the United States of America (USA) by providing lucrative incentives to investors [15]. The provision of incentives was to drive PV technology development to grid parity as rapidly as possible. The cumulative global capacity of PV grew about 50-fold between 2000 and 2011, reaching nearly 70 GW [20]. In southern and eastern Ontario, it has been suggested that PV will reach grid parity by 2018 [20].

In addition to silicon PV technology (which includes mono-crystalline, poly-crystalline and amorphous silicon materials), the quest for cheaper materials and higher module efficiencies led to the development of non-silicon based materials for photovoltaics. Copper indium diselenide and related compounds (which include $CuGaSe_2$, $CuInS_2$ and the alloy $Cu(In, Ga)(S, Se)_2$ known as CIGS) provide a series of thin-film PV technologies with

complex material properties that appeared very promising in the early days of their discovery [14]. The process conditions were very flexible and allowed the establishment of well controlled systems for multisource co-evaporation, which launched CIGS as the fore-runner in thin-film photovoltaics. Current methods for the production of CIGS cells are based on mid-1980s methods developed by ARCO solar which involved the sputtering of metal films with a subsequent selenisation step [12, 16]. The addition of Ga and S helped to increase efficiency [14]. Another thin-film cell technology is based on cadmium telluride (CdTe), which has produced cells with efficiencies of up to 16% and module efficiency of up to 10% [14]. Ongoing research aims to significantly increase the efficiency as it holds great prospects for large scale photovoltaics due to the CdTe material's tolerance to dislocation and its ease of production [14]. The quest for higher efficiencies also brought about the development of tandem cell and concentrating system. By epitaxially stacking solar cells, III-V materials have been successfully used to create multi-junction solar cells (MJSC). Such MJSC typically exploit concentrating optics that deliver high intensity solar irradiation onto the cell, allowing smaller cells to be used and thereby reducing cost [22, 23]. Figure 1-5 below presents the popular NREL illustration of historical and present best research cell efficiencies.

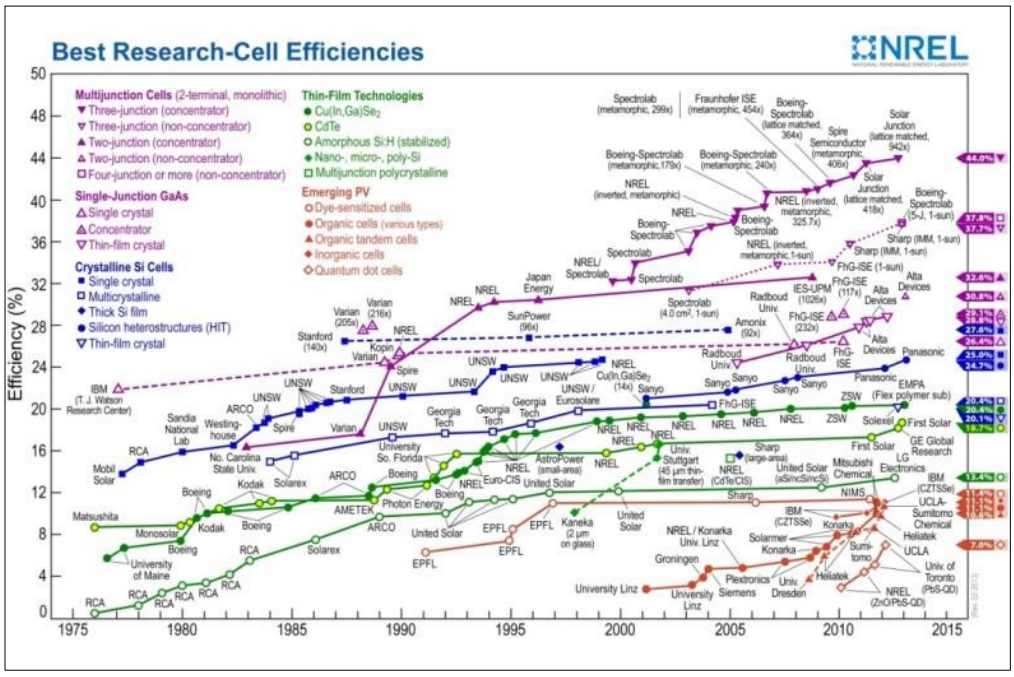

Figure 1-5: NREL's chart of the best research cell efficiencies across various PV technologies over time. Current multi-junction cell technology holds the highest efficiency record of 44% where silicon crystalline cells seem to have

leveled out at a maximum of 27.6% efficiency [24]. The slope of the curve for efficiency growth in multi-junction cells suggests additional efficiency increase is expected in the future.

1.1.2 Renewable Energy for Sustainable Development

Sustainable development as defined by the Brundland report [5] is described as "development that meets the need of the present without compromising the ability of future generations to meet their needs", and it comprises two factors: (1) the concept of need, especially those of the world's poor, and (2) the idea of limitation, which technology and social organization impose on the environment's ability to meet present and future needs [25]. A sense of responsibility towards future generations drives a general consensus, even in fast developing economies, that there is a need to develop sustainably [5]. The increasing global population and the growth of consumption imposes a continued increase in the demand for energy. However, the current dependence on non-renewable sources of energy poses significant issues that contradict the terms for sustainable development. A complementary perspective is given by posing the question of how development can be sustained when fossil and other non-renewable energy resources become depleted. In addition, there is the emission of toxic waste that accumulates for future generations. The degradation of the environment by the deposition of toxic materials has a potential to indirectly hamper the ability of future generations to meet their needs. The choice of energy resource for development determines the ability of society to develop sustainable [26–28]. Hence, to achieve sustainability, we must shift our energy dependence to clean and renewable energies. PV technologies using semiconductor materials to directly convert solar irradiation into electrical energy is one such clean and renewable energy.

1.1.3 A Brief Introduction to PV Systems and their Limitations

Fundamental physics constrains the ability of PV technology to convert incident solar radiation into electrical energy. It is the band gap of the material from which a PV cell is formed that determines the wavelengths of the incident spectrum available for solar absorption. Factors such as carrier recombination, carrier life time and the probability of electron/hole generation via photon excitation in a solar cell provide a basis for determining the theoretical limit for various solar cell technologies. Cell efficiency η is a gauge for performance and it is calculated as the ratio of the electrical power P_{out} generated by the solar

cell to the optical power P_{in} incident upon it, the latter standardized to the irradiance from an AM1.5 spectrum normalized to 1000 W/m^2.

A PV device such as a silicon solar cell produces its electricity by absorption of photons from the solar spectrum with energies above its band-gap; its complex refractive index is $\tilde{n} = n - ik$. The external quantum efficiency (EQE) is the wavelength-dependent function of the ratio of the number of electron-hole pairs collected by the cell to the number of photons of a particular wavelength incident on its exterior. Some of these photons are absorbed (some are reflected) to produce electron-hole pairs, as described in Figure 1-1, but not all pairs contribute to the device current (some pairs recombine). For a single band-gap material, the rate at which photons are absorbed per unit wavelength per area (number/s/m^2/nm) is

$$N_{photons}(\lambda) = \frac{I(\lambda)}{E_{ph}(\lambda)} \times EQE(\lambda) \quad (1)$$

where $I(\lambda)$, the spectral irradiance, is the power per unit wavelength incident per area on the cell (W/m^2/nm), and $E_{ph}(\lambda)$ is the wavelength-dependent photon.

Among the various solar cell technologies, one method for improving cell efficiency involves the use of tandem cells. These comprise multiple band-gap materials that absorb differing portions of the solar spectrum. A common tandem solar cell is formed from III-V semiconductor group materials, with sub-cells of GaInP, InGaAs and Ge. In these solar cells, sub-cells connected by a tunnel junction are stacked in series to increase the overall absorption from the incident solar spectrum. Figure 1-6 illustrates typical EQE measurements for the three sub-cells of a III-V triple junction solar cell (right axis), and the consequent photon flux absorbed (left axis), plotted against wavelength. The reference ASTM G173 AM1.5D spectral irradiance is shown by the solid black curve. For each sub-cell, the spectral energy absorbed is proportional to the EQE and the area each dashed curve yields the sub-cell current.

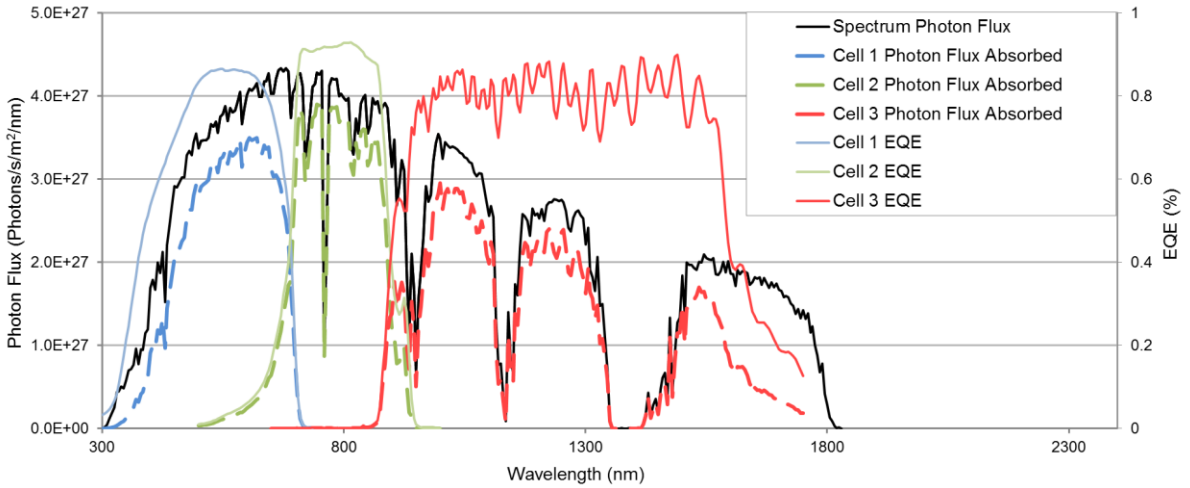

Figure 1-6: Photon flux absorption in proportion to EQE for a sample triple junction solar cell with sub-cells cell 1, cell 2 and cell 3. Each sub-cell is designed to absorb specific portions of the photon flux available depicted by their band-gap thereby increasing efficiency. Sufficiently more sub-cells could be added to further increase efficiency however the selection of materials is limited by their lattice constant.

The band gap of sub-cell materials for such tandem cells determines the range of photon energies available for absorption. For the example in Figure 1-6, sub-cell 1 is a 1.8 eV band gap AlGaInP material, sub-cell 2 is a 1.35 eV band gap InGaAs material with added quantum dots, and sub-cell 3 is elemental Ge with a 0.67 eV band gap. Each sub-cell allows for selective absorption of the incident spectrum; photon energies higher than the band gap of the material are absorbed while lower energies are transmitted to be absorbed by sub-cells with lower band gaps. In this example, cell 1 being the top sub-cell absorbs photon energies greater than 1.8 eV (light with wavelengths below 689 nm), cell 2 being the middle sub-cell absorbs photon energies greater than 1.35 eV (light with wavelengths from 689 – 919 nm) and cell 3 being the bottom sub-cell absorbs photon energies greater than 0.67 eV (light with wavelength from 919 – 1851 nm). Photon energies outside the absorption band of the sub-cells (wavelengths longer than 1851 nm) do not contain enough energy to generate an electron-hole pair in any of the sub-cells. The materials being transparent to these wavelengths, such photons are not harvested and their energies are therefore lost.

Additional losses which limit the performance of semiconductor solar cell materials also occur due to thermalization. This can be described as the loss of energy to phonon emission, or heat, when photons with energies well above the material band gap are absorbed. When photons with energies in excess of the band gap generate electron-hole pairs, the excess energy appears as carrier kinetic energy. The rapid dissipation of this kinetic energy is

known as thermalization, the electrons (holes) coming to rest at the bottom (top) of the conduction (valence) band, heating up the semiconductor lattice. An increase in the semiconductor temperature can also reduce the material band gap. Figure 1-7 illustrates the thermalization process.

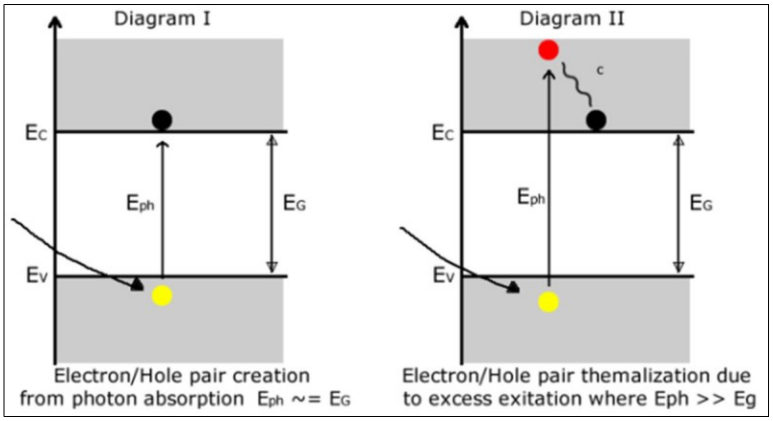

Figure 1-7: Illustration of thermalization of an electron/hole pair. The diagram on the left represents the excitation of an electron/hole from the valence to conduction band where the photon energy Eph is relatively close to the band gap EG. The diagram on the right represents a similar excitation with photon energy greater than the band gap energy. Thermalization occurs and is illustrated as 'c' where the electron/hole pair settles back (thermalize) to the bottom of the conduction band.

A loss mechanism unique to tandem cells, due to the series-interconnected sub-cells, is current mismatch, which manifests as electron-hole recombination (predominantly nonradiative). A tandem cell can be illustrated by a simple circuit diagram having dc power supplies connected in series. For such a circuit, the overall current produced is limited by the power supply producing the least current. Since tandem cells are typically designed for maximal efficiency at a reference spectrum, departures by an incident solar spectrum from this reference may change the current produced by each sub-cell, and thus the tandem cell efficiency. A detailed discussion of the variation in the incident solar spectrum is presented in this thesis.

In all PV systems, loss mechanisms due to the optics that deliver light to the solar cell also reduce system efficiency. For CPV systems, non-imaging lens, focusing mirrors and light-guiding optics are all elements that play a significant role in the overall system performance. Losses arise from such elements as not just direct transmission losses (such as individual Fresnel and absorption losses), but also through their modification of the spectrum transmitted to the tandem cell, as noted above.

1.2 Research Motivation

Motivation for research in photovoltaics is driven globally by the emerging consensus on the need for cleaner renewable energy for sustainable development. Achieving a greener future requires better understanding future energy sources, which in this dissertation is solar energy. A key consideration to effectively harvesting the solar resource is understanding its variation in temporal and spatial dimensions, since these impact the economic decisions driving investment into the technology. Energy yield analysis must be carried out to determine the PV potential of a given site over the investment period. With better the input data, in both time and space, more accurate energy yield models may be constructed.

Persistent increases in population, urbanization and developmental growth combined with modern lifestyles requiring large scale manufacturing, construction and commerce lead to very high energy demands [28] with escalating costs as non-renewable energy sources are depleted. To ensure the availability of energy for future consumption, as well as a safe environment free from pollutants, such costs must be comprehensively understood, and should include such externalities as atmospheric pollutants and greenhouse gases (GHG) emissions. To achieve these goals and mitigate future energy crisis, action must be taken now to develop and utilize alternative renewable and sustainable energy technology such as wind, solar and hydro energy. This need to develop and utilize new technology for energy production provides the essential motivation for researching topics surrounding CPV solar energy systems in this thesis.

The PV industry has long used measured datasets like the Canadian weather energy and engineering datasets (CWEEDS), or simulated data from atmospheric radiative transfer models such as SMARTS2, to provide energy yield estimates within acceptable error margins. Their use has been employed in energy evaluation application packages such as PV Watts and RetScreen. Spatial and temporal variations of atmospheric constituents like aerosols and perceptible water vapour impact the components of the incident solar spectrum (direct and scattered) to various degrees [29], and are of particular interest to CPV research since tandem cells use spectral partitioning to increase efficiency. The cloud sensitivity of CPV systems is considerably higher than that of PV systems, and research suggests that CPV systems may also be more sensitive to spectral variations [30]. Hence, the assumptions which allow PV systems to exploit existing solar resource datasets for accurate energy yield

evaluation may not be true for CPV. This has motivated a study of the characteristics of the local solar resource and drove the implementation of database architecture for acquiring and storing spectral measurements and atmospheric data at 2-minute intervals. The data, from the University of Ottawa's SUNLAB APECS test site, provided the basis for analysing the local spectral sensitivity of energy yield models.

1.3 Thesis Objectives

This thesis addresses four specific objectives: (1) developing software tools for measurement systems; (2) the acquisition of solar spectra, their databasing and analysis; (3) developing faster photovoltaic models; and (4) CPV energy yield analysis. These objectives are described more comprehensively below.

Intuitive software packages enable researchers to perform required tasks in efficient ways, saving time and increasing accuracies by reducing measurement errors. The development of a current-voltage (IV) curve acquisition package was required to allow measurement of IV systems using a Keithley or Kepco power supply with a Spectrolab solar demonstrator (XT-30). Likewise, user-friendly software packages to perform cell spatial uniformity measurements, light source spectral spatial uniformity and cell reliability tests were developed.

A solar test site was instrumented at the University of Ottawa to measure direct normal spectral irradiance, DNI and a range of meteorological conditions. Software and architecture design was required for the collection and storage of highly temporal datasets to promote ease of data retrieval. Data collection was implemented using a dedicated computer system with adequate autonomous software packages capable of acquiring and storing data recorded from the outdoor instruments. The datasets were used for location specific spectral analysis and the evaluation of the local solar resource within the context of local meteorological conditions.

Faster PV models enable assessing very large datasets at minimal cost. Functional simulation concepts have been proposed for PV cells using a single or double diode equivalent circuit model [31, 32]. Conventional methods for implementing such simulations with sequential calculations consume considerable time. An object oriented tuneable PV cell model with parallel programming was developed to ensure result accuracy with exponential

reductions in bulk simulation times. The object characteristics of the PV cell model provide a window for in-depth probes of cell parameters while persistent database storage of the simulated cell model allows for post simulation detailed analysis.

Considering the economics and financing involved, energy yield analysis plays a critical role in feasibility studies for CPV system implementation. Since CPV is sensitive to spectral variation [30], which in turn is impacted by meteorological conditions, an in-depth understanding of the local temporal meteorological effect on CPV energy yield is needed to assist in long term predictive energy yield evaluation for site specific CPV feasibility studies. Using our Ottawa locale as a case sturdy, the measured spectral datasets were compared with other datasets representing historical norms, to constructively quantify the various factors that affect energy yield evaluation. Using detailed CPV models, the energy yield analysis involved temporal characterization of variations between the measured and other datasets determining the overall effect of factors such as cloud cover and aerosols on various CPV architectures, both at the cell and system level.

1.4 Thesis Overview

Five chapters encapsulate the main contents of this dissertation. Chapter one has presented an introduction to the background of PV systems from an historical perspective, noting both the need to develop and utilize sustainable and renewable energy sources and the challenges faced in their realization. An historical evolution of PV systems was presented, and the basic physical and practical limits to its implementation were highlighted. The introduction provides the background for discussions of various factors affecting PV energy production and usage, such as the solar resource and its relationship with the local atmospheric or meteorological conditions and the economics involved in the implementation of grid connected PV systems.

Chapter two discusses issues that relate to PV and CPV systems, reviewing the fundamentals behind the nature of the incident solar resource. It focuses on the atmospheric absorptive components responsible for altering the extraterrestrial black body spectral profile. Here, a “Simple Model of the Atmospheric Radiative Transfer of Sunshine version 2” (SMARTS2), is exploited to simulate the spectral distribution and power of the solar resource. An overview of the APECS test site at the University of Ottawa is given,

presenting the data acquisition system and maintenance procedures for quality control of the recorded dataset.

In chapter three, instruments and software tools developed for characterising and testing CPV systems at the University of Ottawa's SUNLAB research lab are discussed within the context of their development, operation and results. A single diode model, based on publications by Sakurada and Varshni [31, 32], is presented and discussed. Their theory was used to develop a java application, which utilized object oriented programming techniques, to model PV cell response. The java application utilizes parallel programming and database storage methods to speed up simulation time and allow storage of runtime results for recurrent post analysis.

In chapter four, an algorithm to reconstruct the spectral distribution of the solar irradiance from parameterised aerosol optical depth data (taken from measured irradiance) is presented. Data gathered from the measuring instruments on the APECS test site, historical data and typical meteorological data was used in the model. A comprehensive approach was taken to quantitatively de-convolute temporal effects that may affect long term CPV energy yield analysis, such as meteorological variations, atmospheric aerosols and air-mass. A case sturdy was performed for the APECS test site using the measured temporal spectral DNI data sets. Using PV system simulation software introduced in chapter 3, constructive and deconstructive comparisons were carried out on various energy yield recipes.

In chapter 5, the simulations, models and results are summarized. The advantages of the systems developed in chapter 4 are discussed and their practical limitations are highlighted. Suggestions for further investigation are proposed in the context of sustainable renewable energy.

2 The Solar Resource

To effectively analyse energy production in PV systems, modelling and simulation of the solar resource is necessary. In this chapter, the fundamentals of the solar radiation incident on the earth's surface are described, and the relationship between the earth's movement and observed solar radiation is explained in terms of its spectral distribution. Calculation of the solar azimuth and elevation angles is necessary for crude tracking in dual axis trackers which is necessary for CPV system implementation. The algorithms presented in this section explain the equations to derive temporal solar azimuth and elevation.

2.1 Introduction

The sun is the central energy generator within the earth's solar system [33]. It is a class G2-V yellow dwarf star having a radius of 6.96 x 10^7 km. Nuclear fusion of hydrogen at its centre produces radiant energy with helium as a waste by-product. The mean radiation intensity from the surface of the sun is 2.01x10^7 ($Wm^{-2}sr^{-1}$) for an integrated total of 2.85 x 10^{26} W [34]. A small portion of this solar energy arrives at the earth's surface making life possible on the planet. All natural cycles necessary for life on earth which include rain, wind, photosynthesis and ocean current are directly or indirectly driven by the solar radiation incident on the earth.

The energy from the sun is radiated by its corona at an effective blackbody temperature of about 5800 K. At the mean Earth-Sun distance, the sun subtends a solid angle of 9.24 milliradians (or 0.53˚), thus the sun is truly not a point light source and the sun rays are not truly parallel [34]. For the given portion of the solar energy received by the earth, the mean distance between the earth and sun of 1.50 x 10^9 km limits the power of the radiation reaching the top of the earth's atmosphere to about 1366.1 Wm^{-2} ± 7.0 Wm^{-2}. The elliptical nature of the earth's orbit causes variations in the distance between the earth and sun (the Earth's radius vector) to the tune of about 3.39% [34]. This distance is from the perihelion where the distance is closest to the aphelion where the distance is farthest. The variation in distance causes an inversely proportional variation in solar radiation intensity received at the top of the earth's atmosphere denoted by $1/R^2$, where R is the radius vector or mean earth-sun distance. For this reasons, the solar radiation intensity varies annually from December (1414

Wm^{-2}) to July (1321 Wm^{-2}). Complementary causes for variation in the incident solar intensity at the top of the earth's atmosphere include variations in brightness of the sun, sunspot cycle and solar oscillations. Where calculations of the solar resource incident on the earth's atmosphere (the extraterrestrial irradiance) are required, adequate corrections are incorporated to address these fluctuations. The total annual energy received from the sun on the earth's surface is estimated to be about 1.5 x 10^{18} kWh which is more than the global energy need in the year 2000 (~10^{14} kWh/a) [33] by a factor of 1500.

Solar energy incident on the earth's surface has been attenuated by the atmosphere which contains gaseous and aqueous molecules that absorb solar radiation as a function of frequency. Diffraction, reflection and partial transmission by atmospheric constituents splits the solar irradiance into several components that exhibit distinctive characteristics and relationship. These components include the direct beam, global horizontal and global diffuse irradiance. A range of simple to complex algorithms exists for modeling the atmospheric radiative transfer of sunshine to estimate the various irradiance components. For the various configurations for acquiring irradiance data, plane transfer algorithms also exist for modelling sunshine observations at various planes.

The period and duration of sunshine depends on factors such as geographical location and weather conditions. The amount of radiation incident yearly varies for various belts of the planet. Locations at the northern and southern hemisphere generally receive less radiation when compared to sub and middle belt areas. Measuring the solar irradiance incident on the earth's surface requires a plethora of instruments in various configurations to cover the irradiance components. The spectral distribution of solar radiation is measured with spectroradiometers sensitive to wavelengths between 280 and 4000 nanometers. Pyrheliometer and pyranometer instruments are designed for absolute measurements of the direct beam and global horizontal components respectively.

2.2 Earth and Sun

Electromagnetic radiation from the sun spans the electromagnetic spectrum, from X-rays and gamma rays ranging to very long wavelength radio waves. In the context of this dissertation, the range of wavelengths will be restricted to spectral regions relevant for CPV systems,

namely that between the ultraviolet (UV, beginning at 280 nm) and the near infrared (NIR, ending at 4000 nm).

2.2.1 The Earth's Incident Solar Radiation

The sun is a black body radiator whose surface temperature is approximately 5800 K. The sun has a spectral emission that can thus be characterised by the Stefan-Boltzmann and Planck Radiation Law. The Stefan-Boltzmann law, a relation which describes the power radiated from the black body as a function of its surface temperature is given as

$$Q = \varepsilon\sigma A T^4 t\,, \tag{2}$$

where Q is the energy flux density, ε is the emissivity for the emitting surface, σ is the Stefan-Boltzmann constant $= 1.3806 \times 10^{-23}$ (J K^{-1}), A is the area of the emitting surface in meters, T is the temperature of the surface in Kelvin, and t is the time in which the black body is observed in seconds.

Planck's Radiation Law describes the electromagnetic radiation emitted from a black body at thermal equilibrium for any given temperature as

$$E(\lambda, T) = \frac{2\pi hc^2}{\lambda^5}\left(\frac{1}{e^{\frac{hc}{\lambda\sigma T}}-1}\right)\quad, \tag{3}$$

where E is the spectral irradiance or radiant flux per unit area which is a function of wavelength λ and the absolute temperature T, h is Plank's constant a 6.626196×10^{-34} (J s) and c is the speed of light.in vacuum constant at 2.9979250×10^{8} (ms^{-1}). Using these equations, substituting the appropriate values for the sun, the overall power incident on the earth's atmosphere can be deduced. The Planck theory provides a first approximation to the spectral distribution of the sun [34].

Research suggests that the sun is not a perfect radiator nor is it of uniform composition. In estimates, the sun is elementally composed of 92% hydrogen and 7.8% helium. A smaller fraction of the sun to the tune of 0.2% is made up of a mix of about 60 other elements which are mainly metals such as iron, magnesium, chromium, carbon and silicon [35, 36]. Knowing this, advanced models have been developed to predict its spectral irradiance. One such model has been developed by Kurucz [35, 37, 38] who used elemental compositions to compute the spectral irradiance at relatively high resolution. He predicted a significant departure from the black body radiation.

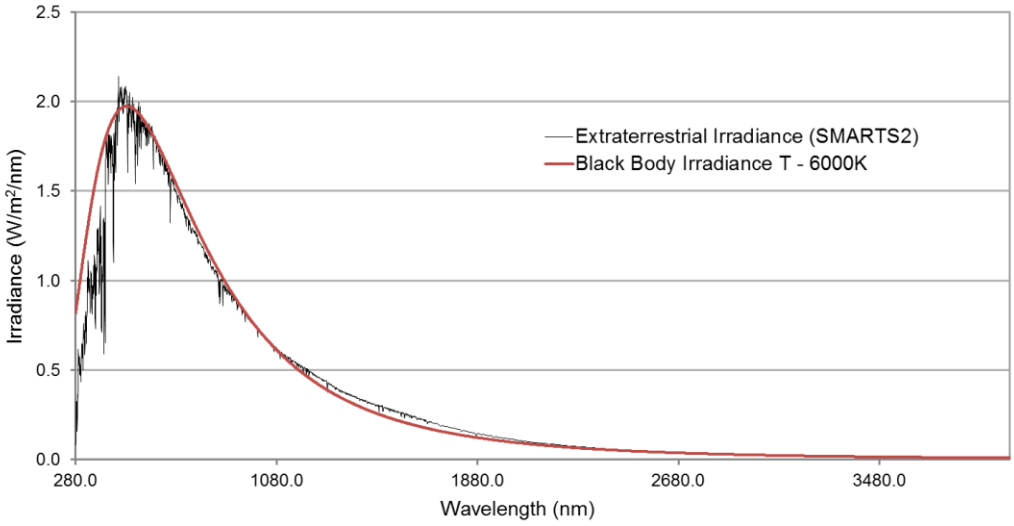

Figure 2-1: Simulated values for extraterrestrial irradiance at the top of the earth's atmosphere taken from SMARTS2, plotted against a "perfect" black body radiation based on the Planck's radiation law with a temperature of 6000K.

Figure 2-1 presents a simulated low resolution extraterrestrial (ETR) spectrum contrasted with an ideal black body radiation spectrum based on the Planck function for a temperature of 6000 K. At specific wavelengths in the infrared region beyond 2 μm, it should be noted that the differences are minimal between the two spectra. Significant differences at the shorter wavelengths are a result of partial absorption of radiation largely arising from the various constituents of the sun earlier discussed. Each unique elemental constituent of the sun absorbs the spectrum with a specific characteristic; hence lines or bands are noted in the resultant spectrum which corresponds to absorption by unique materials. These lines, first observed by Fraunhofer, are named after him [34].

2.2.2 Earth-Sun Temporal Coordinates

As mentioned previously, solar radiation from the sun incident on the top of the earth's atmosphere is referred to as the extraterrestrial radiation. Varying sun-earth distance due to the revolution of the earth on its elliptical orbit, among other factors determines the power of the incident extraterrestrial radiation. For the purpose of describing the solar resource available on earth and its periodic temporal variability, it is therefore important to understand the movement of the earth in relation to the sun.

Gravitational forces between the sun and the earth keep the earth revolving around the sun on an elliptical path known as the earth's orbit. The earth is tilted on an axis

approximately 23.44˚ relative to its orbital plane. In the month of June, the position of the earth on its elliptical orbit is such that the earth is at its farthest distance from the sun (summer solstice), and due to the earth's axial tilt, the northern hemisphere is pointed away from the sun in December and towards the sun in June. In the months of March and September, the northern hemisphere is neither pointing to nor away from the sun (equinoxes). The periodic nature of the earth's revolution around the sun allows for specific recurrent date periods where the earth is farthest, closest or at specific positions relative to the sun. The winter solstice (December 22nd), summer solstice (June 21st), spring equinox (March 21st) and fall equinox (September 23rd) denote specific date periods in the earth orbital cycle where the earth-sun relative position is of interest.

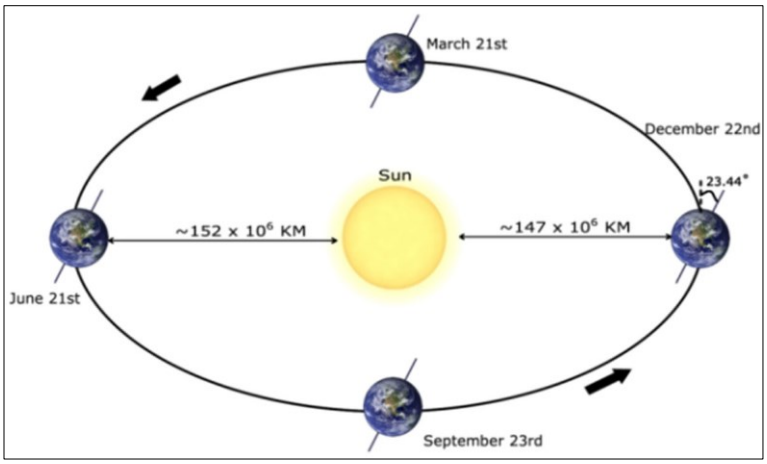

Figure 2-2: The earth's elliptical orbit around the sun (exaggerated), showing an axial tilt of about 23.44˚ relative to the elliptical orbital plane. The northern hemisphere points away and towards the sun at the winter and summer solstice respectively while the earth's axis is perpendicular to its orbit in the spring and fall equinox. The four periods in the year as illustrated correspond to the four seasons.

From a fixed point on the earth's surface, the relative axial and orbital movements of the earth correspond to an observed apparent movement of any given celestial body. For example, an observation of the sun from a stationary point on the earth shows that the sun appears to revolve around the earth. However, due to the tilt of the earth on its axis, this observed movement follows a parabolic path. The observed velocity of the sun follows the earth's rotation. Hence, the position of the sun can be denoted at any given time and location from its horizontal and vertical angular coordinates. Right ascension is the former, and it is measured eastward along the celestial equator from the vernal equinox, in either hours or degrees; the declination angle is the latter, and it is measured north (positive) and south (negative) of the celestial equator. By direct substitution, an hour corresponds to a 15˚

movement of the sun along its right ascension. Consequently, at those times during the earth's revolution where the orbital plane intersects the equatorial plane, the declinations of the sun are equal to zero. Figure 2-3 shows the celestial sphere that illustrates these positions.

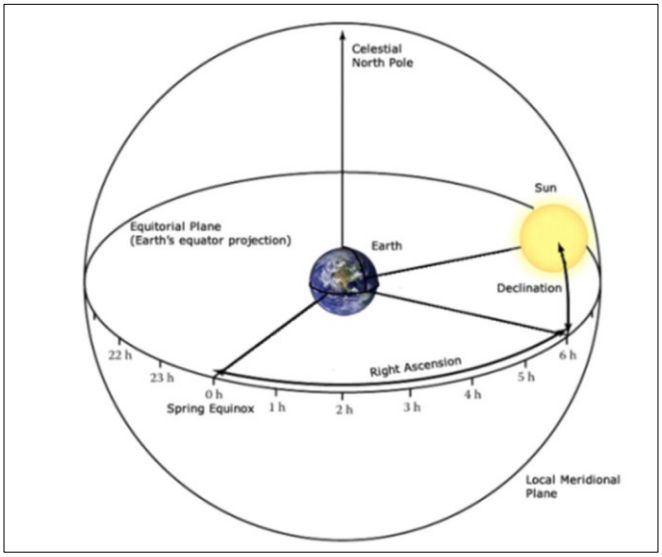

Figure 2-3: A representation of the earth's celestial sphere. The equatorial plane is a projection of the earth's celestial equator to a position in space. The earth's rotational axis forms the celestial North and South poles when extended. The diagram illustrates a right of ascension of 6 hours, or 90° for the sun (Adapted from [39], page 10).

At any given time of the year, the declination can be calculated as

$$\delta = 23.45^{\circ} sin^{-1}\left\{sin(23.45^{\circ}) sin\left[\frac{360}{365}(d - 81)\right]\right\} \quad , \tag{4}$$

where d is the day of the year with January 1st as day 1. Equation (4) is valid for all non-leap years and may be adapted for a leap year by replacing 365 with 366. The celestial sphere (Figure 2-3) must be tilted to adjust for the offset in the celestial north and south poles due to the observer's latitudinal position, as shown in Figure 2-4. It should be noted that for different latitudinal positions, the closer an observer is to the equator (Latitude 0°), the closer the equatorial plane is to the zenith (perpendicular plane to the observer's location) [39]. Hence, for an observer positioned geographically on the equator, the sun would appear to travel directly overhead on the spring and fall equinox where the earth's axis is perpendicular to the earth's orbit. The local meridional plane runs through the earth's axis of rotation as shown in Figure 2-3 and Figure 2-4 and is perpendicular to the local East-West axis synonymous to the longitudinal axis. It is defined by the three directions, due north, due south and the zenith. To determine the sun's coordinates from local earth positions, a combination of parameters must be used to determine right ascension and declination. These

parameters include the observer's latitude and longitude and the local time (as discussed below).

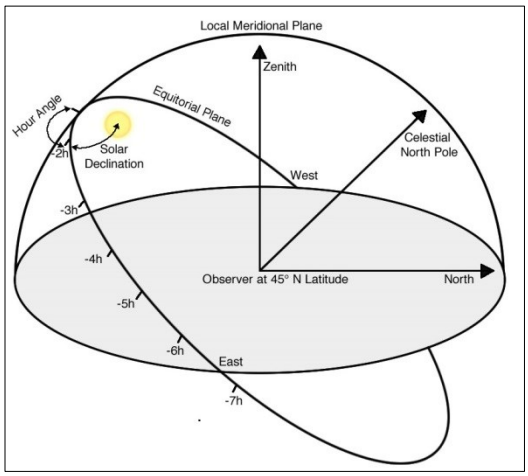

Figure 2-4: Relation of solar angles from an observer's perspective as seen in the northern hemisphere at 40° N. The north and south directions are in the plane of the page. The east and west directions are out of and into the page respectively. The zenith line is perpendicular to the earth's surface. The local meridional plane is the plane of the page and is defined by the north, south and zenith points. The equatorial plane is perpendicular to the polar axis about which the celestial sphere rotates. The solar hour angle, ha, is the angle between the sun's current position and the solar noon that is due south and measured along the equatorial plane in hours (about -2 hours in this Figure). (Adapted from [39]).

The solar hour angle ha denotes the difference between the current position (right ascension) of the sun and its highest position for the day (known as the solar noon). It is calculated due south and measured in hours along the equatorial plane as shown in Figure 2-4. The hour angle is measured in units of time and is used to specify how long it will take for the sun to reach the solar noon or how long ago since the sun reached the solar noon. For each revolution of the earth along its axis, considering the relative motion of the sun observed by an observer at a fixed location on earth, as previously discussed, the earth rotates at a rate of 15° per hour and the equivalent hour angle correspondent to a 15° rotation is one hour. For times prior to solar noon, the hour angle is negative, while for times after the solar noon, hour angle is positive. Solar noon is that point where the apparent sun's path intersects the local meridional plane. At this point, the hour angle is zero. From Figure 2-4, it is seen that the sun lags solar noon by 2 hours, that is, $ha = -2$

To accurately employ the apparent position of the sun, corrections must be made to adjust for the behaviour of the earth's motion around the sun. To quantify this, we carefully consider the rotation of the earth as it revolves around the sun. This rotation occurs at a virtually constant rate due to the earth's conservation of angular momentum [39]. We define

the mean *solar day* as that minimum time interval for which the sun appears over the same meridian, defined to be equal to 24 hours. This is in contrast to the *sidereal day* which uses a distant star, rather than the sun, as a fixed reference. With reference to the distant star, the motion of the earth in its orbit is negligible, so the earth rotates 360˚ in one sidereal day. Because the earth rotates in the same direction as it revolves around the sun (prograde rotation), there are one fewer solar days per year than there are sidereal days and hence the earth rotates more than 360˚ in one solar day. Thus, one sidereal day is about 23 hours, 56 minutes, 4.1 seconds long, about 4 minutes shorter than a solar day.

Due to the elliptical nature of the earth's orbit, the earth's revolution proceeds fastest when the bodies are closest. Since a day is fixed at 24 hours, consequently, for every true solar noon when the sun's path cuts through the local meridional plane, the relative local clock time would be different. The deviation of true solar noon from that stipulated by local time is expressed by the *equation of time* as [40]

$$E = 0.000075 + 0.0019\cos\beta - 0.0321\sin\beta - 0.0146\cos 2\beta - 0.0409\sin 2\beta, \quad (5)$$

$$\text{with } \beta = \frac{2\pi n}{365}, \quad (6)$$

where n is the day number with January 1st as day 1. Equation (5) provides a daily value that denotes how many minutes the sun is behind or ahead of the local meridian at solar noon. For example, the local meridian at Ottawa, Ontario Canada is about 75.69˚W which is 4 hours west of the Greenwich meridian (0˚ longitude). On January 1st, equation (5) produces a result of $E = -3.75$ minutes, meaning that the actual solar noon is 3.75 minutes after local noon.

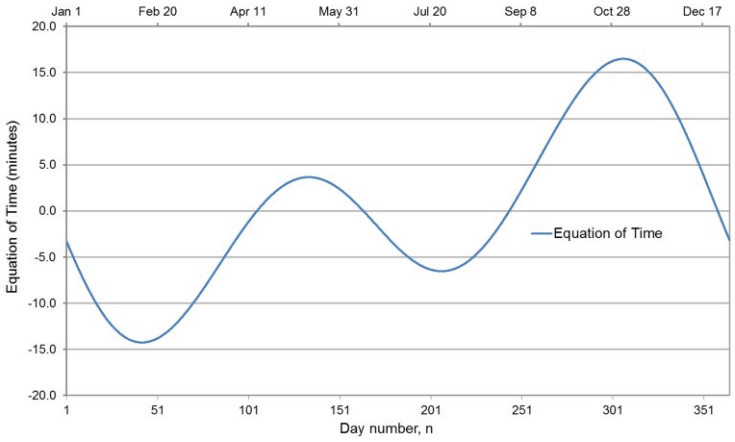

Figure 2-5: Illustration of the equation of time in Ottawa, Canada for the duration of a year. Adjustments have been made to cater for the earth's tilt angle and its noncircular orbit around the sun.

For every fixed observation point on the earth's surface, a combination of the earth's tilt and its orbital revolution gives a unique relationship between the solar declination and the hour angle. When plotted out over the year, this provides the solar analemma. Figure 2-6 presents the solar analemma for a position in Ottawa, Ontario, Canada.

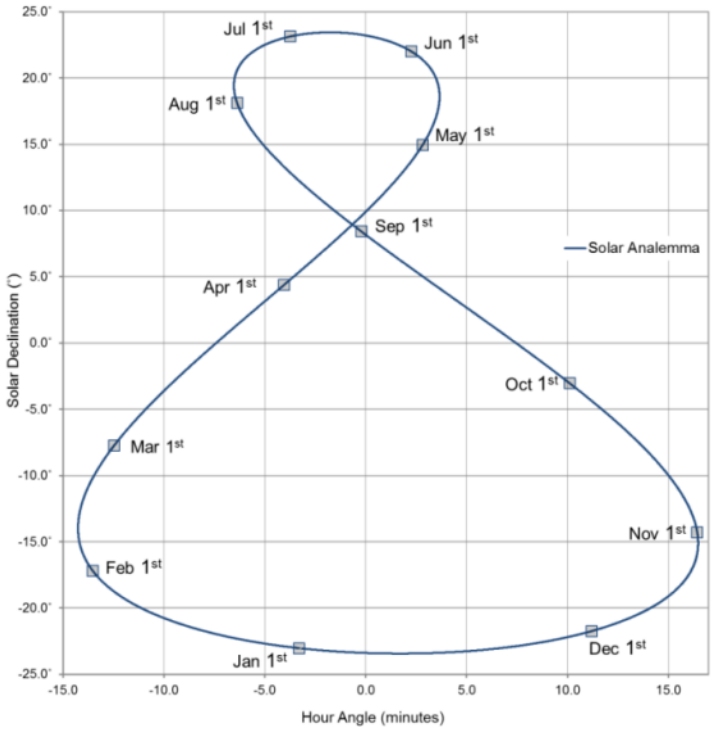

Figure 2-6: Solar analemma for Ottawa, Canada with coordinates of approximately 45˚N and -75˚W. Solar declination is plotted against the equation of time.

2.2.3 Solar Elevation and Azimuth

The previous section introduced the relationship between the movement of the earth about its axis and its orbit around the sun; this section discusses the coordinate system used for referencing or defining the position of the sun with respect to a fixed observer on the earth's surface. The zenith is defined as an imaginary point directly above the observer's location [41], or 90˚ to the astronomical horizon. The solar zenith is defined as the angle subtended by the zenith and the sun [39]. The zenith exists as a fundamental reference for defining the altitude of the sun as illustrated in Figure 2-7. For any location, by computing the vector product of the normal to the earth's surface and the vector from the sun to that location, the cosine of the solar zenith angle can be obtained; the complement of the solar zenith is the solar elevation, also known as the altitude. For example, if consideration is given to a

reference coordinate on the equatorial plane in the celestial sphere as presented in Figure 2-4, with points *x* defined along the east-west axis, point *y* defined for the point of intersection with the local meridian plane and point *z* defined for the celestial polar axis, then for a given latitudinal position in degrees the normal to the surface would be [39]

$$\hat{normal} = y * \cos(latitude) + z * \sin(latitude) \tag{7}$$

The corresponding unit vector from the sun to the observer is dependent on the tilted equatorial plane with an offset of the solar declination (dec) and the sun's hour (ha), as shown in Figure 2-3 and 2-4 respectively, and can be illustrated as [39]

$$\hat{sun} = x * \cos(dec)\sin(ha) + y * \cos(dec)\cos(ha) + z * \sin(dec). \tag{8}$$

Computing the dot product of the normal to the surface with respect to an observer and the direction of the sun yields the cosine of the angle between the two. The angle between the normal to the surface and the sun's direction is the solar zenith denoted by [39]

$$\hat{zenith} = \sin(latitude) \cdot \sin(dec) + \cos(latitude) \cdot \cos(dec) \cdot \cos(ha). \tag{9}$$

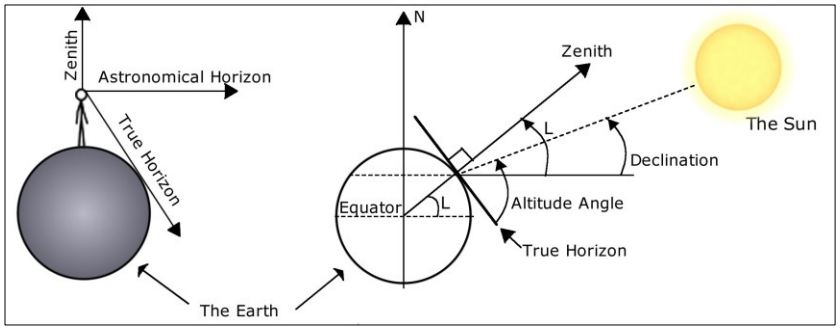

Figure 2-7: Illustration of the zenith, true horizon and the various angles referencing the sun from a fixed position on the earth's surface. "L" in the Figure represents the latitudinal angle. The altitude angle shown is also known as the solar elevation and it forms a complementary angle with the solar zenith.

The solar elevation and zenith angles define the vertical position of the sun with reference to the local or true horizon, while an azimuthal angle defines the horizontal component of the sun's position due north or south from an observing position. This angle is given by [39]

$$\hat{azimuth} = \sin^{-1}\left[-\frac{\cos(dec)\cdot\sin(ha)}{\cos(\frac{\pi}{2}-\hat{zenith})}\right]. \tag{10}$$

The expected azimuthal angle is between 0˚ and 360˚. In some cases, the equation (10) above might produce more than one solution where $[\sin(dec) - \sin(\frac{\pi}{2} - \hat{zenith}) \cdot \sin(latitude)] > 0$. For such scenarios, a conditional

selection is made such that $\widehat{azimuth} = azimuth + 360°$ when $\sin(\widehat{azimuth}) < 0$ and $\widehat{azimuth} = 180° - \widehat{azimuth}$ when $sin(\widehat{azimuth}) \geq 0$. A detailed algorithm for the calculation of the sun's position which includes azimuth and elevation angles to high accuracy is presented later in section 2.2.4.

Figure 2-8 illustrates the movement of the sun above the horizon and the corresponding change in azimuth and elevation angled as observed from the earth's surface. The sun's coordinate may be established by solar elevation (0˚ - 90˚) and the azimuth angle (0˚ - 360˚), which depend on the position of the observer. Since the sun's right ascension changes constantly over the year due to the revolution of the earth, calculation of the solar declination and right ascension can be made without location specific information. Once a universal time is specified, the solar hour angle can be calculated for any given latitude and longitude combination and can be combined with the solar declination to determine the zenith, elevation and azimuth angles. The hour angle and solar declination can be used to point equatorial-mounted equipment in the right direction, while the elevation and azimuth angles can be used to point alt-azimuth-mounted equipment (such as CPV, PV panels and solar measuring instruments).

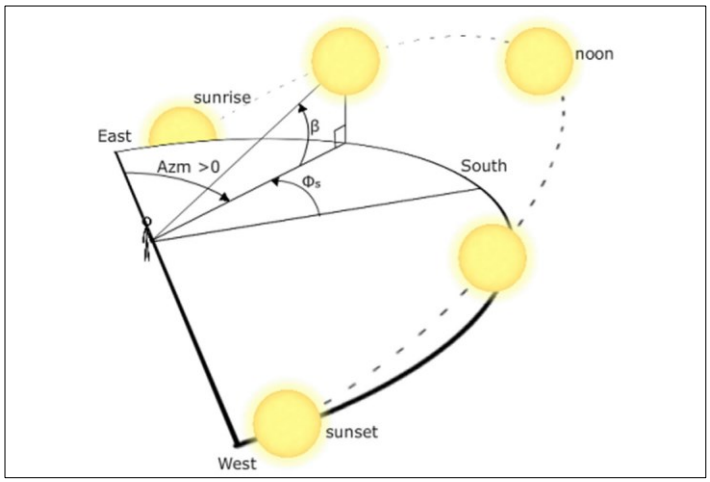

Figure 2-8: The path of the sun above the horizon as observed from the ground in a day. The azimuth angle is usually measured from the north; in such a case, if the sun is directly over the east, it would have an azimuth angle of 90˚. The azimuth can also be referenced to the south as depicted by ϕ_s in the Figure and by convention is considered positive before noon. The elevation β is also shown.

2.2.4 Time Systems

Calculating the azimuth and elevation of the sun from the solar time can be performed with relative ease as the solar time has a relationship between the observer and the sun position.

However, for ground based observation at different locations on the earth's surface, calculations based on the local time would be much more appropriate and useful. The "Local Standard Time" (LST) denotes the time in a specific time zone, without daylight savings time correction, and is equal to the mean solar time at the central meridian of each zone. Mean solar time corresponds to the hour angle of the "mean sun" and is given by the "Universal Time 1" (UT1) time scale (equivalent to the old "Greenwich Mean Time – GMT", but adjusted for polar wobble). "Coordinated Universal Time" (UTC) is measured by an atomic clock and is synchronized to solar time by the addition of leap seconds. UTC, being the more precise successor to GMT, is also referenced to the zero degree longitudinal line. The UTC along with the local time zone fixes the local standard time. Conversely, knowing the local time (and daylight savings offset) and the time zone permits all temporal measurements to be referenced to UTC.

2.3 Calculating Solar Coordinates

Highly accurate calculations of the sun's position are necessary for determining minute changes in air mass which is an important factor for accurate simulation of the radiative atmospheric transfer of sunshine. Tracking algorithms for dual axis trackers also require high accuracy calculations of the position of the sun to function optimally. Some equations previously presented in this chapter for the calculation of solar coordinates yield basic accuracy within ±2% of the true values. This section presents a detailed algorithm to calculate the zenith, hour, elevation and azimuth angles of the sun for any given longitude, latitude and local time. The basic inputs required are the location time zone, local standard time, longitude and latitude. The algorithm includes corrections for the earth's obliquity. Figure 2-9 presents a flow diagram illustrating the process for calculating high accuracy solar coordinates, as presented by the National Oceanic and atmospheric Administration (NOAA) [42]. The time used is the Julian date (the number of days since January 1st, 4713 BC – known as the Julian day – plus the day fraction, as a decimal), as per astronomical convention, with the Julian day beginning at noon GMT. Denoting the Julian century as jc, and the Julian day as jd, the Julian century is given by

$$jc = (jd - 2451545)/36525 \,. \tag{11}$$

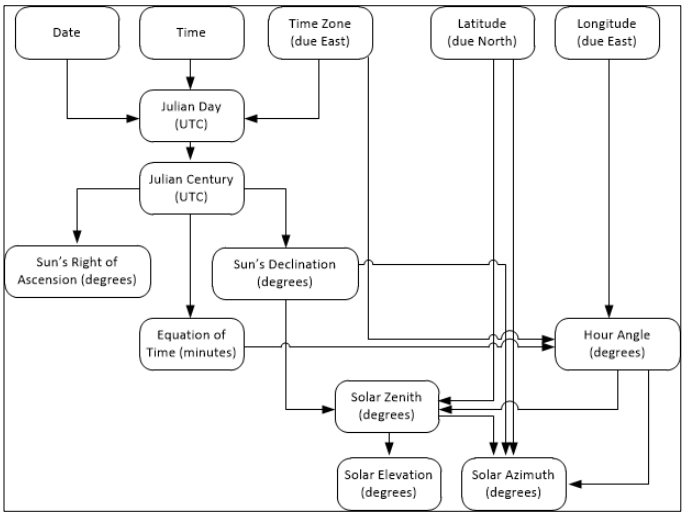

Figure 2-9: A flow diagram for deducing high accuracy elevation and azimuth angular values for the position of the sun from any given longitude and latitude at any given time.

The parameters necessary to calculate solar position include the geometric mean longitude of the sun, gl; the geometric mean anomaly of the sun, ga; the eccentricity of the earth's orbit, eeo; the sun's equation of centre, stc; the sun's true longitude, stl; the sun's true anomaly, sta; the sun's apparent longitude, sal; the earth's mean obliquity, mo; and a correction factor for the earth's obliquity, co. Equations (12) to (20) provide the formulas for calculating the parameters [42]:

$$gl = (280.46646 + jc36000.76983 + jc^2 0.0003032)\ \%\ 360 \tag{12}$$

$$ga = 357.52911 + jc35999.05029 - jc^2 0.0001537 \tag{13}$$

$$eeo = 0.016708634 - jc0.000042037 - jc^2 0.0000001267 \tag{14}$$

$$stc = \sin\left(\frac{\pi}{180} ga\right)(1.914602 - jc0.004817 - jc^2 0.000014) + \sin\left(\frac{\pi}{90} ga\right)(0.019993 - j20.000101) + \sin\left(\frac{\pi}{60} ga\right) 0.000289 \tag{15}$$

$$stl = gl + stc \tag{16}$$

$$sta = ga + stc \tag{17}$$

$$sal = sta - 0.00569 - 0.00478 \sin\left[\frac{\pi}{180}(125.04 - jc1934.136)\right] \tag{18}$$

$$mo = 23 + \left[26 + \left(\frac{21.448 - jc46.815 + jc^2 0.00059 - jc^3 0.001813}{60}\right)\right]/60 \tag{19}$$

$$co = mo + 0.00256 \cos\left[\frac{\pi}{180}(125.04 - j2 * 1934.136)\right]. \tag{20}$$

These parameters permit the sun's right ascension (ra in degrees) and declination angle (dec in degrees) to be calculated as [42]

$$ra = \frac{180}{\pi}\left\{\text{atan2}\left[\cos\left(\frac{\pi}{180}sal\right), \cos\left(\frac{\pi}{180}co\right) * \sin\left(\frac{\pi}{180}sal\right)\right]\right\} \quad (21)$$

$$dec = \frac{180}{\pi}\left\{\sin^{-1}\left[\sin\left(\frac{\pi}{180}co\right) * \sin\left(\frac{\pi}{180}sal\right)\right]\right\}. \quad (22)$$

The equation of time (et, in minutes), the solar time (st, in minutes) and the hour angle (ha, in degrees) can then be computed from the following [42]:

$$var = \left\{\tan\left(\frac{\pi}{180}\frac{co}{2}\right)\right\}^2 \quad (23)$$

$$et = 4\frac{180}{\pi}\left[var \sin\left(\frac{\pi}{90}gl\right) - 2\, eeo\, \sin\left(\frac{\pi}{180}ga\right) + 4\, eeo\, var\, \sin\left(\frac{\pi}{180}ga\right)\cos\left(\frac{\pi}{90}gl\right) - 0.5\, var^2\, \sin\left(\frac{\pi}{45}gl\right) - 1.25 eeo^2\, \sin\left(\frac{\pi}{90}ga\right)\right] \quad (24)$$

$$st = (time\ 1440 + et + 4\, long - 60\, timezone)\ \%\ 1440 \quad (25)$$

$$ha = \frac{180}{\pi}\left\{cos^{-1}\left[\frac{\cos\left(\frac{\pi}{180}90.83\right)}{\cos\left(\frac{\pi}{180}lat\right)}\cos\left(\frac{\pi}{180}dec\right) - \tan\left(\frac{\pi}{180}lat\right)\tan\left(\frac{\pi}{180}dec\right)\right]\right\} \quad (26)$$

where $time$ is the fraction of the day since midnight, $long$ is the observer's longitude in degrees due east, $timezone$ is the observer's time zone and lat is the observer's latitude due north. The solar zenith and elevation angles can now be calculated as [42]

$$zenith = \frac{180}{\pi}\left\{\cos^{-1}\left[\sin\left(\frac{\pi}{180}lat\right)\sin\left(\frac{\pi}{180}dec\right) + \cos\left(\frac{\pi}{180}lat\right)\cos\left(\frac{\pi}{180}dec\right)\cos\left(\frac{\pi}{180}ha\right)\right]\right\} \quad (27)$$

$$elevation = 90 - zenith \quad (28)$$

Finally, the azimuth angle can be calculated using equation (10).

2.4 Atmospheric Transmission of Sunlight

The earth's atmosphere is a layered sequence of gasses retained by the earth's gravitational force. The atmosphere is primarily composed of about 78% nitrogen (N) and 21% oxygen (O_2). Other gasses such as argon (AR), carbon dioxide (CO_2), water vapour (H_2O), methane (CH_4), ozone (O_3) and particulate matter represent about 1% of the atmosphere's composition. The commonly referenced boundary between the earth's atmosphere and outer space is given by the Karman line. The atmosphere acts as a filter with variable transmission

characteristics through which the solar radiation incident on the earth must pass through to reach the earth's surface. The extraterrestrial spectrum, shown in Figure 2-1, becomes spectrally modified and attenuated by its passage through the atmosphere due to absorption and scattering processes. The solar absorption has a linear characteristic where the absorbed irradiance is proportional to the apparent distance through which the sun rays travel to the earth's surface.

2.4.1 Air Mass

The air mass coefficient is a dimensionless quantity that is often used to define the length of the direct optical path through the earth's atmosphere, relative to the path length at solar zenith. The air mass for the sun at the top of the atmosphere is denoted as AM0, while ground based air mass is computed from the solar zenith or elevation as either

$$airmass = \frac{1}{\cos(\text{zenith})} \tag{29}$$

$$\text{or} \quad airmass = \frac{1}{\sin(\text{elevation})} \tag{30}$$

The air mass coefficient is a measure of the apparent length through the atmosphere which the sun's rays pass to get to the earth's surface. An air mass of 1.5 (AM1.5) is the nominal average air mass for most typical PV locations. A combination of optical scattering due to atmospheric diffractive, refractive and reflective phenomena in the atmosphere and absorption by atmospheric constituents through the apparent length of the air mass significantly modifies the AM0 spectral distribution of solar irradiance, as shown in Figure 2-10. The black line represents the AM0 spectrum while the green line represents the AM1.5D direct irradiance spectrum incident on the earth's surface after attenuation by the atmosphere. The shaded portion represents losses due to irradiance attenuation and absorption in the atmosphere.

Figure 2-11 illustrates the net radiative transfer, absorption and scattering components responsible for spectral modification of the extraterrestrial solar irradiance by passage through the atmosphere. Bulk spectral absorption and attenuation of the ultraviolet light in the short wavelength region of the solar spectrum (below 280 nm) is attributed to ozone molecules. Perceptible water vapour absorbs and attenuated irradiance in the long wavelength infrared region. Band absorption also occurs at various wavelengths due to

gasses such as oxygen, carbon dioxide, methane, ozone and perceptible water vapour. Rayleigh scattering and atmospheric aerosols which are constituted of dust, smoke and suspended particulate matter of various sizes, affect a broad range of wavelength in the solar spectrum. The perceived blue color of the sky which is often observed in mid-day is as a result of the un-balanced spectral absorption of the sunlight. The wavelengths which correspond to red and green colors are absorbed relatively higher than the blue color wavelengths.

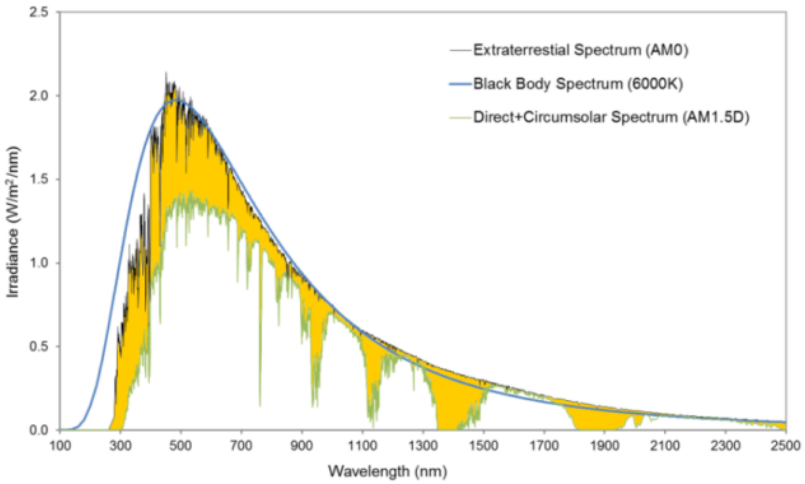

Figure 2-10: Comparison of a 6000K black body spectrum with spectra at various layers of the atmosphere.

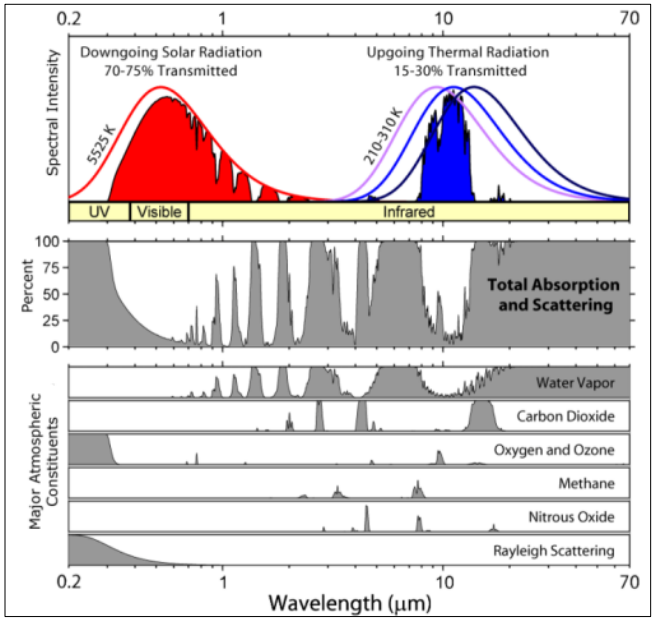

Figure 2-11: Transmission of radiation through the atmosphere. The diagram illustrates bands of the spectrum absorbed by the atmospheric gasses and irradiance scattering phenomena such as Rayleigh scattering [43].

Air mass decreases from sunrise to noon and increases from noon to sunset and the apparent depth of atmosphere that the rays of the sun needs to pass through varies proportionally, as does the absorption of sunlight. Figure 2-12 illustrates the spectral effect of the variation in absorption, refection, diffraction and refraction by atmospheric constituents on the incident Direct Normal Irradiance (DNI) component of the sunshine. It should be noted that the peak power wavelength shifts with airmass and this phenomenon poses a challenge for current matching in epitaxially grown multi-junction solar cells.

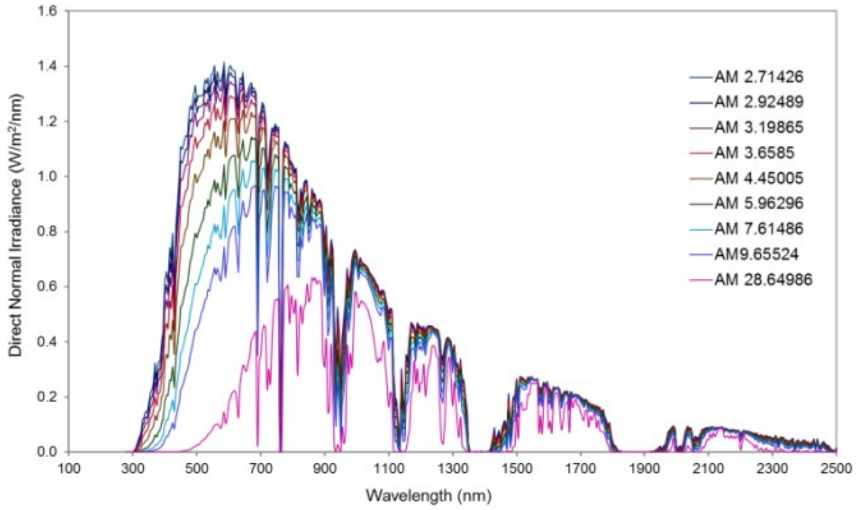

Figure 2-12: SMARTS2 simulated direct normal spectra irradiance illustrating spectral variation due to air mass change.

2.4.2 DNI, GHI and Diffuse Irradiance

The presence of particulate matter in the atmosphere results in the reflection and scattering of sunlight. Sunlight detected by an observer from the entire sky dome is known as the global irradiance, and it may be subdivided into several classes on the basis of its various angular distributions. These components are the direct normal irradiance (DNI), the global horizontal irradiance (GHI), and the diffuse irradiance (DHI). Each irradiance component has unique optical characteristics that depend on atmospheric conditions, as described below.

2.4.2.1 Diffuse Irradiance

The diffuse irradiance (DHI) arises from a combination of sources. It consists of light scattered from its direct path through the atmosphere by particulate matter (gases or clouds) toward the observer. This scattered light can originate directly from the sun, from light

reflected from surrounding infrastructure or trees, and from light reflected from the ground (i.e., the earth's albedo). Consequently, the diffuse irradiance is effectively isotropic and primarily a function of the zenith angle or air mass under non-cloudy conditions. For most scenarios, diffuse irradiance is determined for a reference horizontal plane.

2.4.2.2 Direct Normal Irradiance

The fraction of irradiance passing through the atmosphere without obstruction and normal to the observation surface plane is the direct normal irradiance (DNI), as shown in Figure 2-13. Under non-cloudy clear sky conditions, the majority of the light incident on the earth's surface is direct. In the context of this dissertation, we note that direct sunlight is the only irradiance that can be collected by solar concentrators.

2.4.2.3 Global Horizontal Irradiance

Global horizontal irradiance (GHI) is the full 2π-steradian irradiance above a horizontal observation plane. It consists of the direct and scattered rays of the sun, that is, the direct normal irradiance and the downward-directed diffuse horizontal irradiance (DHI). Figure 2-13 illustrates several sunlight paths that contribute to global horizontal irradiance. Gases and dust particles absorb and reflect the sunlight in the atmosphere. The clouds reflect and diffract the sunlight changing the incident angle while some sunlight passes through clear sky to contribute to direct normal irradiance. Reflections from the clouds that are directed towards the ground as well as reflections from ground infrastructure contribute to diffuse irradiance. When the light reflected from the ground is added to the GHI, the resulting irradiance is known as the total global irradiance. The relationship between the various irradiation components is given by

$$GHI = DNI * \cos(zenith) + DHI \tag{31}$$

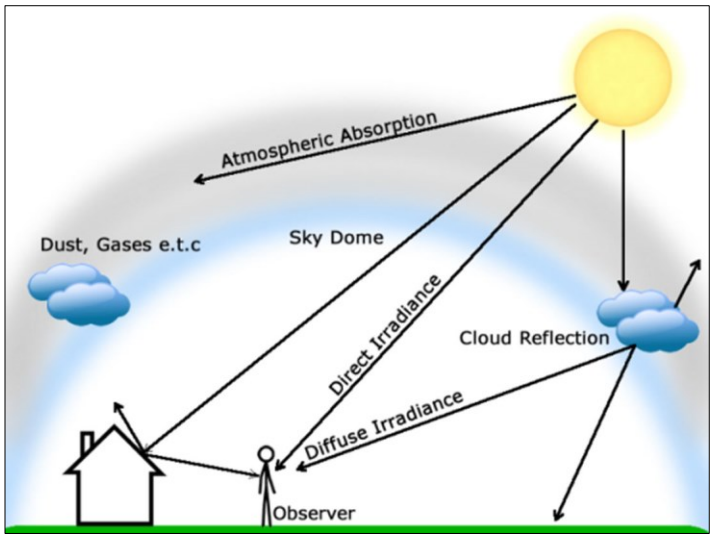

Figure 2-13: Components of sunlight passing through the atmosphere.

2.5 Measuring the Solar Resource

Performing PV systems analysis requires knowledge of the local absolute solar resource. In the case of spectral irradiance, one may wish to measure direct, diffuse or global horizontal spectral irradiance, depending on the nature of the PV system under consideration. In particular, setups are required for evaluating the solar resource observed from a tilted plane. The three main methods for measuring irradiance are (1) ground based measurements, (2) airborne measurements, and (3) satellite based measurements. Not much need be said about airborne and satellite measurements as they are sparingly used or rarely implemented and they do not provide results of high spatial granularity. For spatial measurements, ground based methods are ideal.

Spectral irradiance is typically measured with a spectroradiometer. In some cases where absolute irradiance is not required, a spectrometer may be used. Both spectroradiometer and spectrometer measure the incident sunlight at specific wavelengths using complex optics and mechanics to separate, detect and identify absolute or relative irradiance of various light wavelengths, but the former permits quantitative total irradiance measurements while the latter does not.

Measuring the direct irradiance from the sun requires an instrument that is always pointed at the sun. A pyrheliometer is such a device that uses a thermopile to measure the intensity of incident irradiance. It is often used with a dual axis tracker to keep the field of

view pointed towards the sun for a continuous time series measurements are required. Overall, the pyrheliometer is designed to limit the diffuse light incident on the thermopile to a degree that allows most direct solar irradiation through.

When measuring diffuse or global horizontal irradiance, a pyranometer is used. Similar to a pyrheliometer, it likewise uses a thermopile for detecting the intensity of the incident solar resource; however it differs from a pyrheliometer in that its optics design is made to maximize the horizontal field of view around the instrument. By applying a shading disk to block the direct component of sunlight on a pyranometer, the instrument can also be used for measuring diffuse irradiance.

2.6 Harvesting the Solar Resource

Methods for harvesting the solar resource are divided between thermal systems and PV systems, or some hybrid of both. In this dissertation, the focus is on concentrating PV. We now discuss the optical train and system components that enable this concentration. CPV systems make use of concentrating optics to focus direct normal solar irradiance on the solar cell. Sometimes only a primary optic is used to concentrate the light, but often a secondary optic is used to refine the process thus allowing better acceptance angle, reducing chromatic aberration or increasing flux uniformity on the cell. Numerous designs have been developed based on lens material, tracker architecture or light focus methods.

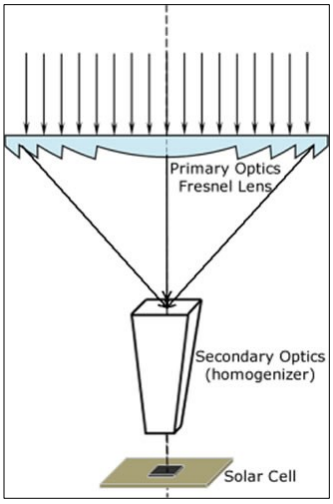

Figure 2-14: Illustration of primary and secondary optics arrangement with a solar cell in a CPV system (not to scale). In this type, a Fresnel lens is used as the primary optics and a secondary optics is present [15].

2.6.1 Trackers and Concentrators

A brief review of some of the technology for trackers and concentrators in CPV system deployment is presented. Ranging from diffractive, internal reflection and external reflective systems, the various CPV systems are presented below in Figures 2-15 to 2-21.

Figure 2-15: The SUNRISE demonstrator at NREL, Ottawa Canada. [15].

Modules of the SUNRISE demonstrator at NREL are made up of six individual optical systems. Each system consists of a Fresnel based concentrating primary optic, an acrylic homogenizer and high efficiency quantum dot based multi-junction solar cells similar to the design in Figure 2-14. The tracker is an OPEL solar dual axis tracker which is utilizes a pole mount design. As seen in Figure 2-15, an advantage of the tracker is the fact that it occupies little ground space. However, to handle wind loads its installation often requires a reinforced concrete base installed into a deep trench.

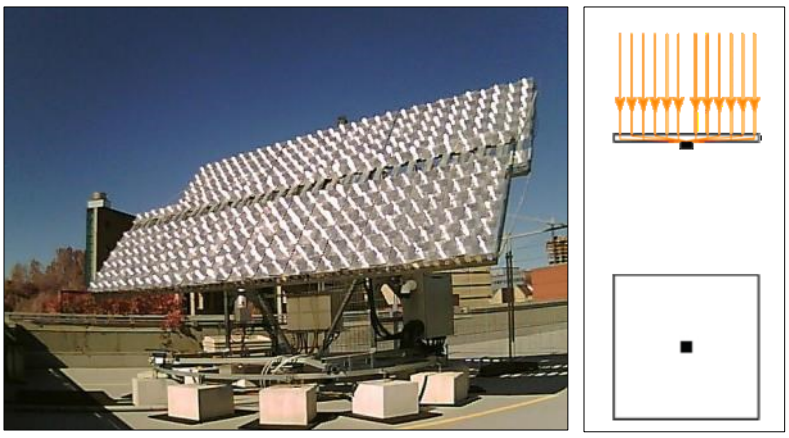

Figure 2-16: The APECS demonstrator at the University of Ottawa solar test site (Left). An illustration of the light guide optics used to concentrate sunlight on the multi-junction cell (Right).

APECS demonstrator modules at the University of Ottawa, shown in Figure 2-16, are made up of six individual optical systems electrically connected in series. Each primary optic, built with acrylic materials, is based on a light guide system that concentrates light on a cell by guiding light from a relatively large surface area to a small multi-junction high efficiency solar cell. The CPV system was developed by Morgan Solar and the tracker is a Golden sun dual axis tracker. A key feature of the tracker design is its weight distribution which allows its installation on a flat surface without the need for trenches. The APECS demonstrator was installed on a rooftop parking lot to take advantage of this feature.

Figure 2-17: An array of Emcore CPV systems with tilt and roll tracking and silicone on glass lens [46].

The renowned PV company Emcore, noted for its development of high efficiency solar cells for extraterrestrial applications, has also deployed terrestrial systems. They make use of tilt and roll trackers installed in arrays, as illustrated in Figure 2-17. Their concentration system, which uses silicone on glass lenses, operates at a higher concentration of about 1090x than other CPV systems that operate at about 500x.

Figure 2-18: A parabolic light concentrating dish using mirrors at the Hermannsburg power station in Australia [15, 45].

A parabolic dish made up of square shaped individual mirrors, shown in Figure 2-18, has been used to develop a concentrating PV system. The system was used to deploy a 1 MW plant at the Hermannsburg power station in Australia. Each dish is 130 square meters in size and it concentrates sunlight to an array of Spectrolab high efficiency multi-junction solar cells. The total concentration of the system is about 500x and the high efficiency multi-junction solar cells are actively cooled with water.

Figure 2-19: Concentrix solar array.[46].

In 2009, Soitec, another well known PV company, acquired Concentrix – the originators of the system shown in Figure 2-19. Subsequently, ten years of research in conjunction with the Fraunhofer institute in Freiburg Germany has brought about technological success. The system uses small Fresnel lenses (4cm by 4cm) to focus sunlight on relative small circular high efficiency solar cells with a metamorphic triple junction design (~2mm diameter). Secondary optics had been initially omitted, however recent developments has witnessed the addition of a reflective secondary optics which is said to increase acceptance angle, color mixing and flux uniformity of their module [15, 47, 48]. The tracker is a dual axis system based on a pole design which requires a deep trench for installation.

Figure 2-20: Dome shaped Fresnel lenses concentrating systems. [44].

For minimizing chromatic aberration and maintenance of short focal lengths, acrylic materials have been used to create domed Fresnel primary optics for CPV. This system, shown in Figure 2-20, was developed by Diado Steel, and a test plant has been deployed in Tokoname City, Aichi Prefecture, Japan [44].

Figure 2-21: CPV demonstrator developed by Solfocus, deployed in Kailua Kona at the National Energy Laboratory of Hawaii [15, 47, 49].

Solfocus developed a CPV system which uses a non-imaging, two stage reflective optic that concentrates sunlight up to 650x. The system, shown in Figure 2-21, has been deployed at the National Energy Laboratory, Kailua Kona, Hawaii [15, 47, 49].

3 Models, Simulations, Hardware and Research Tools

The content of this chapter is presented in three major sections. Section one aims at describing in brief detail the existing research architecture in the SUNLAB, as well as some specific equipment used for characterization of PV systems. Corresponding software tools designed and implemented by the author to use such hardware are also discussed. Section two presents the measurement and databasing of meteorological data sets necessary for CPV performance evaluation. In section three, an algorithm for a high performance modeller to simulate solar systems (cell and optics assembly) is presented. It utilizes the single diode model described in [15, 31, 32]. A java application modeller was developed from the algorithm and the modeller lays the background for the energy yield analysis performed in chapter 4.

3.1 Introduction - SUNLAB

The solar cells nanostructured device laboratory (SUNLAB) is a University of Ottawa research group founded in 2007 for the development, testing and characterization of solar cells and basic PV systems and subsystems. Currently, the group operates two high end solar simulators capable of simulating one sun irradiance and high concentration irradiance (500x – 1000x). Temperature controlled current – voltage (IV) measurements of samples are also possible due to the availability of adequate source meters. Critical PV semiconductor measurements such as external and internal quantum efficiency, electroluminescence and photoluminescence are also performed.

Advanced computer models are being developed for complex multi-junction solar cells, as well as novel single junction solar cells, using a large variety of semiconductor materials. With the aim of increasing cell efficiency to reduce PV system cost, software tools such as Synopsys Sentaurus (a world-leading commercial semiconductor device simulator) are being used to model these cells. Research is also carried out at the module level, for example, to enhance the acceptance angle and reduce chromatic aberrations of the sensitive concentrating optics which focuse the solar irradiance on the cell. Software packages such as Zemax (a ray tracing optics design application) enables researchers to analyse the flow of light through PV

system components. Thermal studies of CPV cell on carrier designs are carried out to increase heat sinking, which increases cell reliability and efficiency.

Evaluation of system performance and reliability is accomplished at an outdoor demonstration site monitored and maintained by the SUNLAB research group (presented in chapter 2). This site allows for continuous IV measurements of sample CPV and PV modules setup with different configurations to analyse system configuration effects, field module reliability and energy yield. Additionally, atmospheric and weather condition data are simultaneously collected into a database to inform predictive models of the solar resource as it varies under such conditions. These models are used to assess the economics in deploying PV technology.

3.1.1 Hardware Systems - Solar Simulators & Cell Characterization Equipment

Hardware available at SUNLAB include two solar simulators that produce artificial light of variable intensity for electrical and optical performance measurements of solar cells under variable illumination. The use of an artificial sun allows for controlled indoor testing of devices. Non-encapsulated bare cells, or cells on carrier, can be tested in the laboratory under controlled conditions such as temperature and electrical bias before they are incorporated into modules and installed in the field. Artificial suns also allow for the comparison of various cell characteristics under well-known spectral distribution and intensity of the illumination used.

3.1.1.1 Oriel Solar Simulator

The Oriel solar simulator (model 92191) is a low concentration continuous illumination artificial light source developed by Newport Inc., capable of producing light with a range of concentration between 1 and 150 suns. It relies on a 1600W xenon lamp to produce the high intensity illumination and its maximum uniform beam area is approximately 5 cm by 5 cm at low concentration. Since the simulator's light source is a xenon lamp, the spectral distribution of the output illumination has a profile that corresponds to black body radiation by gasses in the xenon class (with strong Xe lines). Consequently, a series of optional filters are used to control the output spectrum to simulate irradiance at various AM values. Filters

for AM 0, 1, 1.5 global, 1.5 direct and AM 2 are currently being used in the SUNLAB laboratory.

A PV cell characterization station has been setup to be used with the Oriel simulator. The system includes a test stage fitted with a temperature controller and a vacuum pump to allow characterization of bare semiconductor solar cells and cells on carriers. Highly conductive probes are often used to access and establish electrical connections on test samples. Other hardware used for the characterisation process include a high precision source meter used to bias a sample and record its response.

An intuitive software application has been developed to use the Oriel station. Its features include remote temperature settings, configuring the source meter bias, sweep and measurement of test samples and control of the Oriel shutter (necessary to obstruct the output light coming from the station). The application also provides options for calculating parameters and plotting results from measured data. A picture of the Oriel station is presented in Figure 3-1.

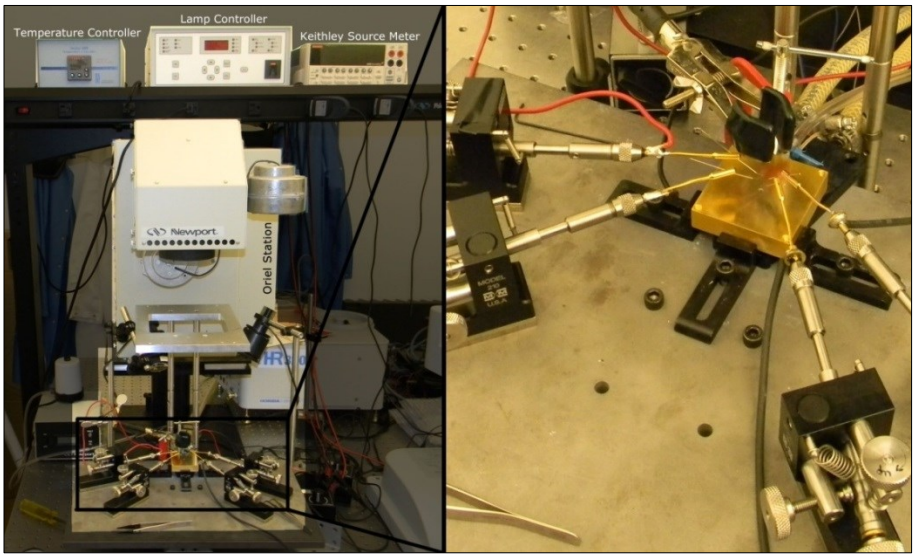

Figure 3-1: The Oriel Solar Simulator at SUNLAB, 2013.

3.1.1.2 XT-30 Solar Simulator

The XT-30 solar simulator is a high concentration system designed with state-of–the-art technology. It is the first of its kind and is designed, developed and supported by Spectrolab Industries. The business end of the simulator produces high concentration illumination using a 3000 W Xenon lamp capable of delivering over 1000 suns continuous illumination across a

uniform 1cm by 1cm area; higher concentrations can also be achieved by using a homogenizer with smaller aperture. The system includes a filter to achieve an AM1.5D terrestrial spectral distribution. Modification of the output spectrum profile can further be achieved with the addition of band filters. Due to the excessive heat produced by the Xenon lamp, integrated water cooling is required. An active pump system circulates chilled water through pipes and around the housing covering the lamp. Similarly, stages upon which the cells were mounted were also water cooled, allowing higher intensity illumination of cells without overheating.

Other interesting features of the XT-30 solar simulator include a shutter for temporarily obstructing the illumination, and the availability of four separate stages accessed by moving the simulator's beam output with an automated motor control system. This motor movement capability allows for precise on-sample alignment of the XT-30. A heat dump is used to dissipates light energy into the circulating chilled water supply when the simulator is idle.

The characterization system that accompanies the XT-30 includes electrical connections on each stage, a source meter, a National Instrument Data Acquisition (DAQ) system and precise motor control systems for moving the illumination head (Vemex controller). Intuitive software provides remote control, configuration and measurement. Detail of the software developed for performing various tasks is presented later.

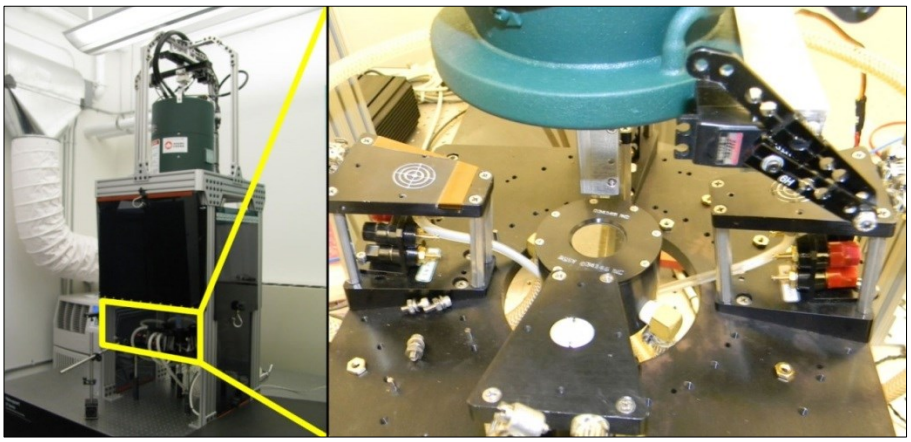

Figure 3-2: The XT-30 solar simulator and its accompanying hardware in SUNLAB's laboratory, April 2013. The green bin houses a high powered fan, the Xenon lamp and necessary filters for tuning the output light spectral distribution.

3.1.1.3 Sinton Flash Tester

The Sinton flash tester is a flash tester capable of delivering a white light spectrum in a very short time at high concentration. It is used for applications where measurements of the carrier lifetimes are required. The speed of a flash test effectively removes temperature effects since sample heating is minimal. The setup includes a vertically moveable head which houses a homogenizer in the form of a glass cylinder connected to a diffuser. A high luminance halogen lamp is managed by control electronics to produce the needed power for the flash. A computer system provides remote control of the lamp and is used to take measurements.

3.1.1.4 Newport's Quantum Efficiency Measurement Station

Quantum efficiency (QE) is a spectrally-dependent carrier collection probability generated by single-wavelength illumination across the device thickness, relative to the number of incident photons. It is indicative of the current production process when integrated over all wavelengths and gives insight into the recombination processes that reduce cell efficiency. The measurement process involves counting the number of photons at different wavelengths incident on the sample active area and the number of electrons that are collected at the terminal of the sample. External QE (EQE) is the ratio of the number of electrons collected to the number of photons externally incident on the cell; internal QE (IQE) is that ratio relative to the number of absorbed photons.

A Newport quantum efficiency test station is used for measuring the cell QE. The station is capable of measuring the QE of sub-cells in a multi-junction PV device up to four junctions. It consists of a number of light sources, a bias source meter, temperature control, wide band detectors (silicon and germanium) and accompanying software. A Xenon lamp is used in conjunction with a monochromator and filters to select individual optical wavelengths used for the tests. Other light sources provide bias light for isolating individual layers in the case of multi-junction solar cells. Temperature control keeps samples at 25 ºC using a thermoelectric device for heating and cooling (since the processes involved in QE are temperature dependent). The sample is fixed to a stage using suction from a vacuum pump, and highly conductive gold plated probes are sometimes used to establish electrical connection. A sample quantum efficiency measurement of a multi-junction high efficiency solar cell with quantum dot technology is presented in Figure 1-6. The Figure distinguishes

absorption efficiency of the 3 sub-cells within the solar cell. The corresponding portion of the photon energy of an AM1.5D spectrum is also shown.

3.1.2 Software Systems

To enable characterisation of solar cells and systems, user friendly software applications are required to control corresponding hardware. Most hardware venders provide basic software applications but additional features are frequently required to perform specialized tasks. In most cases where software needs to be modified for customized features, the process of modification requires well thought plans for ensuring compatibility and ease of use. Described below are new and modified software developed for a series of applications in characterising and evaluating PV cells and systems.

3.1.2.1 Simple, Pluggable Current-Voltage (IV) Utility

Measuring dark and light IV curves of solar cells is a key requirement for cell characterisation. In most cases, large, complex setups that come with specific vendor hardware are the toolset available to take reliable IV measurements. The choice of a power supply meter also determines the software to be used and the need to take multiple measurements of a single sample is often ignored. For mobile measurements, quick IV characterization and the use of multiple source meters in a user friendly manner, increases research efficiency. Plug and play applications are ideal in such circumstances.

3.1.2.1.1 Aim

A simple, pluggable current-voltage measurement toolset was driven by the need for a harmonized toolset for measuring IV curves on the XT-30 solar simulator. As with most hardware systems, vendor specific software was available with limited functionalities. The custom application aimed to increase efficiency in taking IV measurements. Designed for using interchangeable power supply meters (the Keithley 2400 series and Kepco power supply meter), the application was to provide a user friendly intuitive interface for taking and storing multiple IV measurements with and without the XT-30 setup. The application was design to be used with both a general purpose interface bus (GPIB) and a serial connection. The features include:

- plug and play application,

- simple interface for intuitive use,
- usability with both Keithley and Kepco source meters,
- ability to take and save multiple IV measurements,
- plotting of IV measurements in real time,
- ability to create, store and edit configuration profiles for the source meters and
- ability to plug-in application segments for controlling the XT-30 motor

3.1.2.1.2 Method / Description

Labview was chosen as the preferred development platform for building the "IV curve utility" due to its relative ease of use and deployment. The corresponding application design used a finite state machine structure to coordinate the application's operation. Figure 3-3 illustrates a flow chart of the applications initialization routine. Upon launch, the application performs a routine to search for connected hardware; loads configuration settings and initializes the hardware and interface. At this point, user input determines the next course of action to be taken by the application.

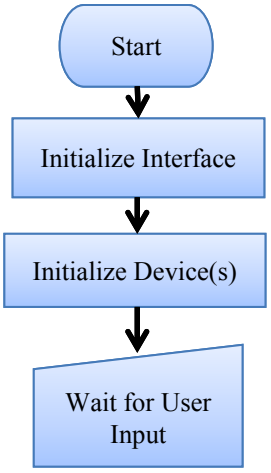

Figure 3-3: Flowchart illustrating an overview of the start-up procedure used in the application's finite state machine to ensure hardware and software interface is ready for use by the user.

Initializing the application interface consists of resetting the graphs, controls and indicators to their default value. However, initializing the devices – a Keithley or Kepco source meter interfaced through a GPIB interface, a Vemex motor controller interfaced through a serial interface and a National Instrument (NI) Data Acquisition system (DAQ)

interfaced through a universal serial bus (USB) interface – requires a fairly complex sub-procedure to search, reset, retrieve settings and then conFigure the device for 1 or 2-way communication. Figure 3-4 illustrates the search and conFigure routine performed during the device initialization process. It should be noted that in some cases where the automatic routine cannot proceed such as when a device physically dis-connected, the application required user input.

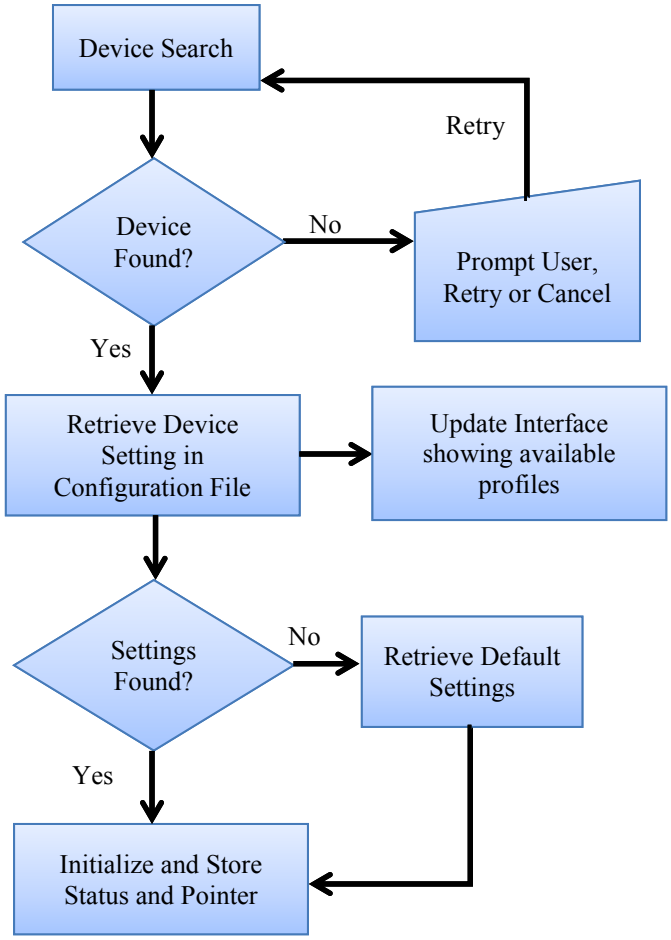

Figure 3-4: Flowchart illustrating the device initialization process for the source meters and the Vemex motor control.

The application uses a settings file for storing persistent configurations as illustrated in Figure 3-4. These configurations include the Vemex controller's stored reference positions that correspond to stages on the XT-30 and the source meter profiles. The system design provides for the creation of new profiles as well as editing existing profiles. This is implemented in the finite state machine when the user executes a profile save action. An

input to initialize a new profile creates a profile with default configurations that is expected to be modified and saved by the application user. Factors such as voltage limit, protection current, sweep range and sense mode are among the settings configurable by the user that can be persisted. A sanity check was implemented to ensure profile names are unique with default profile names automatically created from timestamp values. A delete feature was also incorporated to remove profiles from the settings file.

For each power supply meter configured, a unique initialization (INI) file section records a list of header keys. These correspond to section headings that store the settings for the specified device. Depending on the device unique features, the range of key-value pairs under each configuration key header varies significantly. Similarly, the Vemex controller stores labels, including *x* and *y* coordinates for each position. Twelve positions in total are available for configuration and persistence by the application user.

Within the finite state machine, a generic module was implemented to perform IV curve sweep operations. The module was designed generic to allow re-usability between the multiple source meters (Keithley and Kepco) and to be used as a plug-in within other applications. This module is referred to as the IV measurement module. When the sweep input is executed on the IV measurement utility, loaded configuration settings in conjunction with initialized pointers to the hardware device are passed to the IV measurement module which then returns results that include V_{oc}, I_{sc}, fill factor (FF) and maximum power (P_{Max}). Results returned from the IV measurement module are saved in an array with an initial id label of the timestamp. Provisions are made for this id to be edited to a custom text of choice by the application user. Simultaneously, the IV and power curve are plotted on two graphs. A list option is available for the user to scroll through recorded measurements.

A feature to save single and multiple recorded results into a spreadsheet file was implemented. The data for each measurement is recorded with identification of the measurement label previously mentioned. Each record is saved on two spreadsheet rows which allows ease of access to individual or multiple records. Basic error logging was implemented to allow for debugging the application.

3.1.2.1.3 Result

Using the IV utility involves connecting required hardware to a computer system and launching the application. Researchers began using the application by early 2013 at the

SUNLAB laboratory and ongoing reviews have aided its refinement to its current state. IV curves could be plotted in normal or log scale. The Figures 3-5 and 3-6 present the application interface.

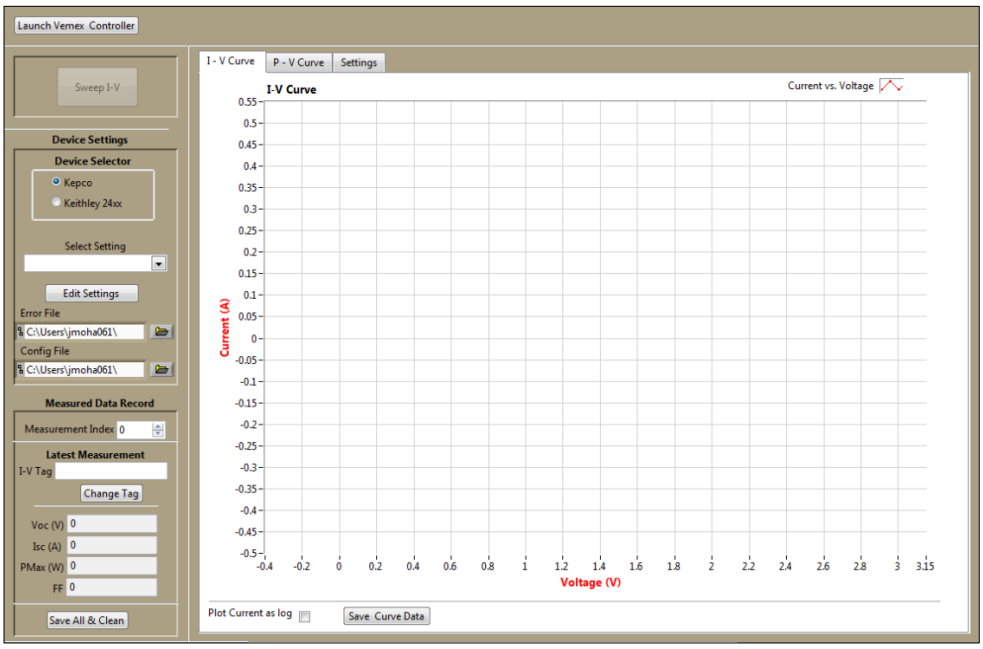

Figure 3-5: Main Interface of the developed application showing the IV-curve graph. The user friendly interface offers intuitive Input controls.

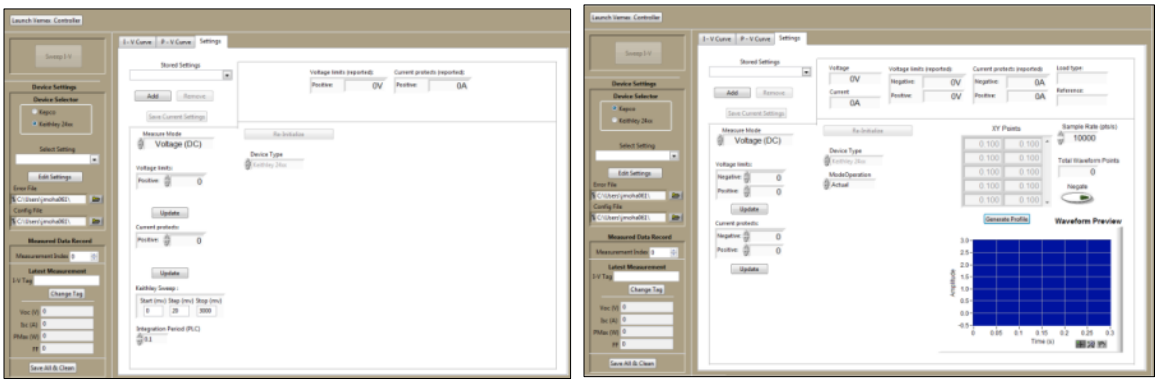

Figure 3-6: A contrast between configuration settings for a Keithley source meter (Left) and when a Kepco source meter (right). The interface is generated according to the user's input.

3.1.2.2 Spatial Uniformity Measurement Systems

Spatial uniformity in the context of this dissertation refers to the response from the intensity profile along *x* and *y* coordinates of the beam exiting the homogenizer on the XT-30 solar simulator or the response from a solar cell being the short circuit current or maximum power due to uniform illumination per unit surface area on the cell. Two applications have been

developed to measure and record the spatial uniformity of a beam exiting the solar simulator and the response on a solar cell.

3.1.2.2.1 Spectral Spatial Uniformity Utility

Understanding the spatial uniformity of the beam exiting the homogenizer is important to fully understand the response from a solar cell. Since the solar cell is sensitive to spectral variations, the spectral response of this uniformity test is also important. A beam evenly spread across the full active area of the cell with uniform intensity at each wavelength is the ideal. However, since the solar simulator makes use of filters to control its output spectrum, and since the various wavelengths of light are affected differently, some tuning is often required to acquire the best fit. An application exists which makes use of the integrated irradiance from a silicon detector to measure the overall intensity of the XT-30 beam through a pin hole. By moving the homogenizer across this pin hole in a systemic pattern, a 3D picture could be generated to depict the overall uniformity of the beam.

3.1.2.2.2 Aim

The proposed application uses a spectroradiometer as the detector so that the spatial uniformity as a function of frequency can be measured. The application should be able to generate 3D plots to depict the spatial uniformity of the beam exiting the XT-30 for all wavelengths observable by the spectroradiometer. The intensity of several wavelengths that correspond to the EQE of individual sub-cells should be grouped together to understand the beam uniformity per sub-cell.

3.1.2.2.3 Method / Description

The application exploited an existing algorithm from a spatial uniformity measurement system that uses a silicon detector. The process involved extending the features of the utility to record and store irradiance intensity for individual wavelengths. Additionally features were added to plot and save the results. Labview was the choice of development platform for the parent code, so the new application was also developed within labview for compatibility. A finite state machine structure was used to manage the operations flow. Similar to the IV utility described in section 3.1.2.1, the initialization procedure of the application involves searching for necessary hardware connections and saving a reference. More specifically, the

Vemex motor controller and an ASDi spectroradiometer must be detected for the application to proceed. Subsequently, user actions determine the state of the finite machine and hence the operation of the application.

Configuration settings used for capturing a measurement include the homogenizer size and an array size used as a resolution setting. A configuration file was used; data stored and retrieved from the file include parameters such as an IP address and the calibration files path for the ASDi spectroradiometer. Capturing a measurement begins by a performing a beam alignment procedure. Here, the application user manually places the XT-30 homogenizer beam directly centred over a pin hole receptor for the spectroradiometer and executes the beam alignment operation. Figure 3-7 below demonstrates the action performed in this operation.

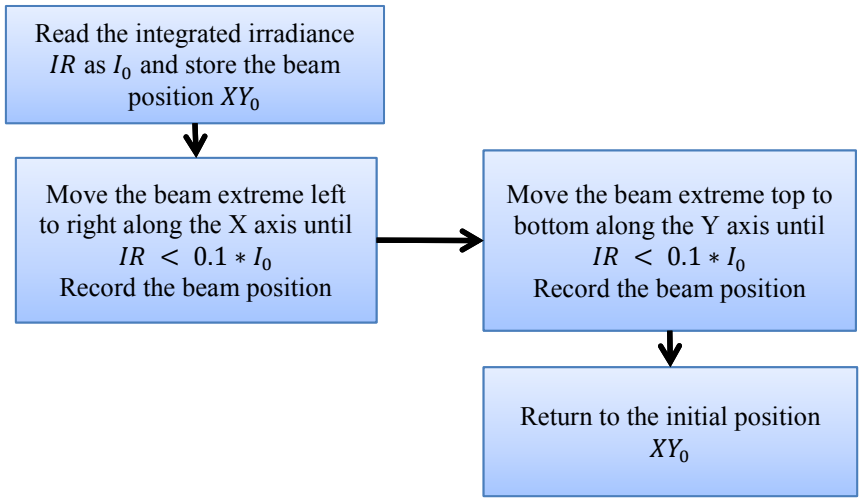

Figure 3-7: Illustration of the beam alignment procedure to ascertain the size of the beam in terms of X and Y coordinates and hence the limits of the scan.

Following the beam alignment, the application's logic estimates the range of movement, which depends on the selected homogenizer size (a 1cm by 1cm unit area or 0.5cm by 0.5cm unit area). It also estimates the resolution for the measurement (the number of data points needed) based on the square array settings. The process operates as depicted in Figure 3-8, where the application remotely moves the XT-30 homogenizer through the Vemex controller in calculated steps along the X and Y coordinates within the range determined from the beam alignment procedure while taking a spectrum measurement at each step. Precautions have

been taken to ensure that the spectroradiometer detectors are not saturated due to large fluctuations in the irradiance by performing an optimization procedure at each step.

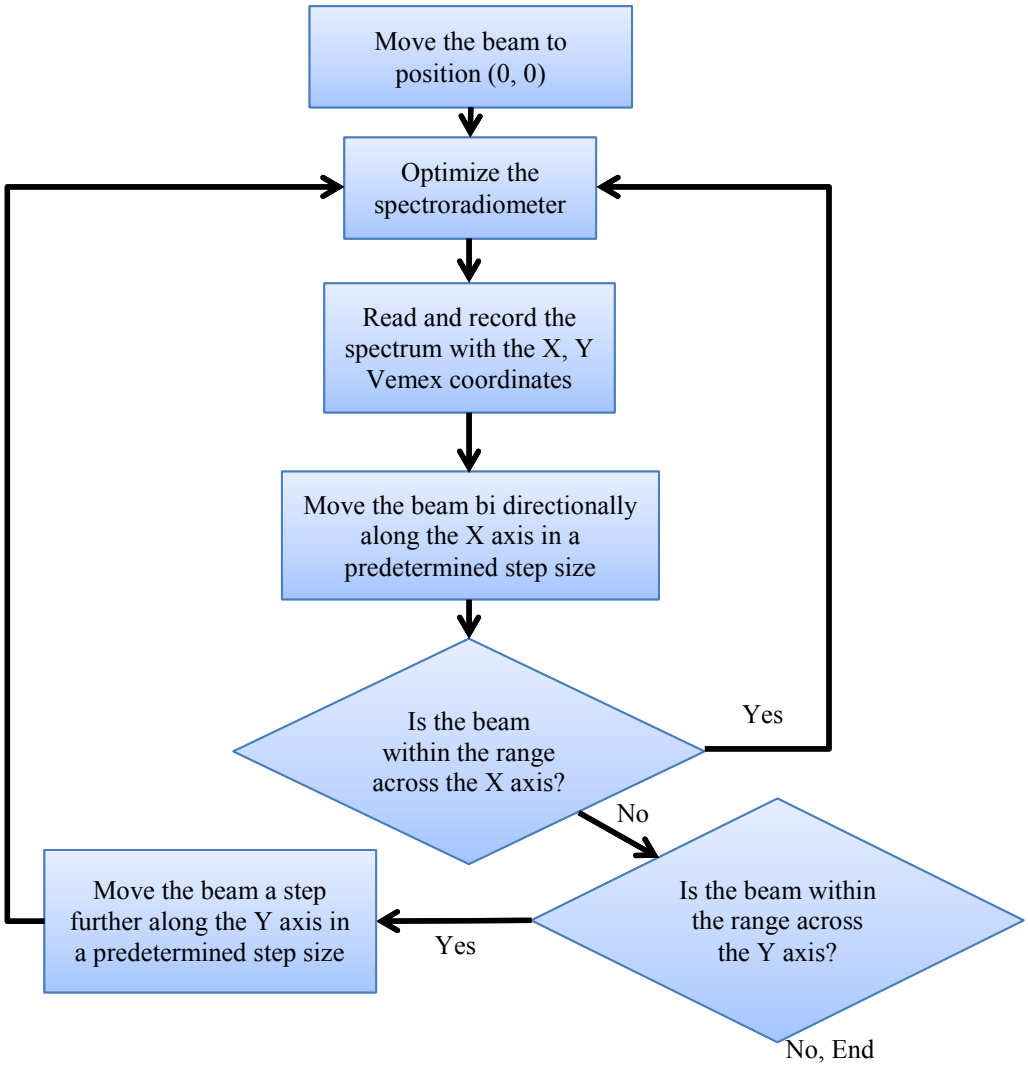

Figure 3-8: Flowchart illustrating the "raster-scan" procedure when capturing the uniformity of the XT-30 beam.

3.1.2.2.4 Results

The developed application's interface is presented in Figure 3-10. As earlier discussed, the application features 3D and 2D graphs for individual wavelength profiles as well as profiles for variable wavelength ranges.

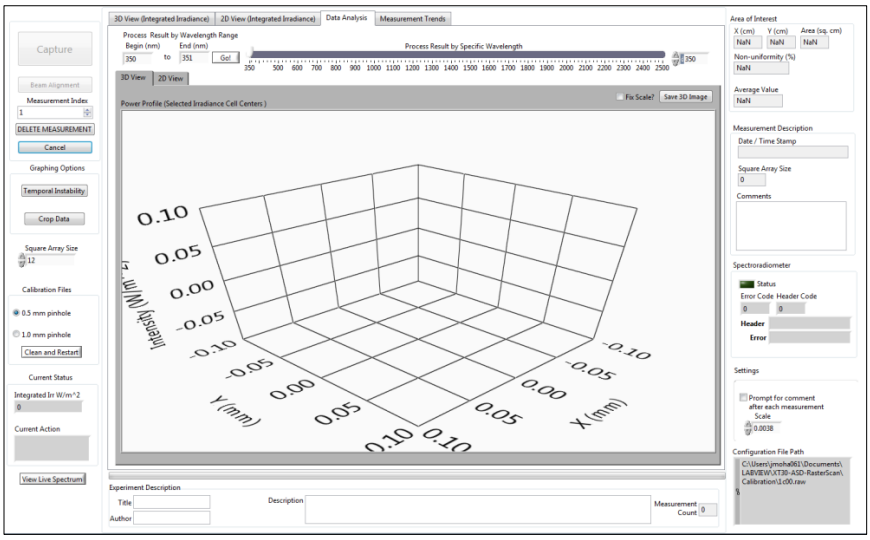

Figure 3-9: The application interface showing a sample run of spectral spatial uniformity measurement.

3.1.2.3 Solar Cell Spatial Uniformity Utility

Similar to beam uniformity measurement, the solar cell spatial uniformity measurement aims to determine the response per unit area from a solar cell. It is a source of complementary information that helps to determine the effect of dead or inactive bus-bar on solar cells.

3.1.2.3.1 Aim

The "solar cell spatial uniformity utility" was designed to perform a task similar to the "spectral spatial uniformity utility". However, instead of a pin hole and a spectroradiometer as a detector, it was designed to use a solar cell as the detector with a characterised beam from a specified homogenizer. .

3.1.2.3.2 Method / Description

The application was created using a template from the spectral spatial uniformity utility since several features were shared between the two applications, such as the pattern movement of the Vemex motor controller for the beam alignment and capture operation. What differed between the two applications was the mode of recording or sensing intensity. Again, a finite state machine was used. The initialization procedure for the application was similar to that of the IV Utility as depicted in Figure 3-6.

The IV measurement module introduced in section 3.3.1.2 was rebuilt to determine solar cell response through a power supply meter. The new module replaced all aspects of

spectroradiometer measurements in the spectral spatial uniformity utility used to determine intensities. Two methods of recording solar cell response were implemented: (1) use of the short circuit current from each light IV curve, and (2) the use of the maximum power on the cell's light IV curve. The data recorded during a capture operation was stored and plotted on a 2D and 3D graph. The data were also made exportable as a spreadsheet file for external use. For each critical operation, such as the beam alignment and the capture operation, the relevant changes were made using the spectral spatial uniformity utility to reflect the change of detector type.

It should be noted that issues may arise from cell carrier exposure to high concentration irradiance if the homogenizer used for the measurement is sufficiently larger than the active area of the cell. Increasing the step size for movement of the beam along the X and Y axis reduces this risk at the cost of measurement resolution. The ideal light source for this measurement would be one with a beam sufficiently smaller than the cell active area.

3.1.2.3.3 Results

Results from an initial test measurement carried out on a triple junction solar cell using a 0.5cm by 0.5cm homogenizer are presented in Figure 3-10. The Figure confirms that placing a beam at the centre of the cell yields the maximum current**.**

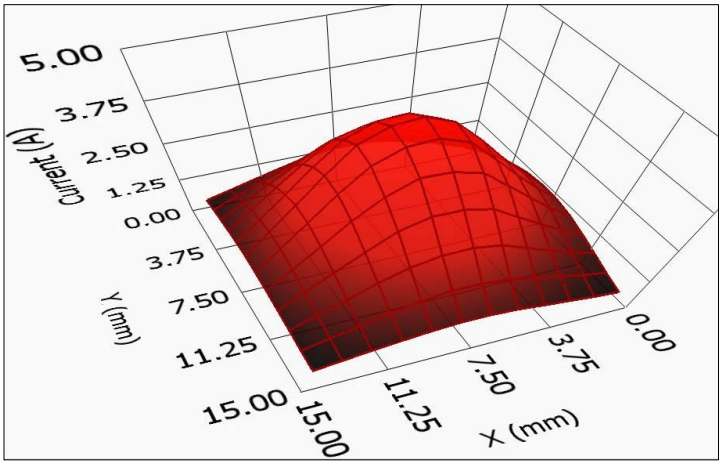

Figure 3-10: 3D profile of the uniformity across the surface of a triple junction solar cell.

3.1.2.4 Light-Cycling Utility

With the current growth rate of CPV implementation, besides enhancing cell efficiencies, researchers also aim to increase reliability of solar cells for longer periods on sun. Fluctuations of high concentration irradiance by movement of clouds and diurnal variations stress CPV system components, particularly the cell-on-carrier. Degradation is expected to be a delamination of the cell from its carrier due to crack propagation from voids in the soldered joint between the cell and its carrier. For researchers to experimentally evaluate this degradation effect, accelerated aging tests can be conducted in the lab by simulating temperature fluctuations on a cell through optical cycling.

3.1.2.4.1 Aim

The aim of the light-cycling utility is to simulate fluctuation of the sun's irradiance at high concentration on a cell in an accelerated manner. The application should leverage the XT-30's ability to produce high concentration irradiance on a small surface area and its shutter should be used to cut-off the irradiance on the cell at relatively fast rates. The utility should be designed to accept scheduled commands and run in an automated fashion with little or no human supervision. It should record a spectrum using the spectroradiometer, take an IV curve using either a Kepco or Keithley source meter, move the XT-30 beam output across stages and actuate a servo to open and close the XT-30 shutter using a parallel port interface. The application features should include:

- record and store spectrum,
- record and store IV curves using either a Keithley or a Kepco source meter,
- move the beam output using the Vemex controller across stages,
- actuate a servo to open or close the XT-30 shutter,
- implement a scheduled wait in seconds,
- allow time relative scheduling of each operable feature and
- allow saving and loading of schedules.

3.1.2.4.2 Method / Description

Labview was chosen as the application development platform for this utility due to its relative ease of use and deployment. A c++ platform was also used to create an application library to communicate with a parallel port. The utility was designed in two parts: one for system setup and one for actual use. The system setup design was made for the initialization of connections to the Vemex controller and the power supply meters as well as configuration setting for the source meters (described in section 3.1.2.1.2). The actual scheduling or running of simulations was access restricted based on conditions that must be met, such as availability of a connected source meter.

Upon application launch, source meter setup and configuration are done and a subsection is launched. The subsection provides an interface to perform the actual target operation and an initialization procedure to enable or disable features based on whether certain hardware are connected and operable. A finite state machine structure was used to coordinate operations. The application uses the IV curve module described earlier (in section 3.1.2.2.1.2). Similar modules were created for other segmented tasks, which include moving the XT-30 beam output using the Vemex controller to any given X and Y coordinate, taking a spectrum measurement using the spectroradiometer, and opening or closing the XT-30 shutter by broadcasting a binary command over the network. For the purpose of simplicity, explicit details of the mode of operations of each respective module created have been omitted. A c++ application library was created to accept broadcast messages and transfer the binary content to a parallel port. The parallel port was connected to a servo circuit for opening and closing the XT-30 shutter.

Each feature available in the utility after its initialization phase, besides the wait action, is designed to be operated with and without a scheduler. This allows for application flexibility if manual operation is required. Controls on the application allow for data results, in the form of IV curve data or spectrum data, to be save to file. Scheduling actions involve adding the required action step by step to a schedule list on the utility. The list can be edited by deleting individual or bulk actions and it can be saved and loaded to and from a persistent file. For each action scheduled, a memory space is allocated to store parameters unique to the action (such as X and Y coordinate for a Vemex controller movement, or specific source meter

configuration settings for an IV curve measurement). A blank memory space is also created for each scheduled action to record the status and result of the task once completed.

Once a schedule is initiated, a prompt is presented to the utility user to save a spreadsheet file that would contain the operation results. Subsequently, each operation is run in a top-down approach from the schedule list and the status of the operation with or without a result is inserted into the spreadsheet file. Features were also designed and developed to pause, resume and stop the schedule while running.

3.1.2.4.3 Result

The application has been used since March 2013 with the XT-30 solar simulator to apply light cycling on high concentration solar cells, delivering at least 8000 light cycles at 5 seconds intervals with a dark IV curve every hour. Figure 3-11 presents the application interface. Various options are available via the utility. For example, varying the open and close duration of the shutter on the XT-30 over the course of a light cycling experiment could increase or decrease the temperature ramp rate.

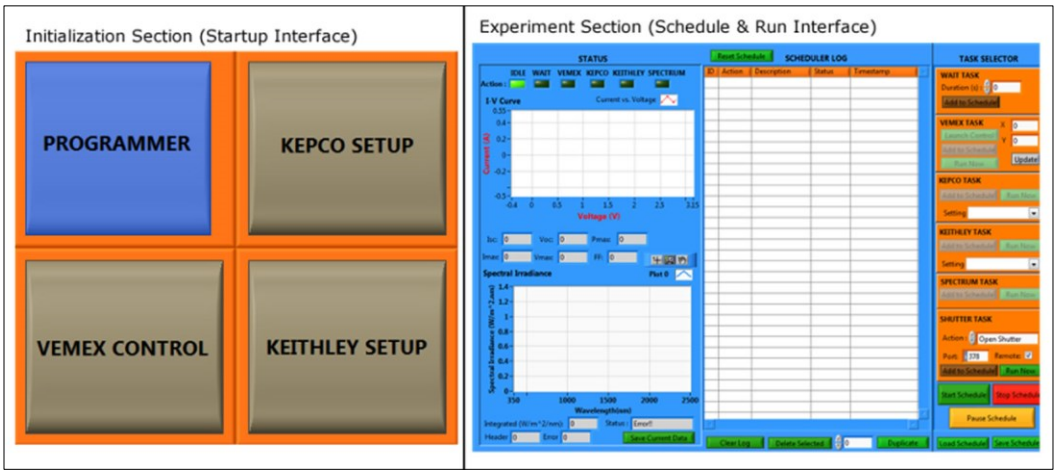

Figure 3-11: The two main interface of the Light Cycling Utility (not to scale).

3.2 Data Logging and Databasing of APECS Datasets

The theory of CPV systems suggests that the technology is sensitive to spectral variation of the incident solar resource (see section 1.1.4). There is thus a need to optimise cell EQE for location specific deployment of CPV systems to address such spectral variations. Performance evaluation through simulations of PV systems is therefore necessary to

characterise system behaviour over time. In particular, for energy yield evaluation, there is a need for solar resource data of high temporal granularity. The need to scientifically evaluate CPV technology in the field was a key driver of the *Advancing Photonics for Economical Concentration Systems* (APECS) project, for which a solar test site was built to evaluate the performance of prototype CPV technologies in light of calibrated measurements of site-specific meteorological data (such as direct normal spectral irradiance, direct normal irradiance and global horizontal irradiance) acquired at 2 minute intervals.

3.2.1 Overview of APECS, Test Site and Databasing Architecture

The *Advancing Photonics for Economical Concentration Systems* (APECS) project is a program for studying high efficiency CPV systems to advance their economic viability for grid connected solar power. It began early in 2011 and is funded though the "Ontario Research Foundation – Research Excellence" program, in partnership with the University of Ottawa and Morgan Solar Inc. As part of this project, a test site was set up at the University of Ottawa, located on the roof-top parking lot of the University's sport complex (45.4194˚N, 75.6769˚W), as shown in Figure 3-12. The site accommodates two dual-axis trackers mounted with both CPV and PV systems, and instruments for measuring direct normal irradiance (DNI) and direct spectral irradiance. A CCD camera to record images of cloud conditions around the solar zenith is also installed on the tracker. Instruments for measuring global horizontal irradiance (GHI), wind speed and ambient temperature have been set up on the site.

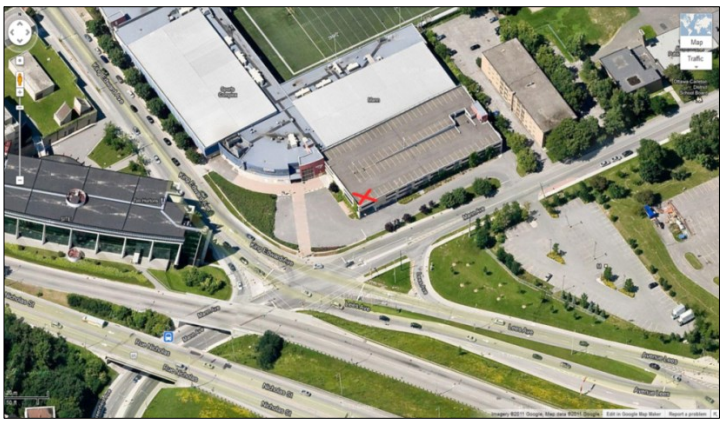

Figure 3-12: Google map satellite image of the environs around the sports complex of the University of Ottawa. The red cross indicates the location of the APECS test site.

3.2.2 Measuring Instruments

Most data at the test site is recorded once every two minutes. This includes GHI, DNI, spectra and cloud cover image. The task of storing the data was made possible through a series of connections between software and hardware systems. The electrical and structural hardware design is outside the scope of this discussion; however, a full description has been published elsewhere [50]. Instruments for measuring the GHI, DNI and spectra include an Eppley pyranometer, Epply NIP Pyrheliometer and ASDi spectroradiometer respectively. The tracker used is a GoldenSun dual axis system. Table 1 presents the specifications of the instruments.

Equipment	Specification
Eppley PSP Pyranometer	ISO Secondary Standard
Eppley NIP Pyrheliometer	ISO Secondary Standard
ASDi Spectroradiometer	350 – 1830 nanometer averaged to 1nm resolution
GoldenSun Tracker	Dual axis, tracking accuracy 0.1˚ to 0.2˚

Table 1: Basic specifications for some instruments on the APECS test site.

3.2.2.1 Eppley PSP Pyranometer

The Eppley Precision Spectral Pyranometer (PSP), a product of Eppley laboratory Inc., is a radiometer capable of measuring the total or defined broadband wavelength of sun and sky irradiance. The instrument is presented in Figure 3-13. Irradiance detection is possible through a circular multi-junction wire-wound thermopile which has the ability to withstand severe mechanical vibration and shock. The receiver is coated with Parson's black lacquer which has a non-wavelength selective absorption. On the instrument, there are two removable hemispheres of Schott optical glass. The hemispheres are made of clear WG295 glass which is uniformly transparent to energy between 0.285 to 2.8µm. A spirit level is built into the instrument and an adjustable leveling screw (visible in Figure 3-13) is available to align it. A desiccator is also included in the pyranometer to keep the optics free of moisture [51]. Measuring the GHI data from the Eppley pyranometer is performed through an ADC voltage reference measurement along its output. The instrument is built with cast bronze and its guard shield (top cover) is enameled in white. Calibration of the Eppley Pyranometer compensates for temperature [51]. Table 2 lists some of the manufacturer's specifications.

Figure 3-13: The Eppley PSP Pyranometer.

Criteria	Specifications
Sensitivity	~ 9μV/Wm^{-2}
Impedance	~ 650 Ohms
Temperature Dependence	±1% over ambient temperature range (-20˚C to +40˚C)
Linearity	±0.5% from 0 to 2800Wm^{-2}
Response Time	1 second
Cosine Reception	±1% from normalization 0-70˚ zenith angle ±3% 70-80˚ Zenith angle

Table 2: Eppley Inc. specifications for the PSP pyranometer.

3.2.2.2 Eppley NIP Pyrheliometer

The Eppley Normal Incidence Pyrheliometer (NIP) is also a product of Eppley Inc. and measures absolute solar radiation at normal incidence. It is a standalone instrument without moving parts, and it requires a tracker to keep it pointed at normal incidence to the sun. The pyrheliometer's detector, at the bottom of the instrument (top-left area of Figure 3-14), is a wire-wound thermopile. The tube preceding the detector has diaphragms to create baffles and its inner surface is blackened to reduce reflectivity. The aperture ratio is 1 to 10 of its length, with the opening subtending an angle of 5˚43'30''. The pyrheliometer is filled with dry air at atmospheric pressure and sealed at the viewing end with a 1mm thick *Infrasil II* window. Flanges at each end of the pyrheliometer tube provide a target to aid in aiming the instrument at the sun. Similar to the Eppley pyranometer, the pyrheliometer's calibration is compensated for temperature and traceable to the world radiation reference. Table 3 presents some of the manufacturer's specifications.

Figure 3-14: The Eppley NIP Pyrheliometer.

Criteria	Specifications
Sensitivity	~ 8μV/Wm^{-2}
Impedance	~ 200 Ohms
Temperature dependence	±1% over ambient temperature range (-20˚C to +40˚C)
Linearity	±0.5% from 0 to 1400Wm^{-2}
Response Time	1 second
Calibration Reference	Eppley primary standard group of pyrheliometers.

Table 3: Some of the manufacturer's specifications for the Eppley NIP pyrheliometer.

3.2.2.3 ASDi FieldSpec3 Spectroradiometer

Spectroradiometers are instruments for measuring light intensity as a function of wavelength. It produces data which corresponds to the spectral distribution profile of irradiance with absolute power measurement. The ASDi Fieldspec3 spectroradiometer (Figure 3-15) is an integrated system designed for a range of applications in spectroscopy. It uses multiple detectors (silicon and thermoelectrically cooled InGaAs) for measuring a broad wavelength band of the spectrum. It supports Ethernet connections and thus is suitable as a remote sensing system. Some specifications by the manufacturer are presented in Table 4.

Figure 3-15: The ASDi FieldSpec3 Spectroradiometer.

Criteria	Specifications
Spectral Range	350-1830nm
Spectral Resolution	3nm @ 700nm 10nm @ 1400nm
Sampling Interval	1.4nm @ 350-1050nm 2nm @ 1000-1830nm
Operating Temperature	0˚C to 40˚C

Table 4: Some of the manufacturer's specification for the ASDi FieldSpec3 spectroradiometer installed at APECS test site at the University of Ottawa.

3.2.3 System Design

A single tracker on the test site has been dedicated to pyrheliometer, spectroradiometer and camera instrumentation to measure events along the solar zenith. Figure 2-16 provides a full view of the tracker in question, with a closeup of the instrumentation shown below in Figure 3-16. The spectroradiometer was partially disassembled to be installed in a temperature controlled housing. The temperature control mechanism is made up of an electric heater and a thermostat setup with conduits along a looped active airflow to keep the spectroradiometer housing above 5˚C. A cosine receptor was mounted on the instrument plate of the tracker and iswas connected to the spectroradiometer through a fibre optic cable. A direct attachment that limits sunlight on the cosine receptor to its direct component was then mounted on the cosine receptor. Parts of the instrument that make up the system are presented in Figure 3-17. A connection for recording data from the spectroradiometer was setup through an Ethernet cable that was networked to an indoor computer in the SUNLAB laboratory

Figure 3-16: Instrument panel on a tracker at the APECS test site. (a) Spectroradiometer attachment. (b) Eppley NIP pyrheliometer; (c) CCD camera and (d) temperature controlled ASDi housing for spectroradiometer environmental stabilization.

Figure 3-17: Parts of the spectroradiometer setup on the tracker at the site. The spectroradiometer from Figure 3-15 has been partially disassembled to fit into an environment controlled housing. (A) The spectroradiometer; (B) The cosine receptor; (C) The direct attachment; (D) The housing for mounting the spectroradiometer; (E) A flexible fiber optic cable which connects the spectroradiometer to the cosine receptor. Adapted from [15].

Similar to the spectroradiometer, data from the camera is also being recorded through a networked Ethernet connection on a computer in the laboratory. Data from the pyrheliometer, pyranometer and module monitoring systems is recorded through a Campbell scientific data logger (model number CR1000). The data logger takes ADC reference voltage measurements from the pyrheliometer and pyranometer which are recorded to text files with timestamps.

3.2.4 Data Logging and Backup Architecture

Large datasets were expected from the instruments on the test site since the goal of the measurements was to acquire highly temporal data. Storing and accessing such large datasets required significant information technology (IT) infrastructure to ease memory management, data retrieval efficiency and data backup. To this end, a dedicated server was set up to handle the collection, storage and retrieval of research data gathered from the APECS test site. Custom computer software gathered the data from the spectroradiometer and camera to binary files stored on disk. Text files with data from the pyrheliometer, pyranometer and prototype modules were similarly generated and stored on disk using Campbell scientific data logger software. Subsequently, a relational database (Microsoft SQL 2005), carefully tuned for optimization of memory and speed in read and write operations, was populated with data from the binary and text files by a scheduled custom script. A website hosted on the server (apecs.site.uottawa.ca) provides remote access to the data.

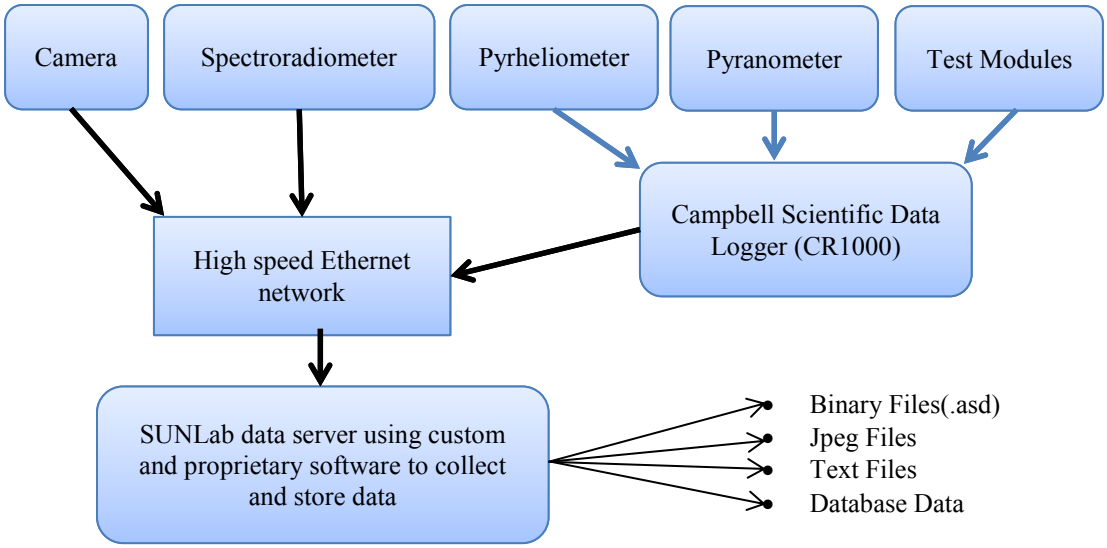

Figure 3-18: Diagram illustrating data collection and storage procedure between the SUNLAB data server and the APECS test site.

3.2.5 Measurements

The objective of the test site instrumentation and database design was to collect and archive spectral radiation, direct and global horizontal irradiance and other meteorological data in a database made across a range of air mass values and atmospheric conditions applicable to concentrated photovoltaic (CPV) systems. Measurements carried out across a range of air mass values allow the impact of factors that contribute to modifying the direct beam to be individually understood. Details of the temporal relationship between air mass and the solar zenith have been presented in section 2.4. We recall that the important atmospheric variables with the highest impact on the spectral radiation distribution and solar irradiance are cloud cover, perceptible water vapour, barometric pressure and atmospheric turbidity (aerosol optical depth). With proper instrumentation these variables can be independently measured, however methods also exist to accurately resolve some values from other instrument measurements such as spectral irradiance.

The sun-facing camera mounted on the tracker provided suitable data for resolving the cloud cover index which indicates the degree of obstruction of direct light. The tracker-mounted spectroradiometer also provided a means to resolve the frequency-dependent aerosol optical depth and perceptible water vapour from absorption profiles in the measured spectral data.

Measurements taken at two minute sampling intervals of DNI, direct spectral radiation, sky cloud condition and GHI began in March 2011, April 2011, November 2011 and January 2013, respectively, and have continued to date. Occasionally, for periods of time ranging from a few minutes to several weeks, some data were not recorded due to instrument calibration, system upgrade, network failure or software error. The spectroradiometer also had to be repaired over the measurement period. Stringent maintenance procedures were implemented to clean, align and calibrate the instruments to ensure data accuracy. Figure 3-19 illustrates the worst case scenario noted for data bias due to dirt and misalignment of the pyrheliometer, which measures integrated intensity. Through cleaning and alignment was performed after a period of non-maintenance that lasted for approximately 7 months, and the data were taken during a sunny period with clear sky conditions.

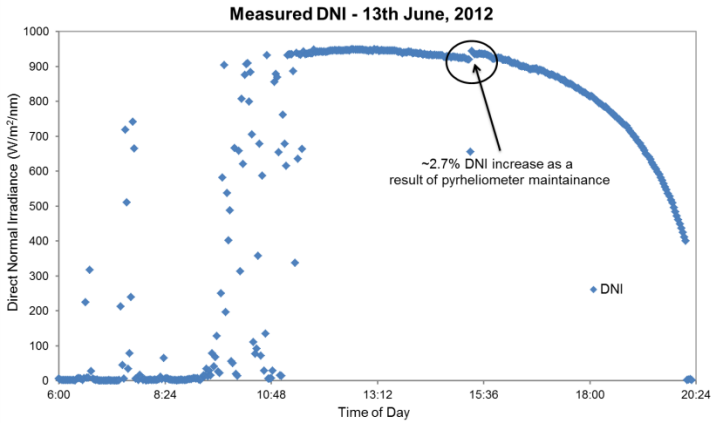

Figure 3-19: Measured DNI as a function of time from the APECS test site taken on the 13th of June 2012. The anomaly in the recorded irradiance showed an increase in DNI of approximately 2.7%.

Neglecting spectroradiometer maintenance has a greater impact on the quality of spectral measurements than neglecting pyrheliometer maintenance does on the quality of direct intensity data. Spectroradiometer maintenance requires cleaning and aligning the direct attachment and cosine receptor's detector but several factors makes the cosine receptor's detector more sensitive to contaminants deposited on it. The DNI data are very sensitive to directional misalignment given the aperture size of the direct attachment. Furthermore, experience showed that the deposition of rain, snow and dust on the cosine receptor's detector significantly biased the spectroradiometers measurements. These concerns were addressed with a maintenance procedure for all instruments scheduled on a biweekly basis.

Acquisition timelines for data measured and recorded in the APECS system database from the project's inception to the 19th of April 2013 are represented in Figure 3-20 by both their present and absence. The complementary representation attempts to overcome the limited point density of the plot, relative to the extremely high data density. Approximately 375,000 spectra, 530,000 DNI with concurrent meteorological data and 60,880 GHI datasets are represented in the figure. Data quality control was performed to exclude erroneous measurements and an interactive web-script was developed to provide an easy interface for data access (http://apecs.site.uottawa.ca/data-return-form/).

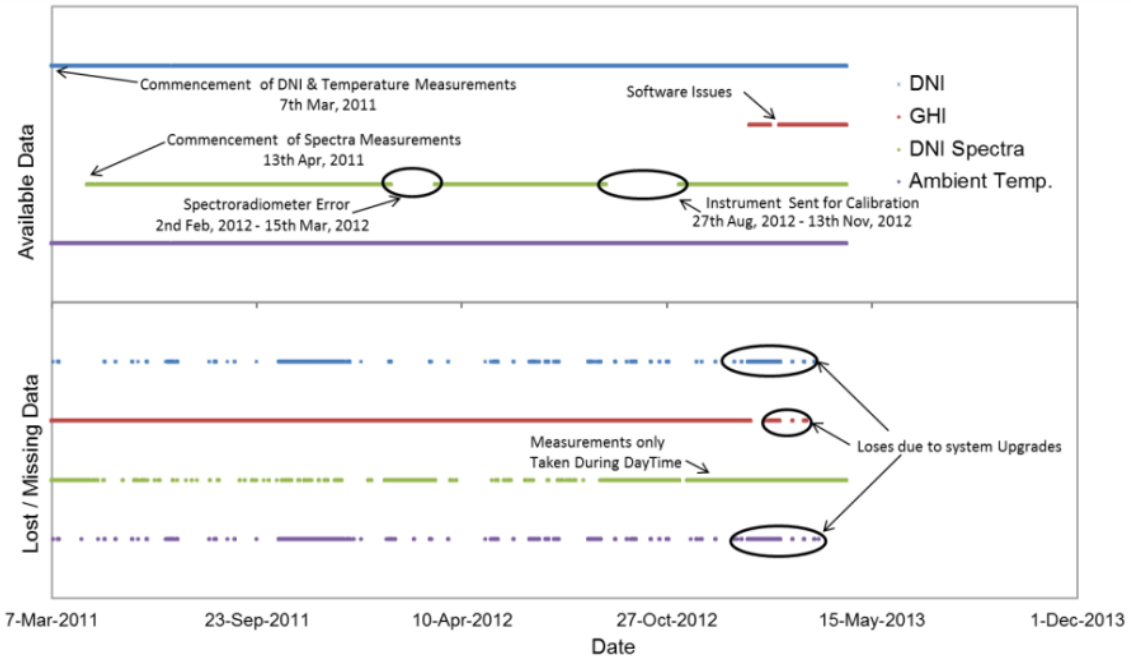

Figure 3-20: Graph illustrating a timeline for data collected and stored from the APECS test site. The data available and accessible in the database from the commencement of measurements to the 19th of April 2013 is represented. Factors responsible for major data losses are highlighted.

3.3 Photovoltaic System Simulation

There is a critical need for modeling and simulation tools. A solar cell of any given number of junctions may be modeled by various methods. Simple methods, such as EQE convolution with the solar irradiance, require less computation (and are less detailed) than complex methods, such as the simulation of electron-hole transport. If system parameters of a given accuracy will suffice, then a trade off between computational speed and detailed system response may be made. The single diode model has been shown to yield good agreement with system measurements [15], and its parameterization is sufficient for our purposes – each

subcell being represented by its own model. Using this model, extensive simulations may be made within reasonable time periods. Using the Java programming language, an object oriented implementation that used parallel programming methods was developed to decrease simulation times.

3.3.1 Review of the Single Diode System Model

In its simplest form, a solar cell may be represented by an equivalent circuit comprised of a current source, a diode, and series and shunt resistances, as illustrated in Figure 3-21. The single diode model allows the extraction of an IV characteristic curve from the equivalent circuit of a solar cell. This characteristic is the sum of the fundamental response of the diode and its response to illumination. The former represents the cell response in the absence of illumination, and is given by the ideal diode equation as

$$I_d = I_0 \left[\exp\left(\frac{qV_d}{nk_BT}\right) - 1\right], \tag{32}$$

where I_d is the diode dark current, I_0 is the saturation current, q is the elementary charge, V_d is the diode voltage, n is the ideality factor, k_B is Boltzmann's constant, and T is the temperature of the diode. Equation (32) produces a diode characteristic curve.

If the solar cell is illuminated, the IV characteristic curve shifts down because electrical power is being produced due to photon absorption (see Figure 3-22). If I_L is the response of the current source representing cell illumination, then application of Kirchhoff's laws yields the modeled IV characteristic as

$$I = I_L - I_0 \left[\exp\left(\frac{q(IR_S+V)}{nk_BT}\right) - 1\right] - \frac{IR_S+V}{R_{sh}}, \tag{33}$$

where R_S is the series resistance in the cell and R_{sh} is the shunt resistance across the cell. These parameters derived from a combination of non-ideal factors such as carrier recombination, semiconductor imperfections and wire bond issues on a solar cell, and are zero and infinity respectively for ideal cells. Numerical methods are usually exploited to solve this transcendental equation. Note that the polarity of the current has been reversed in equation (33) to be consistent with power production. This mirrors the IV characteristic across the voltage axis, with the representation now in quadrant 1 rather than in quadrant 4, as illustrated in Figure 3-23.

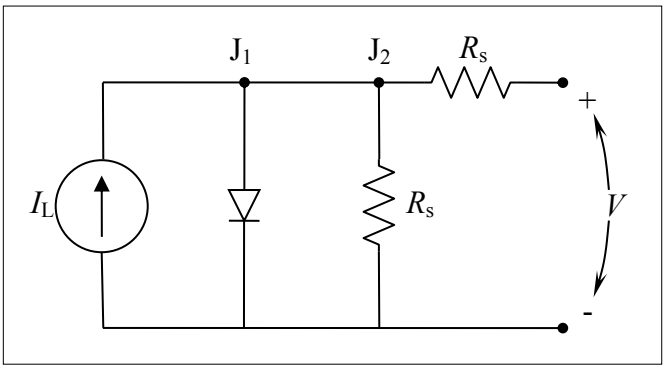

Figure 3-21: Equivalent circuit for a single junction solar cell. Adapted from [15].

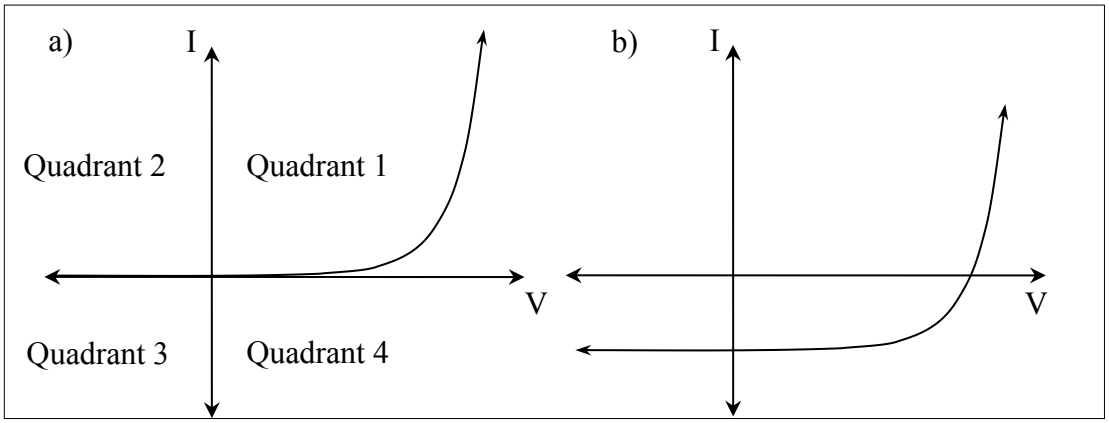

Figure 3-22: Current – Voltage curves for an ideal solar cell. a) Represents a dark IV curve where no illumination is present on the solar cell. b) Represents a light IV curve which has been illuminated. Adapted from [15].

For solar cell applications, key descriptors of an IV curve are the short circuit current (I_{sc}), the open circuit voltage (V_{oc}), the maximum power point (P_{max}) and the fill factor (FF). These system parameters provide the bulk of information necessary for performing cell analysis or evaluation. The short circuit current is the current at the point on the IV curve where the bias voltage is set to zero and it denotes the maximum current a cell can produce. The open circuit voltage is the voltage at that point on the IV curve where the overall current is zero. The maximum power point represents the point on the IV curve where the product of the current $I_{mp}$and voltage V_{mp} yields the maximum power. The fill factor (FF) is a ratio of the solar cell's maximum power, relative to the equivalent ideal current source, as

$$FF = \frac{I_{mp}V_{mp}}{I_{sc}V_{sc}}. \tag{34}$$

These parameters are presented in Figure 3-23.

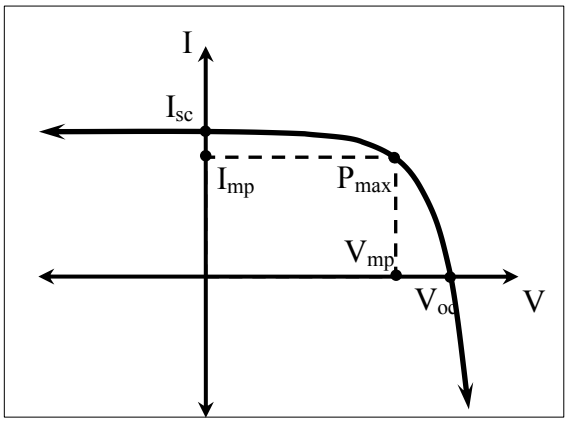

Figure 3-23: A cell IV curve shifted to the first quadrant, illustrating points corresponding to the short circuit current, open circuit voltage and maximum power. Adapted from [15].

3.3.2 Modeling Multi-Junction Cells

A modeling procedure for a triple-junction solar cell based on the single diode solar cell model was published in [15]. The procedure models a triple junction cell with an equivalent circuit diagram illustrated by Figure 3-24. Temperature controlled measurements were taken from real triple junction isotypes and the characteristics of the shunt and series resistance for each sub-cell were extracted.

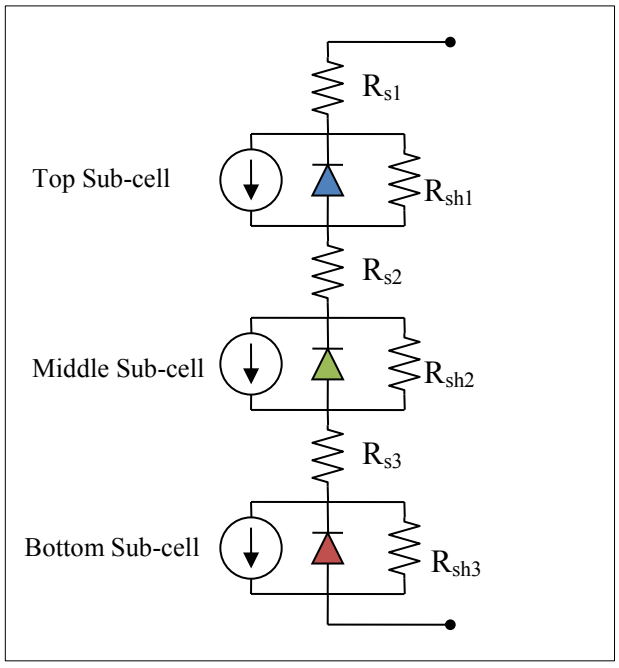

Figure 3-24: Equivalent circuit representation of a triple junction solar cell. Adapted from [15].

The model addresses the temperature dependence of the external quantum efficiency, using the Varshni equation [32] to calculate the temperature-dependent band gap energy for each sub-cell as

$$E_g(T) = E_g(0) - \alpha \frac{T^2}{T+\beta}, \tag{35}$$

where $E_g(0)$ is the band gap of the sub-cell at 0 K, T is the temperature of the semiconductor (K) and α & β are material parameters. The wavelength-dependent EQE for each sub-cell was then temperature corrected by an amount equivalent to the difference between the reference band gap and the shifted band gap.

The magnitude and wavelength dependence of the light incident on the CPV system is altered by the optical components that deliver it to the cell. This change is quantified by the system's optical transfer function (OTF), which is the wavelength-dependent ratio of the transmitted irradiance to the incident irradiance. To calculate the photogenerated current density for each subcell, the EQE therefore needs to be scaled by the OTF. For incident irradiance $I(\lambda)$ and photon energy E_{ph}, the photocurrent density is (36)

$$J_{ph} = q \int \frac{I(\lambda)}{E_{ph}(\lambda)} * OTF(\lambda) * EQE(\lambda, T)\, d\lambda, \tag{36}$$

where q is the electron charge constant. Having deduced the photocurrent density for each subcell, application of the diode model as described by equation (33) allows each subcell JV characteristic to be given in terms of its series and shunt resistances as

$$J = J_{ph} - J_0 \left[\exp\left(\frac{q(JR_s+V)}{nk_BT}\right) - 1\right] - \frac{JR_s+V}{R_{sh}}. \tag{37}$$

The final JV curve for the combined triple-junction system can be deduced from the sum of the three sub-cell JV curves. Since the subcells are electrically connected in series, as illustrated in Figure 3-24, the cell voltage is the sum of the sub-cell voltages, while its current (at each voltage) is that of the least-producing subcell.

4 Spectral Estimation and Energy Yield Analysis

Two major research results are presented in this chapter: The first describes a method to acquire spectral datasets through the design and implementation of a model, extending results published by Harrison and Michalsky [52], that parameterises the aerosol optical depth (AOD) from spectral measurements. The purpose of the extended model is to generate time resolved clear sky spectra for any specified location. The second is an analysis aimed at discovering the impact of meteorological effects on long term energy yield predictions.

4.1 Spectral Estimation Using Parameterized Aerosol Optical Depth

The design and operation of PV systems depends on the nature of the local solar resource. For CPV systems, the local DNI is the key component of the solar resource responsible for photocurrent generation. Long term local measurements of spectral DNI are essential for assessing CPV system response at any particular site [53]. However, setting up systems to measure the spectral distribution of the solar resource at every potential CPV site is economically unviable due to time requirements and spectroradiometer costs. Wide area satellite meteorological measurements are sometimes used as an input to radiative models, but these only provide low resolution spectral irradiance of insufficient temporal granularity. However, ground based measurements of meteorological conditions with less expensive instruments can be used as an input to radiative models. One such model, a "Simple Model for the Atmospheric Radiative Transfer of Sunshine version 2" (SMARTS2), has been developed to describe average local radiation [54, 55]. It treats the optical depth of the atmosphere in terms of its individual components, such as Rayleigh scattering, gaseous absorption and aerosols.

Using SMARTS as a base model, the clear sky DNI for the APECS test station in Ottawa was predicted and assessed using an extended method for extracting AOD from measured spectra. Meteorological data gathered from various sources, such as the Canadian Weather Energy and Engineering Data Sets (CWEEDS), were used to achieve this goal. Simulating solar spectra with SMARTS2 is straightforward; the primary concerns are the locally sensitive inputs to the model, and the AOD in particular.

SMARTS2 provides built-in algorithms for deducing an atmospheric constituent's optical depth from basic meteorological data. For example, perceptible water vapour can be calculated from temperature, atmospheric pressure and humidity data. In place of meteorological measurements of the optical depth of atmospheric gases, the model typically uses the concentrations of gases in the atmosphere to calculate individual absorptive profiles. One exception is the determination of the AOD. Unlike basic meteorological parameters that can be easily measured with conventional instruments, the wavelength dependence of the AOD depends on the local distribution of particle sizes in the atmosphere and its direct measurement is nontrivial. The temporal profile of the AOD is never particularly constant, especially in urban areas due to the varying atmospheric concentrations of dust, smoke and smog. For convenience, SMARTS2 makes use of the angstrom parameter to extrapolate a known AOD (τ_{λ_0}) at a particular wavelength (typically, 500 nm or 550 nm) to other wavelengths. This parameter is defined by

$$\frac{\tau_\lambda}{\tau_{\lambda_0}} = \left(\frac{\lambda}{\lambda_0}\right)^{-\alpha}, \tag{38}$$

where τ_λ is the optical depth at the required wavelength.

4.1.1 Optical Depth Extraction Algorithm

An algorithm for extracting optical depths from ground based measurements [52] was further developed to extract optical depths from time resolved measured spectral DNI under clear sky conditions. The hypothesis that spectral DNI may be adequately simulated on the basis of single-frequency AOD extraction from clear sky spectral irradiance was self-consistently tested against its generating spectra. The extraction process begins with the Langley regression, which is a linear regression applied to Bouguer's law.

Bouguer's law describes the attenuation in intensity of light traversing a uniform medium as

$$\frac{I_\lambda(x)}{I_\lambda(0)} = exp^{-\tau_\lambda x}, \tag{39}$$

where I_λ is the measured DNI at wavelength λ, x is the path length traversed by the light (which may be expressed as an air mass), and τ_λ is the optical depth for the specified wavelength [52]. It is necessary to calculate the air mass as a function of time of day and year. The high precision solar calculation algorithm presented in section 2.4.1 was used to do

so, employing earth obliquity corrections and refractive corrections as stipulated in Kasten's approximation [55]; see also section 2.3. Using linear regression, Bouguer's law has the form

$$\ln I(\lambda, x_n) - \ln I(\lambda, 0) = -\tau x_n \,, \tag{40}$$

where I is the received DNI as a function of wavelength λ and the path length x_n. A best fit line was then used to determine the value of $I(\lambda, 0)$ which corresponds to the extraterrestial spectral irradiance where the optical depth is zero. Our optical depth extraction algorithm is similar to the objective Langley regression algorithm stipulated by L. Harrison and J. Michalsky [52], with minor modifications to the data filtration and sampling details.

Typical DNI spectra are presented in Figure 4-1, one for air mass zero and one for air mass 1.5. The regions highlighted are areas strongly affected by atmospheric constituents that contribute to the overall optical depth. The corresponding input parameters in SMARTS2 that affect the magnitude of absorption in these regions are shown.

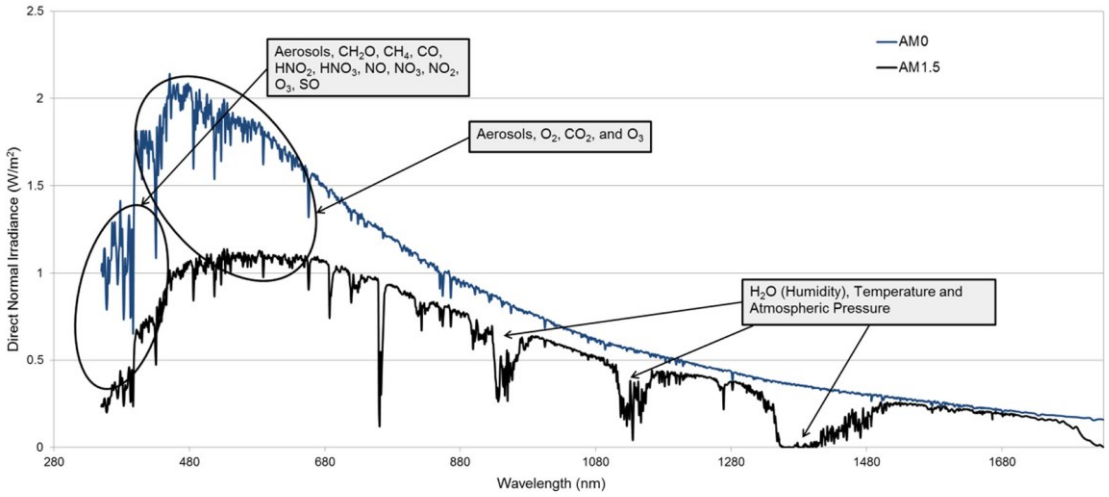

Figure 4-1: The AM0 (extraterrestrial, blue) and AM1.5 (terrestrial, black) spectra, with illustrations of spectral regions where particular atmospheric constituents dominate absorption.

Figure 4.2a presents the integrated spectral DNI (the irradiance) from morning to evening of 11 May 2012. The timestamp can be converted into air mass values, and the rectangular regions delimit the 2 < AM < 6 regions, where the rate of change of DNI to air mass is greatest. The natural logarithm of the 500 nm DNI is shown in Figure 4-2b as a function of the air mass. Substantial deviations from linearity are a result of minor cloud cover. Since the optical depth extraction algorithm is predicated on the near-clear-sky conditions, such data areas need to be excluded from the calculations.

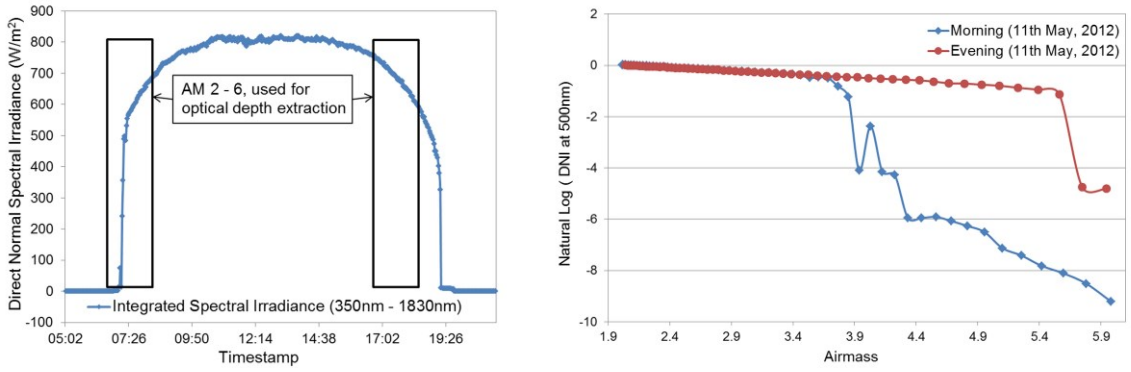

Figure 4-2: (a) Integrated spectral irradiance as a function of time (left) on the 11th of May 2012. (b) The corresponding natural logarithm of the irradiance for the marked sections between air mass 2 and 6 (right).

To perform the Langley regression, a series of data filtering procedures were applied to remove data points influenced by cloud cover. The details of the procedures have been published elsewhere [52]. Data of the afternoon period were processed and the results shown in Figure 4-3, with the data initially filtered between 2 < AM < 6 again presented in the top-left plot. The next two filters remove data points affected by the onset and termination of cloud coverage: the top-right plot shows the result of the former, where points showing positive gradients in the DNI profile have been removed; the bottom-left plot shows the latter, where data points with negative gradients greater than twice the mean have been removed. A final filter is employed to further minimize error, removing all data points with standard deviations greater than 1.5 from the nominal regression line. The final dataset is shown in the bottom-right plot of Figure 4-3. A least square regression fit as per equation (40) yields an AM0 DNI at 500 nm of 1.871W/m^2 and an optical depth of $\tau_{500nm} = 0.280$.

The procedure was repeated for wavelengths between 350 and 1300 nm at 1 nm spacing. The resulting optical depth τ_λ for each wavelength is shown in Figure 4-4. Three regions of interest are noted: the high frequency end corresponding to wavelengths between 350 nm and 550 nm, dominated by Rayleigh scattering; the mid-wavelength region between 550 nm and 1000 nm, with a predominantly monotonic dependence influenced by the aerosol distribution; and the long wavelength region greater than 1000 nm, where significant structure in the optical depth arises due to the strong water vapour absorption bands.

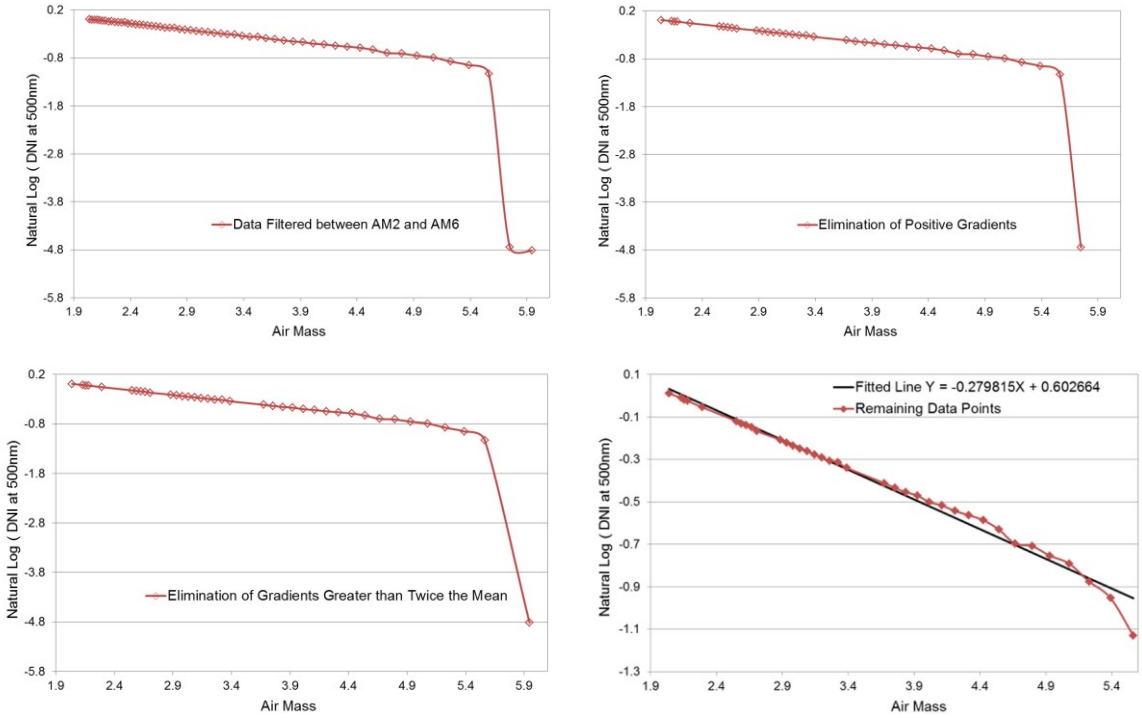

Figure 4-3: Top-left – Initial data, filtered to include only data points between AM2 and AM6. Top-right – Removal of data points with positive gradients. Bottom-left – Removal of data points with negative gradients greater than twice the mean of all gradients. Bottom-right – Removal of data points varying more than 1.5 standard deviations from a nominal regression line. The straight line is a final fit to the filtered data as per the Langley regression.

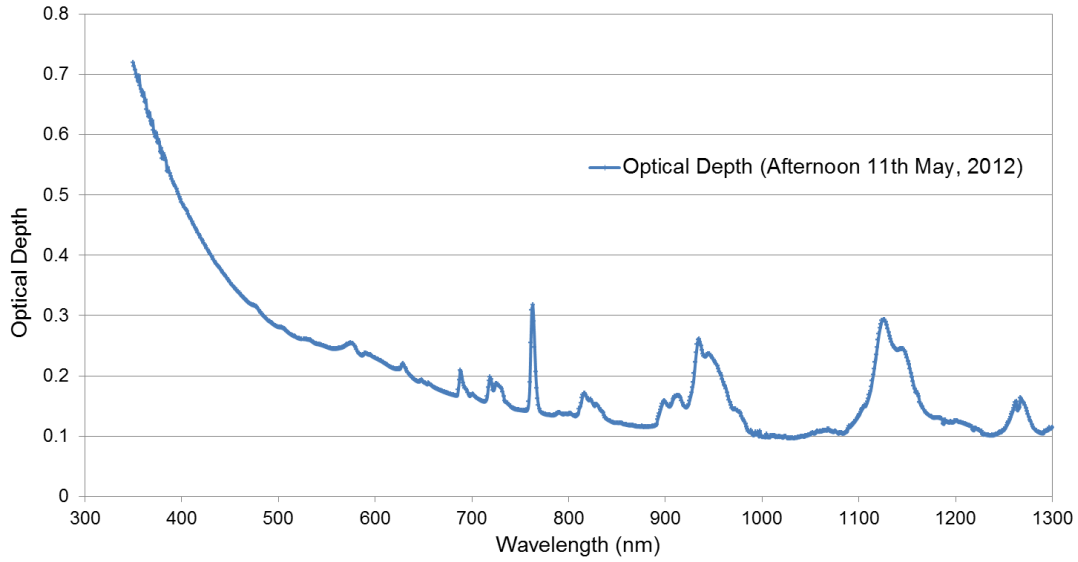

Figure 4-4: Optical depth as a function of wavelength calculated from measured spectra using an algorithm adapted from the Langley objective regression algorithm.

4.1.2 Aerosol Optical Depth Extraction

Spectral irradiance measurements taken on the late afternoon of the 13 June 2012, an afternoon with fairly clear sky condition (illustrated in Figure 3-19), were used to deduce an average optical depth for that period. First, meteorological and geographical input parameters were fed into SMARTS2 (on cards 2 – 8 for the relevant set of air mass values) to calculate a model spectrum, with AOD inputs (on card 9) set to zero. The optical depth algorithm was applied to the resulting spectra from this model to obtain an optical depth profile as a function of wavelength for zero aerosol contribution. Next, the measured spectra from the APECS test site (which corresponds to the air mass used for the SMARTS2 model) were fed into the optical depth algorithm to extract the site-specific AOD-containing optical depth profile. To ascertain this AOD, a wavelength-dependent subtraction between the optical depth derived from measured spectra and the optical depth derived from modeled spectra was carried out. The algorithm is summarized in Figure 4-5.

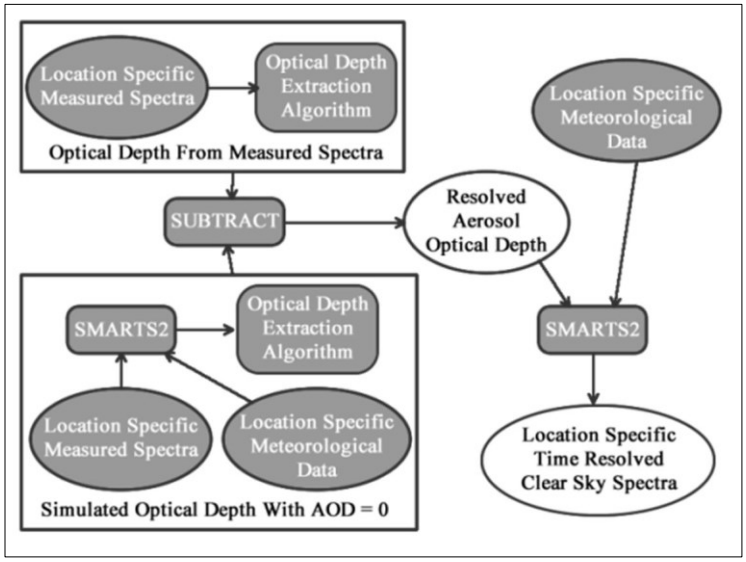

Figure 4-5: Block diagram illustrating the procedures implemented for calculating aerosol optical depth from simulated optical depth and its application to SMARTS2 to derive simulated sky spectra.

The results of the AOD extraction process are shown in Figure 4-6. The solid blue curve is the optical depth extracted from measured data, the red dashed curve is the simulated optical depth with zero AOD contribution, and the dotted green curve is the difference between the two, representing the AOD contribution to the optical depth. In the high intensity spectral region shown, the AOD is effectively flat implying that the choice of a frequency-independent AOD parameter in SMARTS2 is arguably valid. Furthermore, it

appears that the AOD smoothly decreases at high frequency, which is asymptotically anticipated. However, the purported values for the AOD in the vicinity of the water absorption bands are clearly spurious, implying that AOD does not linearly decouple from optical depth in the manner codified by SMARTS2.

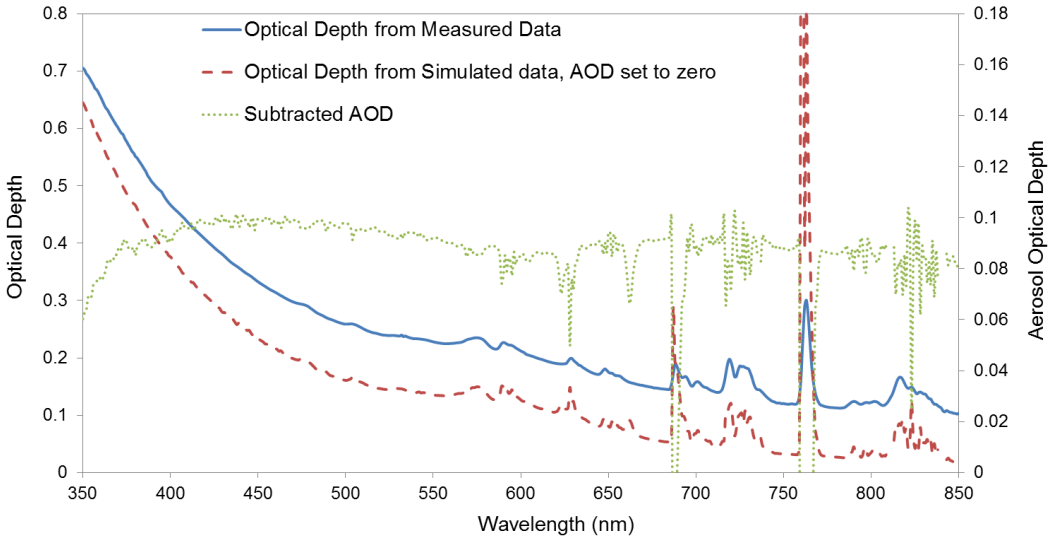

Figure 4-6: Optical depth calculated from spectral irradiance data (blue line), simulated aerosol-free optical depth (dashed red line). The difference between the two optical depths (dotted green line) represents the modeled contribution to optical depth due to aerosols.

Assessing the validity of the using a frequency-independent AOD to accurately simulate site-specific spectral DNI, the AOD at 500 nm as determined above was input into the SMARTS2 model, in conjunction with the previously mentioned meteorological and geographical parameters for the APECS Ottawa test site. Figure 4-7 presents the comparison between such simulated spectra and the actual measured spectra. The spectral mismatch between the measured (blue curve) and simulated (red curve) spectra is found to be minimal (within ±0.1 W/m^2, green curve) for most wavelengths. This validates our hypothesis.

Our AOD extraction algorithm is only valid for clear sky conditions and requires measurement of the solar spectral irradiance at 500 nm or 550nm. Under such condition, however, a broadband spectroradiometer is not necessary, and it could be replaced by a relatively cheap silicon detector with a band-pass filter 500 nm or 550 nm. The spectrum thus generated can reliably be used for energy yield calculations with considerable accuracy. This may be seen by comparing short circuit currents calculated using both modelled and measured spectra from Figure 4-7, assuming some typical EQE for a triple junction solar cell. The calculations are presented in Table 5 below, with their resulting percentage

differences for each sub-cell in a CPV system. Since the current produced by the cell is limited by the subcell with the lowest J_{sc}, using a single-frequency AOD value, in conjunction with local meteorological properties, to predict the local solar resource overestimates current production by only 0.56% in this case.

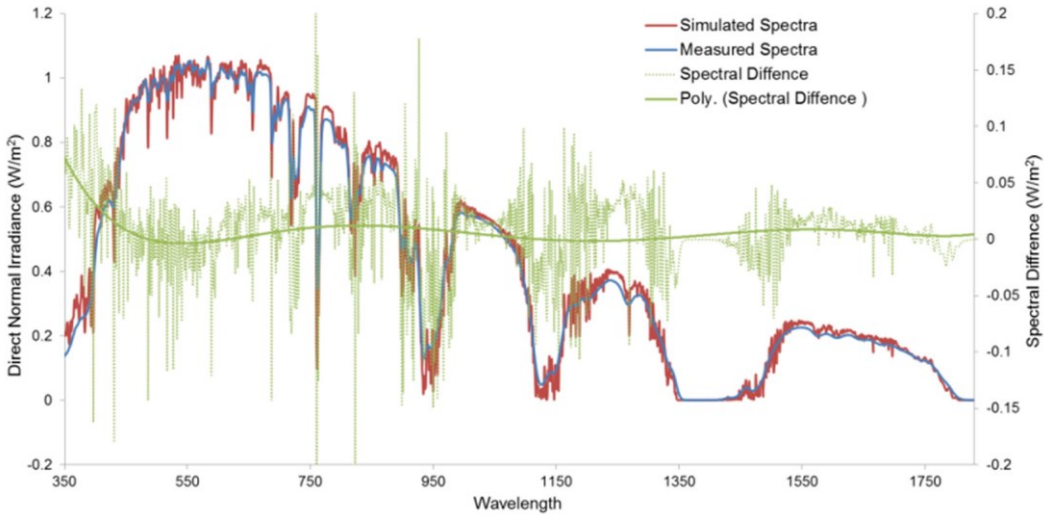

Figure 4-7: Measured DNI taking in the morning period of 2 July 2012 under clear sky conditions. Aerosol optical depth at 500 nm calculated using the method described above was input into SMARTS2 to simulate an equivalent clear sky DNI spectrum.

	Measured J_{sc}	Modeled J_{sc}	% Difference
Top Sub-cell	9.1723 mA/cm^2	9.2233 mA/cm^2	0.56
Mid Sub-cell	10.1831 mA/cm^2	10.4152 mA/cm^2	2.28
Bottom Sub-cell	15.0971 mA/cm^2	15.2361 mA/cm^2	2.72

Table 5: J_{sc} comparison in top, middle and bottom sub-cells between measured and modeled spectra based on data from Figure 4-7.

While the above illustration was for a particular case, and a single air mass, it suggests that predictive energy yield analysis based on simulated spectra may be possible for appropriate inputs, particularly if temporal aspects of AOD variation can be addressed. We have already noted that there is a significant difference in the averaged morning and afternoon optical depths, and that the true profile of the natural logarithm of the DNI as a function of air mass is actually polynomial, not linear. This indicates that the AOD is also variable. Further insights into the various factors that may bias predictive CPV energy yield evaluations are given in the next section.

4.2 Investigating Energy Yield Analysis

Energy yield analysis in the context of PV systems is associated with the determination of energy production over a given time period. It is often a predictive process to evaluate a potential PV site when planning, siting or financing PV installations. Where CPV is concerned, due to the nature of the technology, it is unknown if the current methods used for PV energy yield evaluation are directly applicable for all atmospheric conditions. This is because CPV optics focus only the direct sunlight component, unlike PV which uses global irradiance. The response of CPV to factors that affect its solar resource, such as cloud cover, aerosol and perceptible water vapour, needs to be investigated and properly understood. The literature [30] also documents that CPV cells are more spectrally sensitive to atmospheric variation than PV cells. This is of particular concern since the models used for PV energy yield evaluation do not need to address spectral variation.

In this section, a spectrally sensitive CPV model has been compared to a simple power – efficiency product model (commonly used for PV evaluation) under different temporal conditions to determine the presence and degree of bias in the use of simple models for CPV. The choice of dataset used for PV energy yield evaluation spatially and temporally is also investigated with an aim to de-convolute the degree of bias due to air mass variations, aerosols, cloud cover and temperature changes. Temporally measured spectral from the APECS test site (Ottawa, Ontario, Canada) between June 2011 and August 2012 was used for the analysis. Data from the Canadian Weather Energy and Engineering Data Sets (CWEEDS) and the Canadian Weather for Energy Calculation (CWEC) were utilized for long term sturdy and typical meteorological analysis respectively.

4.2.1 Introduction / Background

Recent breakthroughs in high efficiency multi-junction solar cells towards 40% efficiency [56] have driven interest in the use of CPV technology for developing utility-scale solar farms. With ever growing interest in renewable energy for sustainable development, the role of concentrated photovoltaics is bound to become more prominent in the global market [57]. CPV technology is fast becoming an economically viable option for utility-scale, clean renewable electricity in global regions with high annual direct solar insolation. Presently, over 360 MW of CPV generating capacity has been installed worldwide [58], and the trend

in development suggests that the drop in cost and rise in efficiency could permit economically viable use in some regions of Canada. For implementing CPV, the local solar resource must be considered when siting and financing projects, and adequate energy yield models are essential for the decision making processes.

CPV performance is dependent on its system efficiency profile, a function of the temporal solar resource and the cell and optics efficiency. System performance has been enhanced through cell tuning and customized optics [59]. The components of the optical assembly deliver the solar resource to the cell and each component has a frequency-dependent transmission efficiency known as the optical transfer function (OTF). For multi-junction CPV systems, cell current is limited to that of the least producing sub-cell. Optimally, light incident on the cells across all daylight air mass values should allow each sub-cell to produce a current that does not limit performance. Best CPV system performance may thus be achieved by tuning the solar cell and the system optical transfer function to the spectrum of the local solar resource over all air mass values. Methods to tune the solar cell for the standard spectrum have been reported [60, 61] and tuning a multi-junction cell to a location specific spectrum has been shown to yield better system performance [61]. Predicting the spectrum of the local solar resource requires proper understanding of the temporal behaviour of atmospheric and meteorological components such as clouds, perceptible water vapour and aerosols which affect the local solar resource. Where measured long term spectral DNI data are absent, as described in section 4.1, these components play an important role as inputs into atmospheric radiation transfer models such as SMARTS2.

PV system output must be sold into a very competitive market with cost as the dominant differentiator. Electricity providers such as Ontario Hydro are increasingly looking at ways to match generation to demand in the most economical manner. The use of incentives to reduce electricity consumption at peak hours is being implemented in Ontario and solar generated electricity is well suited to provide electricity when demand is at its peak. To assess economic potential under different pricing schemes, and to guide policy for incentive programs, it is important to determine energy yields at high temporal granularity. The inputs to energy yield analysis are key to levelized cost of energy (LCoE) calculations [62], the basis for financial analysis of utility-scale PV projects.

Financial calculators like PVWATTS and RETScreen, popular for non-concentrating flat plate PV systems, are of questionable utility for CPV because CPV energy yield models (i.e., OTF and cell response) have different sensitivities to local inputs. These sensitivities may be to certain meteorological parameters in terms of temporal power and spectral variations [63, 64], or more directly, due to the fundamental spectral sensitivity of the multi-junction cells themselves. The fundamental question then is how specific the spatial and temporal inputs to the model must be in order to yield an accurately predict energy production. In this section we quantify the impact of neglecting input variations on energy yield predictions, referenced to predictions deriving from measured test datasets, to estimate the bias in applying simple predictive methods dependent on long-term averages to CPV analysis. A more comprehensive financial assessment model is shown in Figure 4-8. The analysis described in this subsection constitutes the beginnings of this more detailed assessment model.

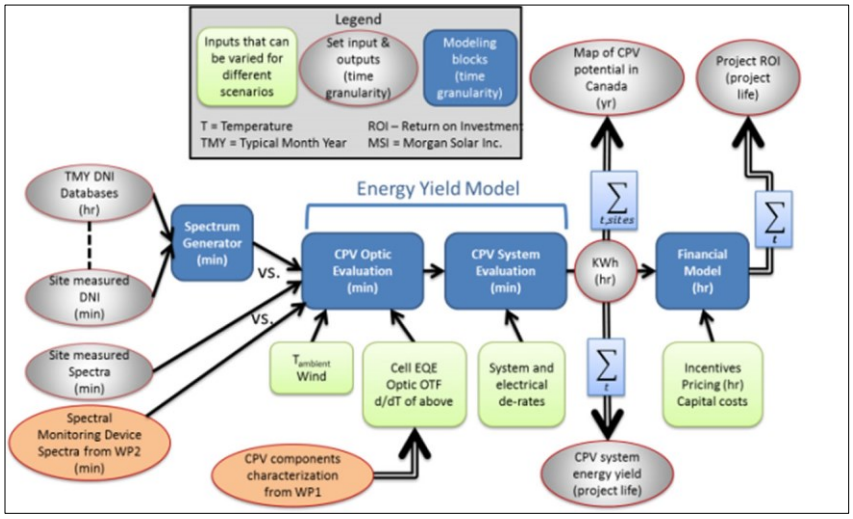

Figure 4-8: A sample CPV financial assessment block model that incorporates assesses energy yield inputs. The diagram is taken from the project proposal "Low Cost PV Energy Yield Analysis for Canadian and Global Locations" - CPVEYA).

4.2.2 Experiments and Analysis

A detailed CPV system model based on the algorithm in section 3.2 was developed using the Java programming language. It was extended to provide more generic functionality in order to test various combinations of input datasets and multi-junction cell configurations. Since large datasets were to be processed, the software used core parallel programming algorithms and relational database storage. Processed results were stored in a database to be retrieved and analysed for further post processing. A complementary application was developed to

analyze the result of the simulations. It processed simulated cell data and provided a real-time view for monitoring cell behavior. The interface displays temporal information on the spectral profile, input DNI, cloud condition, sub-cell IV characteristics, EQE and the instantaneous and cumulative energy output. An illustration is provided in Figure 4-9.

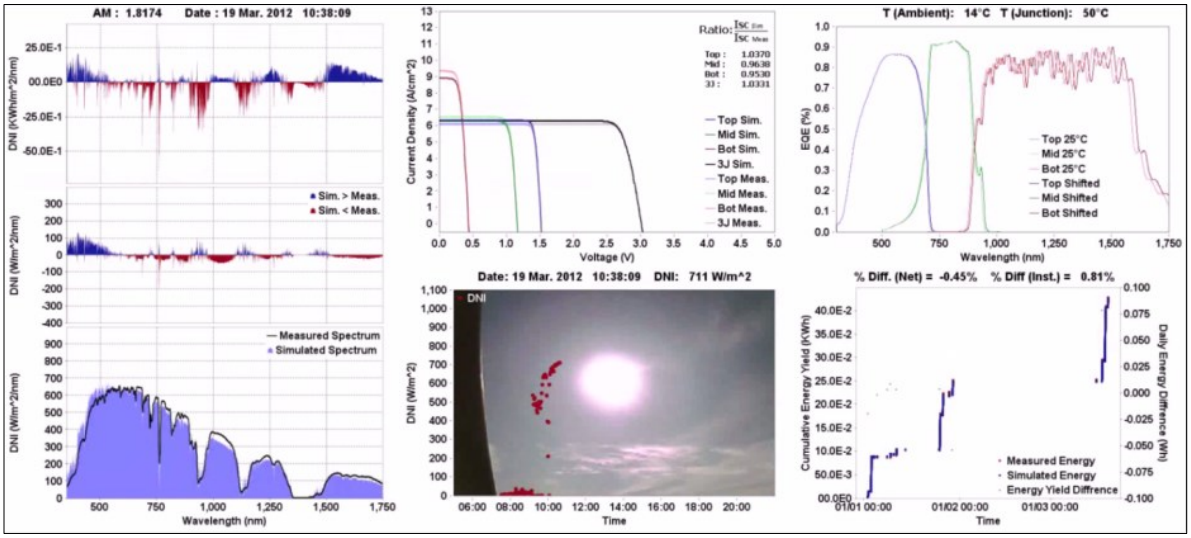

Figure 4-9: Sample media illustrating the operation of a data plotting application developed to aid analysis of simulated cells stored in a database.

4.2.2.1 Energy Yield Model Validation

Validation of the energy yield model is necessary because majority of the analysis to be carried out depends on the models accuracy. Research at SUNLAB has led to the development of a method to parameterize temperature dependent characteristics of multi-junction solar cell isotype and preliminary results have been published [64]. A quantum dot enhanced solar cell, with a unique EQE modified to optimize efficiency for a given air mass, was used for this analysis. Figure 4-10 presents the EQE profile of the solar cell.

Using the equations provided by Sakurada *et al.* [31] and Varshni [32], temperature-dependent dark IV curves were recorded for each sub-cell isotype using the SUNLAB's Oriel station [64]. Measurements were taken for 20˚C, 25˚C, 30˚C, 40˚C, 50˚C, 60˚C and 70˚C. A fit algorithm that varied the saturation and non-recombination components of the dark current was subsequently used to search through a two diode cell equation to determine the equivalent parameters that corresponded to the cell characteristics for the range of temperature measurements. Specified and measured cell material parameters to model the sub-cells are presented in Table 6 below.

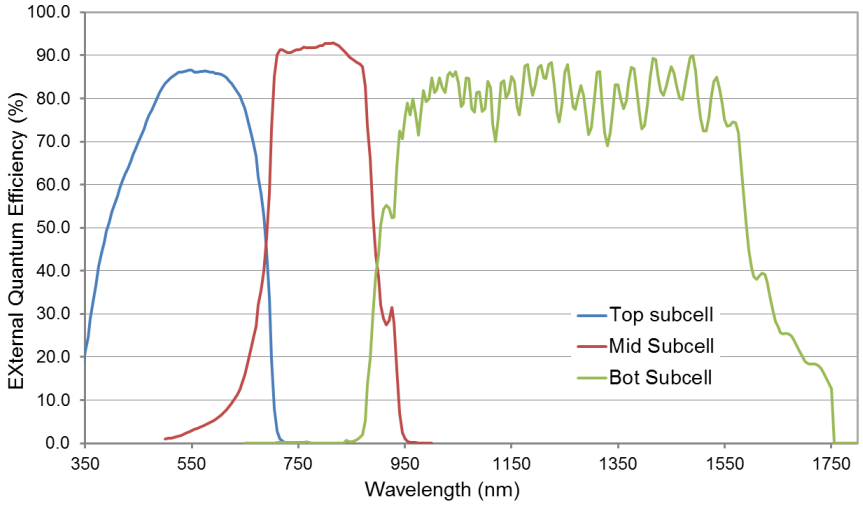

Figure 4-10: External quantum efficiency (EQE) of a multi-junction solar cell being used for the subsequent analysis. The top sub-cell is made up of Aluminum Gallium Indium Phosphide (AlGaInP), the middle sub-cell is made up of Indium Gallium Arsenide (InGaAs) infused with quantum dots and bottom sub-cell is made up of Germanium (Ge).

Parameters	Top Sub-cell	Middle Sub-cell	Bottom Sub-cell
Eg @ 0K (eV)	1.879	1.519	0.750
Eg @ 25˚C (eV)	1.7967	1.4233	0.6705
α (eV/K)	6.00E-4	5.41E-4	4.77E-4
β (K)	350.0	204.0	235.0
R_s (Ω)	9E-7	9E-7	9E-7
R_{sh} (Ω)	1E4	1E4	1E4
Saturation Factor	4.77E-26	38.07E-20	2.394E-7
Recombination Factor	1.43E-4	1.85E-10	4.8E-5

Table 6: Cell parameters, specified and generated for modeling cell IV characteristics using temperature dependent calculations based on the Varshni relation. Eg is the sub-cell band gap, α and β are semiconductor material properties, R_s and R_{sh} are series and shunt resistance respectively.

Light IV curves were taken from a triple junction solar cell with internal sub-cell characteristics similar to the characterized isotypes for various temperatures and light intensity on the Oriel station as presented on Table 7. Spectra with intensities specified in Table 7 were input to the cell simulation model, using the temperatures and the parameters specified above. The results of the simulation are presented for comparison with the measured IV curves in Figure 4-11 below. It shows good agreement between measured and simulated IV curves for different temperatures and light intensities. The cell simulation model is the foundation of the energy yield analysis used in the following assessment.

Input Label	Temperature (˚C)	Concentration (suns)
Sample 1	37.2	2.59
Sample 2	37.9	2.82
Sample 3	38.5	3.06
Sample 4	39.1	3.32
Sample 5	39.1	3.54

Table 7: Input sample parameters for validating the cell simulation.

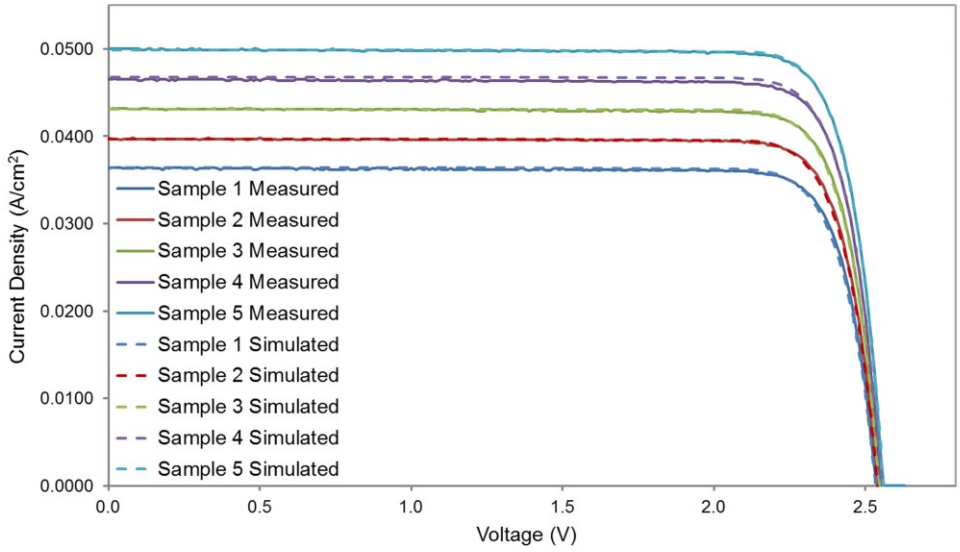

Figure 4-11: Comparison of measured and simulated temperature dependent IV curves. We note the similarity of the temperature matched simulated curve to the measured curve which validates the models performance. Adapted from [64].

4.2.2.2 Energy Yield Model Comparison

The primary cause of spectral variation is the temporally evolving air mass, on which all components of the atmosphere depend. The effect of air mass on DNI spectra was earlier illustrated in Figure 2-12. Incorporating change in air mass and temperature, an investigation was made to determine the difference in energy yield analyses between a simple model (based on an efficiency-energy product) and a more sophisticated model (described above in section 4.2.2.1). The multi-junction cell calibrated in section 4.2.2.1 was optimized for the American Standard for Testing and Material standard spectrum (ASTM) known as ASTM G173, which has an overall rating of 900W/m^2. Under Standard Test Conditions (STC), the multi-junction cell has been measured and its efficiency is noted to be 30.6%.

Using the SMARTS2 simulator with parameters set for the ASTM G173 spectrum, DNI spectra were generated for air mass values between AM1 and AM12 (subsequently translated into nominal time of day) as model inputs. The model results, as electrical power curves, are presented in Figure 4-12 (right axis); the integrated DNI are shown for reference (left axis). The results of the simple model (red curve) are clearly directly proportional to the DNI (as expected for an efficiency-power product). The more rigorously accurate model (green curve) departs from DNI scaling.

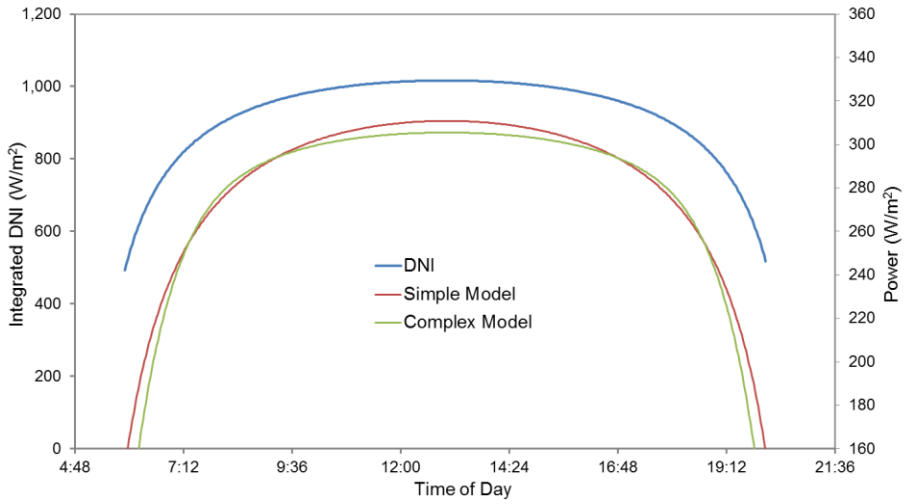

Figure 4-12: Modeled triple-junction cell output using a simple and complex model. The simple model result is directly proportional to the input power but the complex model efficiency varies.

Due to spectral mismatch between sub-cells for the range of air mass inputs, the overall efficiency of the cell changes with the incident spectrum profile. In Figure 4-12, for early morning and late evening periods the cell efficiency is lower than the STC rating due to the higher proportion of long wavelength radiation in the spectra. Later in the morning (and earlier in the evening), at air mass values close to AM1.5, the cell efficiency matches the STC rating and minimal difference is expected between the simple and complex models, as is seen. The variation in cell efficiency with time of day (air mass) is shown in Figure 4-13 (left axis: black diamonds and solid line) – note the reduction in cell efficiency near zenith. This is due to increasing domination by shorter wavelength components of the incident spectrum – as shown by the subcell current curves, the cell goes from top subcell (blue curve) limiting at high air mass to middle subcell (green curve) limiting at low air mass. Since the bottom subcell always overproduces (red curve), the resulting cell current production (dashed black curve) tracks the competition between top and middle subcells.

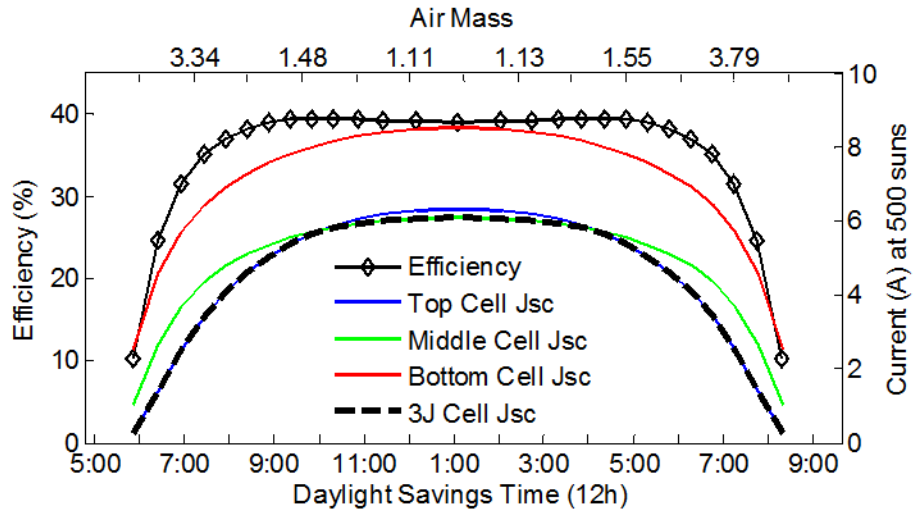

Figure 4-13: Modeled cell efficiency as a function of time of day (air mass). We note the different current profiles for the top and middle sub-cells that limit the cell current at various points of the day [15].

Temperature variation also affects cell efficiency due to the reduction in subcell band gap energies with increasing temperature that drives changes the EQE profile. Figure 4-14 presents the cell efficiencies calculated with the complex model as a function of ambient temperature. The ambient temperature ($T_{ambient}$) was determined from the junction temperature ($T_{junction}$) for each particular efficiency by assuming a linear relationship between junction temperature and DNI as given by

$$T_{junction} = \left(\frac{DNI*50}{1000}\right) + T_{ambient}\ , \tag{41}$$

where each increase in concentration by one sun leads to an increase of 50˚C in $T_{junction}$.

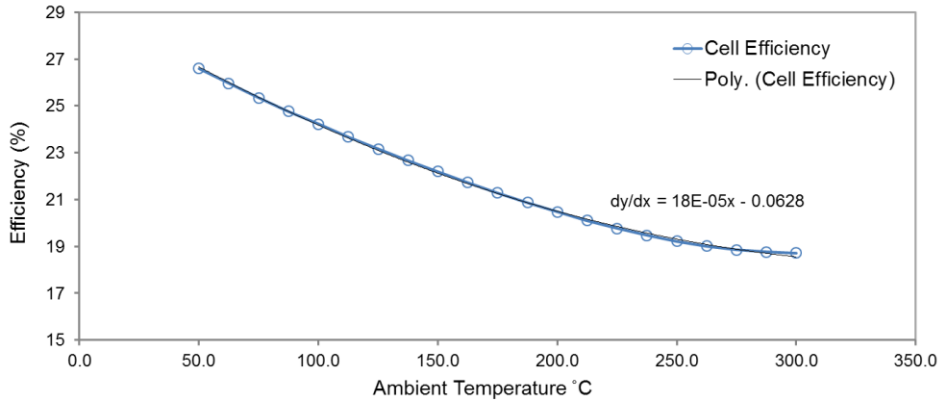

Figure 4-14: Modelled efficiency as a function of ambient temperature for a triple junction solar cell. The temperature range is exaggerated to illustrate the gradual slope of the curve.

Considering solely variations in air mass and ambient temperature, a comparison between energy yields calculated from simple and complex models was carried out using spectra simulated using SMARTS2 (using fixed ASTM G173 parameters), scaled to the integrated DNI measured with the pyranometer over the range of air mass values present in the APECS dataset between June 2011 and July 2012. Calculated energy yields on two minute time intervals are presented in Figure 4-15. Blue and red dots are simple and complex model results, respectively. For each day there is a distribution of energies from near zero to some maximum because DNI varies with cloud cover and air mass; there are gaps in the time series due to instrumentation faults and maintenance. We note that the two models agree quite well for the winter period, when energy production is low, but that the simple model overestimates energy production during summer months, when energy production is high. Over the year, the total energy produced from the simple and complex models was 369.3 KWh and 357.7 KWh, respectively. The 3.2% overestimation by the simple model is purely due to the neglect of spectral variation driven by air mass and temperature. In so far as the DNI for that year may be assumed as typical, the degree of overestimation will also be typical. Clearly, summers with higher DNI will yield a greater overestimation, and cloudier summers a lesser overestimation. The point remains, however, that spectral variation must be accounted for in energy yield models to achieve predictions of CPV energy production to better than several percent accuracy.

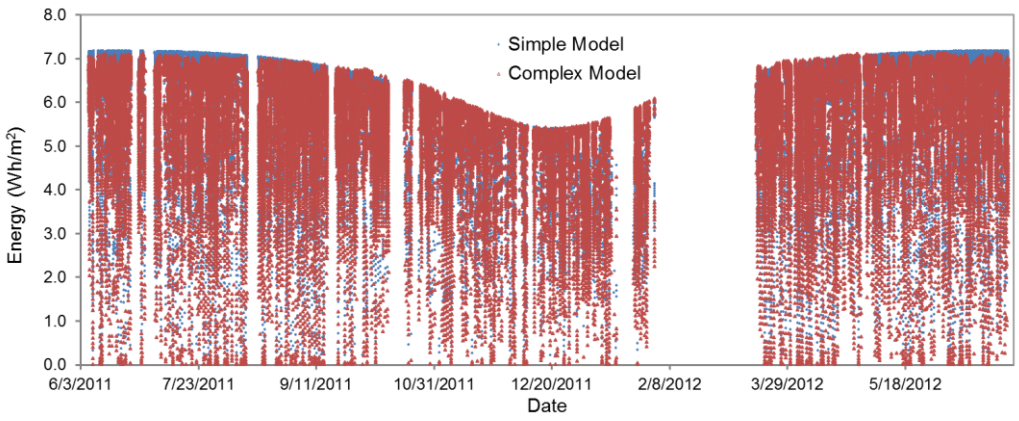

Figure 4-15: Highly temporal simulated energy yield using the simple and complex model. We note the marked difference in peak energy for the summer periods which correspond to high DNI.

4.2.2.3 Input Dataset Comparison

It is economically unviable to setup long term solar resource measuring instruments at all potential PV sites; hence, data used for long term energy yield analysis is often improvised. A comparison between measured DNI data from the APECS test site and simulated SMARTS2 spectrum using generic continental parameters (ASTM G173), typical meteorological year (TMY) datasets and historical datasets (CWEEDS) is presented. The exercise aims to determine the degree of accuracy for CPV energy yield analysis in Ottawa using various data reductions. This is necessary because, for most PV energy yield evaluation systems, TMY datasets are used as the data input for the temporal solar resource.

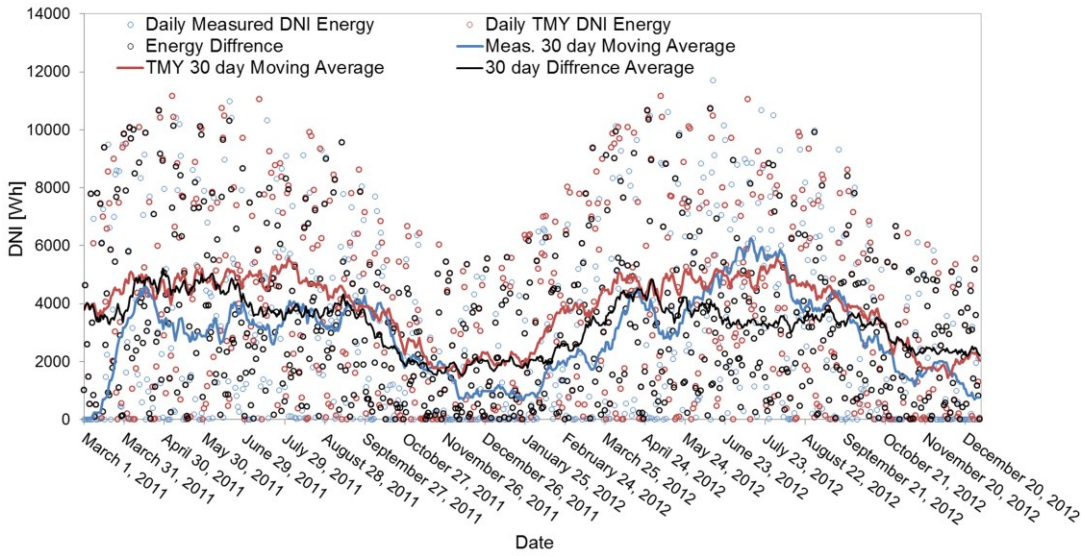

Figure 4-16: Comparison of the APECS measured DNI taken between March 2011 and December 2012 to the CWEC TMY dataset for the same time period. The Root Mean Square Deviation (RMSD) between the two dataset is 4179.6Wh and the total energy difference is ~25.4% where the TMY underestimates measured values.

Measured (blue) and TMY (red) DNI (in Wh) are presented in Figure 4-16, open symbols being daily values and solid lines a 30-day moving average. Several observations may be made: First, while broad seasonal trends are apparent in the daily values, there is extensive day-to-day variation between the two datasets (black symbols). Since the TMY dataset is not an average, but a representative dataset, these variations are typical of what one would expect between any two years. Note that the solid black line represents the average of the differences, not the difference of the average. Integrated over the year, the TMY data produces results 25.4% lower than would actually be obtained for the indicated time period.

Presumably a longer time series would reduce this difference, so further analysis was performed with a larger dataset.

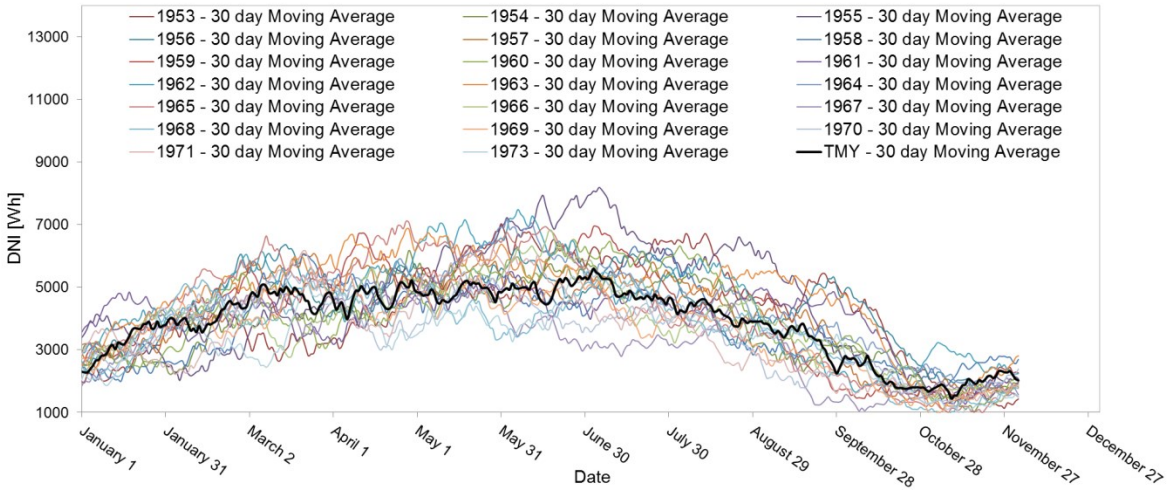

Figure 4-17: CWEC TMY plotted against 19 years of CWEEDS datasets between 1953 and 1972.

DNI (in Wh, as 30 day moving averages) from the CWECS TMY was compared with that from the CWEEDS historical dataset (from 1953 to 1970), as shown in Figure 4-17. The TMY dataset either underestimates or overestimates the CWEEDS dataset, depending on the time of year, but the multiyear trend is that CWECS TMY assessments underestimate energy predictions as compared with historical results. This is seen in Table 8, where the relative difference in energy production between multiyear average CWEEDS data is compared with CWECS TMY for 1, 5, 10, 15 and 20 year sample periods. The results suggest that climactic variability largely averages out on 5 to 10 year timescales, and that long term climactic variability (on 10 to 20 year timescales) may still yield fluctuations in energy yield at ~0.5% level. The major finding, however, is that using the CWECS TMY dataset for long term prediction leads to about a 7% underestimation in energy yield.

TMY Years	CWEEDS Year(s)	Difference (%)
1	1955	15.97
2	1961, 1962	9.60
5	1953 - 1958	8.30
10	1953 - 1963	7.36
15	1953 - 1968	6.61
20	1953 - 1973	7.15

Table 8: Comparison between annual energy from TMY and CWEEDS over variable sample periods.

4.2.2.4 De-convolution of Meteorological Bias Factors Affecting CPV Energy Yield

Having confirmed the existence of bias due to spectral variation in CPV energy yield models, an analysis was carried out to determine the effect of various factors on CPV energy yield analysis. The experiment involved the use of datasets from (1) SMARTS2 simulated spectra scaled to measured DNI, (2) TMY spectra, (3) ASTM G173 spectra, (4) AM1.5D spectra scaled to ASTM G173 DNI, and (5) AM1.5D spectra scaled to measured DNI. These datasets, constructed at 2 minutes intervals, were input into the CPV energy yield model (discussed in section 4.2.2.1) and compared with the energy yield produced from the measured spectral DNI of the APECS dataset. Figure 4-18 presents a block diagram to illustrate the comparison process.

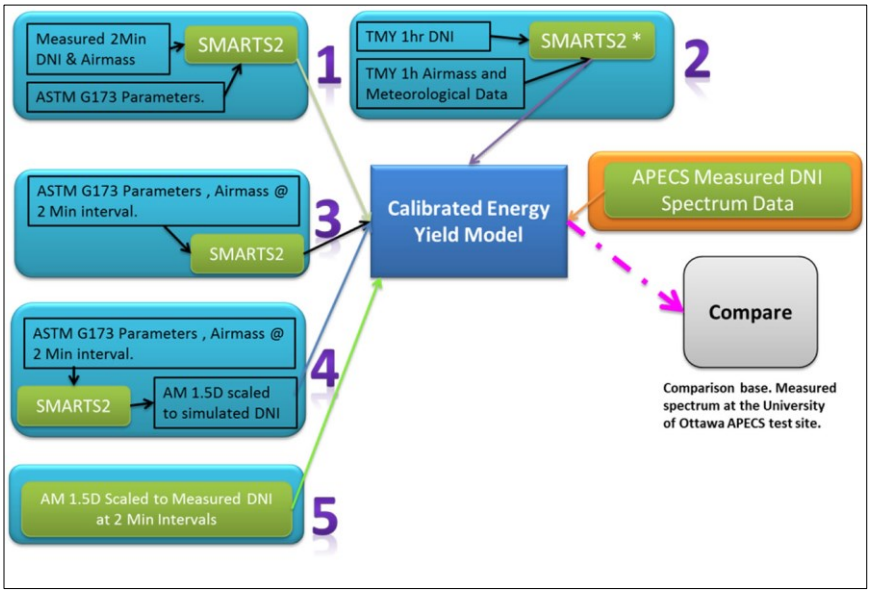

Figure 4-18: Block diagram illustrating the data input types for comparison against measured DNI spectra.

Results from the simulations using the various inputs were used to de-convolute the factors that affect energy yield. Dataset 1 allows for the de-convolution of the effects of spectral variation due to aerosols and perceptible water vapour. The sample data takes into consideration air mass, and insolation loss due to cloud cover. Dataset 2 de-convolutes the effect of overestimated or underestimated cloud cover. Dataset 3 neglects the effect of cloud cover on solar insolation and in conjunction with dataset 4 aids to de-convolute the full effect of spectral variations due to air mass change. Dataset 5 complements the result from dataset 1 to de-convolute the effect of air mass induced spectral variations.

The energy yield model was executed with an OTF profile of unity across all wavelengths for data inputs generated or measured at two minutes intervals between June 2011 and August 2012. Omissions were made where data were unavailable in the APECS dataset (see Figure 2-30). Figure 4-19 presents the cumulative energy from the simulations. We note that the TMY based energy assessment markedly underestimates all other assessments. This is consistent with the results presented in section 4.2.2.3.

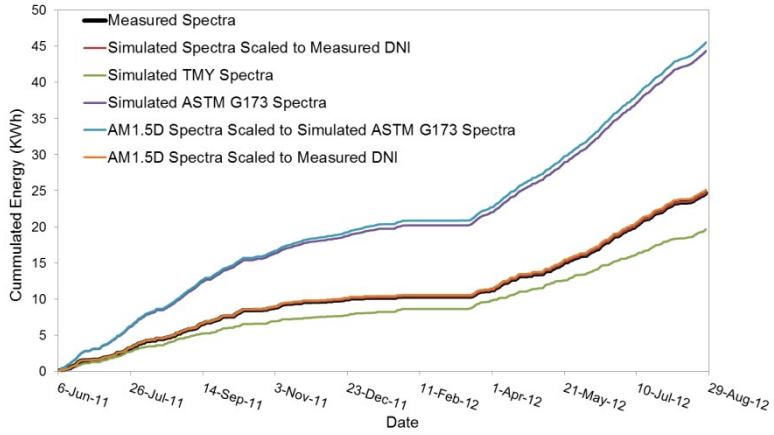

Figure 4-19: Cumulative energy profiles of CPV energy yield analysis using various dataset input with a flat OTF profile with 100% transmission.

Table 9 below summarizes the percentage difference in energy yield between measured and simulated datasets (negative values implying an overestimation by the latter). An energy assessment based on Dataset 1, which incorporates all but meteorological variability (continental averages are used for aerosols, humidity, etc in SMARTS2), overestimates energy production by only 0.42%, implying that the input and model appropriately capture almost all of the spectrally induced variability; note that cloud cover is accounted for in the DNI scaling. The gross underestimation by the TMY dataset, of some 20%, is consistent with our earlier analysis in section 4.2.2.3 and is indicative of year-to-year variability in energy production. Datasets 3 and 4, which primarily neglect cloud effects, demonstrate the strong sensitivity of CPC energy yield to clouds, and imply that the APECS site was cloudy for at least 60% of the time. The difference between datasets 3 and 4 is that the latter also neglects spectral variation, the difference implying that its neglect overestimates energy production by 2.44%. This is consistent with the difference between datasets 1 and 5 (both of which account for clouds through DNI scaling, but the latter neglects spectral variation), at 1.55%.

Label No	Data set	Difference (%)
1	Simulated spectra scaled to Measured DNI	0.42
2	Simulate TMY spectra	-20.34
3	Simulated ASTM G173 spectra	60.71
4	AM1.5D spectra scaled to simulated spectra	63.15
5	AM1.5D spectra scaled to measured DNI	1.97

Table 9: CPV energy yield difference measured and various data sets input. An OTF of 100% transmission was assumed for the simulation.

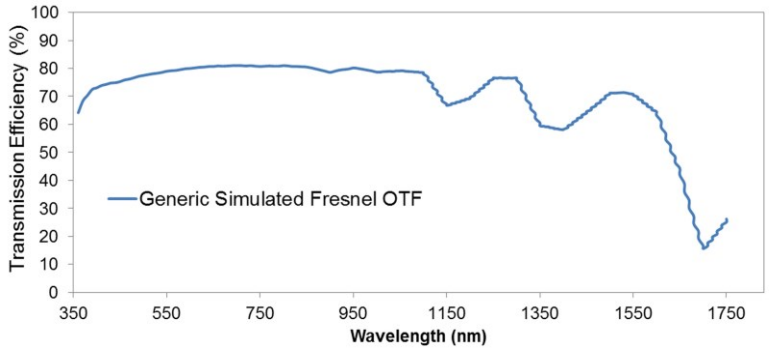

Figure 4-20: Zemax simulated optical transfer function for a generic Poly (methyl methacrylate) (PMMA) Fresnel lens.

To further validate our analysis, a generic OTF based on the simulated optical transmission through a PMMA Fresnel lens (Figure 4-20) was introduced into the CPV model and the simulations as described above were repeated. The inclusion of the Fresnel lens introduced a spectral bias in the current matching between sub-cells. Since the simulated cell model was not now tuned for the input OTF, the overall effects of spectral mismatch for all data sets should be more pronounced.

Results for the simulations with and without OTF are presented in Table 10. For ease of comparison, the input datasets have been categorized by the factors that are being deconvoluted: (A) spectral variations due to meteorological effects such as aerosols and perceptible water vapour; (B) loss of DNI due to cloud cover; and (C) spectral variations due to air mass. Neglecting the underestimating TMY energy assessment, the overestimation in energy production has been increased, on average by some 0.3%, in agreement with expectations.

Input Spectrum Dataset	A Meteorological Effects	B Cloud Cover Effects	C Airmass Effects	Difference Without OTF	Difference With OTF
Measured Spectra	✓	✓	✓	-	-
1 Smulated spectra scaled to measured DNI	✗	✓	✓	0.42%	0.53%
2 Simulated spectra using TMY parameters	✓	✓	✓	-20.34%	-20.49%
3 Simulated spectra using ASTM G173 parameters	✗	✗	✓	60.71%	60.92%
4 AM 1.5D Scaled to simulated spectra using ASTM G173 parameters	✗	✗	✗	63.15%	63.65%
5 AM 1.5D Scaled to Measured DNI	✗	✓	✗	1.97%	2.39%

Table 10: Overview of simulation results under three conditions that affect spectral variation and the DNI resource.

The analyses confirms that an OTF increases the spectral sensitivity of CPV systems and hence it is the product of cell and optical train response that should be tuned to the optical spectrum. The results also confirm that over the sampling interval (~1 year), for the APECS test site in Ottawa, the neglect of spectral variation due leads to about a 2% overestimation of CPV energy yield. Furthermore, the results for input dataset 1 imply that the impact of aerosols and perceptible water vapour on energy yield is minimal. Finally, we can deduce from the analysis that the most important factor that contributes to bias in CPV energy yield analysis is the effect of cloud cover on DNI. This is noteworthy because it stipulates that location specific data for the temporal impact of cloud cover on DNI is absolutely necessary to accurately predict CPV energy yield.

5 Conclusions

A brief history of PV and CPV technology was presented and the need for PV as a sustainable source of renewable energy was highlighted. The solar resource and its source - the sun; was discussed in terms of its spectral distribution and relationship with the earth respectively. Equations and algorithms necessary to locate the sun spatially and temporally were presented.

Details of research and characterization tools developed by the author for use with solar demonstrators in the SUNLAB research group were discussed. Databasing procedures carried out to acquire and store highly temporal meteorological data for CPV analysis under the auspice of the APECS project were discussed.

A method to estimate the spectral distribution of the direct solar irradiance using meteorological data sets, a spectral simulation model (SMARTS2) and temporally measured DNI at a single wavelength (550 nm) was proposed and investigated. A CPV energy yield model was developed and analysis was performed using data measured at the APECS test site to determine factors that affect long term CPV energy yield analysis in Ottawa, Ontario, Canada.

5.1 Overview / Summary

In chapter one, the ever increasing demand for energy and the issue of environmental pollution as a result of fossil fuel consumption motivated research and development of PV energy technologies. Depleting non-renewable energy resources was highlighted as a cause for concern, and renewable PV generated electricity was proposed as an energy source that would aid sustainable development in the future. The history of PV systems from its dominance in extraterrestrial to terrestrial applications was discussed and its growth trend in terms of price and efficiency was highlighted. The learning curve for PV which went into full bloom for terrestrial use in 1976 was found to suggest that the price of PV would be less than a dollar per watt by 2015. The history of standardization processes generated to characterise various solar cell types was highlighted.

CPV technologies that promise cheaper energy systems were reported to have achieved about 44% cell efficiencies. Unlike PV, which shows little scope for future improvement, the

trend in efficiency growth for CPV is still strong. The basic operation of CPV cells were contrasted with PV cells, with the enhancement in efficiency due to the multi-junction architecture responsible for absorbing larger portions of the solar resource. The major issues that negatively impact CPV (relative to PV), such as DNI-specificity and spectral mismatch, were discussed.

In chapter two, the nature of the spectral distribution of the extraterrestrial solar resource was discussed. The earth-sun temporal relationship was described and algorithms for calculating precise coordinates of the sun from the earth's surface spatially and temporally were presented. Knowledge of elevation angles were necessary for calculating the air mass as a precursor for simulating the temporal atmospheric transmission of sunlight through the atmosphere. The algorithm also provide a method for calculating azimuthal and elevation angles necessary for tracking the dual axis trackers used for CPV systems. Instrumentation for measuring components of the solar resource were reviewed and notable CPV installations were presented.

In chapter three, PV and CPV research within the uOttawa SUNLAB was highlighted, and hardware tools, such as the high concentration XT-30 solar demonstrator and the temperature controlled low concentration Oriel test station, were described. Software tools developed by the author to characterise and test solar systems were discussed. The tools included a pluggable IV testing utility, a spectral and spatial cell uniformity measurement system and a light cycling utility.

The architecture for high temporal granularity data measurement and databasing within the APECS project was presented. The datasets acquired were DNI, GHI, spectral DNI, cloud cover and ambient temperature; the measuring instruments used were an Eppley NIP pyrheliometer, Eppley PSP pyranometer, ASDi spectroradiometer and a CCD camera. Ongoing measurements for each dataset began at various times in 2011 and were carried out at 2 minutes intervals. A dedicated server was setup to record, store and publish the data sets (http://www.apecs.site.uottawa.ca). A model for simulating the detailed IV characteristics of a solar cell based on the diode equation [31] and Varshni relation [32] was presented. The calculations were used to develop a java application for modelling PV systems.

In chapter four, investigations were carried out to assess the impact of using single wavelength optical depth values on the accuracy of the simulation of the solar resource. The

extraction of an aerosol optical depth from measured data was input to an atmospheric radiative transfer model (SMARTS2) and the result validated against measured spectra from the APECS test site. The results were used in a triple-junction cell model to predict short circuit currents and a bias of ~0.6% between measured spectra and spectra was shown. It was noted that the model is only valid for clear sky conditions.

Investigation of methods and datasets used for CPV energy yield analysis was performed. Data from the CPV energy yield model was verified against measurements and the result were in good agreement. Comparison was carried out between a simple and complex model for CPV energy yield and the results suggested that the simple model overestimates annual energy yield by ~3%. This was attributed to the neglect of spectral and temperature variation in the simple model.

Using historical data sets from CWEEDS, the CWECS TMY dataset often used for PV energy yield analysis was investigated. A comparison was carried out to determine the overall energy bias against 1, 5, 10, 15 and 20 year CWEEDS energy yield assessments. The results were that the CWECS TMY dataset still underestimated long term (> 5 years) energy yields by about 7%.

An investigation was carried out to determine the degree to which certain factors influence CPV energy yield. Five different spectral models, each neglecting one or more significant factors, were compared against each other and measured spectra after their input into the CPV energy yield model, both with and without an OTF. The results showed that for the duration of the analysis (~1 year), and the specific location of the reference data (Ottawa), the neglect of spectral variation (due to air mass) gave a ~2% overestimation in CPV energy yield. Similarly, the neglect of spectral variation due to aerosol optical depth and perceptible water vapour had a minimal impact on energy yield estimates, overestimations of 0.42% and 0.53%, without and with an OTF, respectively. As expected, the results verified that an OTF increased the bias in CPV energy yield analysis. The most prominent contributor to CPV energy yield analysis was found to be cloud cover, at about the 60% level. The results suggest that for accurate CPV energy yield prediction, the input dataset must be one that addresses cloud cover.

5.2 Future Work

The attempt to generate spectral measurements from single-parameter AOD measurements, as presented in section 4.1, showed promise of viability. However, the approach used was based on the assumption of a constant AOD value for morning and evening periods, in contrast to what was actually observed. Opposed to the calculations presented where OD was assumed to change linearly with air mass, in reality, the rate of change of OD with air mass is non-linear. In Figure 5-1 below, the log of measured DNI irradiance at 500 nm on a clear sky day was plotted against air mass for the morning period. We note the non-linear profile of the curve that corresponds to a constant change of OD with air mass. A polynomial of the 3rd order was fitted to the filtered data, which suggests that an algorithm equivalent to equation (40) could be developed to resolve temporal OD. Future work on this subject is required to determine the algorithm needed to apply temporal AOD to the spectral generator (SMARTS2). Further work is also required in investigating methods to improve the spectrum estimation model. One such method could involve the use of multiple extracted AOD at different wavelengths for different segments of the spectrum.

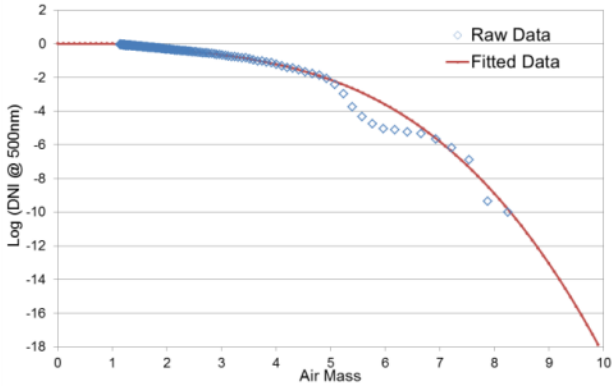

Figure 5-1: Natural logarithm of the DNI at 500nm measured on the 3rd of May 2013, plotted against morning air mass. A 3rd order polynomial was fitted to the filtered data and plotted. The polynomial fit provides a means to resolve temporal OD.

The APECS project is continuing and a test site is being established in Littlerock, California, USA. Possible future work would involve the development of database architecture similar in design to the Ottawa test site to investigate site-specific responses to a markedly different local solar resource (higher DNI, little cloud cover).

In section 4.2 the experiments conducted determined that not all assumptions that hold true for PV energy yield analysis do the same in CPV energy analysis. A task that is of

considerable interest for future work is the development of an interactive computer software application to aid decision making for economic and financial circumstances in siting, financing and maintaining CPV systems for grid connected electricity production. Such a system would leverage the detailed CPV simulation model developed to perform energy yield analysis and would complement the PV applications RetScreen and PVwatts. The application would use measured data from multiple sources to minimize the LCOE and maximizing Return on Investment (ROI).

6 References

[1] I. Dincer, "Renewable energy and sustainable development: a crucial review," *Renew. Sustain. Energy Rev.* **4** (2), pp. 157–175, Jun. 2000.

[2] J. E. Cohen, "Human population: the next half century," *science* **302** (5648), pp. 1172–1175, 2003.

[3] G. M. Masters, *Renewable and efficient electric power systems*. Wiley-Interscience, 2005.

[4] M. Harper, "Sustainable and Renewable Energy Development in Ontario : A look at the Current Policy Frameworks and Discourses Surrounding Sustainable Energy and Wind and Solar Power in Major Ontario Newspapers Sustainable and Renewable Energy Development in Ontario : ," **5** (1), 2009.

[5] J. Butlin, "Our common future. By World commission on environment and development. (London, Oxford University Press, 1987, pp.383 £5.95.)," *J. Int. Dev.* **1** (2), pp. 284–287, 1989.

[6] E. Bequerel, "Recherches sur les effets de la radiation chimique de la lumière solaire, au moyen des courants électriques," *CR Acad. Sci* **9**, pp. 145–149, 1839.

[7] A.-E. Becquerel, "Mémoire sur les effets électriques produits sous l'influence des rayons solaires," *Comptes Rendus* **9** (567), p. 1839, 1839.

[8] Wikipedia, "A. E. Becquerel --- Wikipedia, The Free Encyclopedia." 2013.

[9] C.-T. Sah, R. Noyce, and W. Shockley, "Carrier Generation and Recombination in P-N Junctions and P-N Junction Characteristics," *Proceedings of the IRE* **45** (9), pp. 1228–1243, 1957.

[10] W. Shockley, "The theory of pn junctions in semiconductors and pn junction transistors," *Bell Syst. Tech. J* **28** (3), pp. 435–489, 1949.

[11] C. A. Wolden, J. Kurtin, J. B. Baxter, I. Repins, S. E. Shaheen, J. T. Torvik, A. A. Rockett, V. M. Fthenakis, and E. S. Aydil, "Photovoltaic manufacturing: Present status, future prospects, and research needs," *J. Vac. Sci. Technol., A* **29** (3), p. 30801, 2011.

[12] M. A. Green, "Silicon photovoltaic modules: a brief history of the first 50 years," *Prog. Photovolt. Res. Appl.* **13** (5), pp. 447–455, 2005.

[13] A. McEvoy, T. Markvart, L. Castañer, T. Markvart, and L. Castaner, *Practical Handbook of Photovoltaics: Fundamentals and Applications: Fundamentals and Applications*. Elsevier Science, 2003.

[14] A. Goetzberger, C. Hebling, and H.-W. Schock, "Photovoltaic materials, history, status and outlook," *Materials Science and Engineering: R: Reports* **40** (1), pp. 1–46, Jan. 2003.

[15] M. Yandt, "Characterization and Performance Analysis of High Efficiency Solar Cells and Concentrating Photovoltaic Systems," University of Ottawa, 2012.

[16] D. Matin, "A Steeper Learning Curve for PV," 2011. [Online]. Available: http://www.interpv.net/market/market_view.asp?idx=94&part_code=03. [Accessed: 16-Apr-2013].

[17] K. Mitchell, C. Eberspacher, J. Ermer, and D. Pier, "Single and tandem junction CuInSe2 cell and module technology," in *Conference Record of the Twentieth IEEE Photovoltaic Specialists Conference*, 1988, **1**, pp. 1384–1389.

[18] "Solar cell prices dropping, but broad terrestrial use awaits mass production," *Electronics*, pp. 40–41, 19-Jul-1973.

[19] L. M. Magid, "The current status of the US photovoltaic conversion program," in *12th Photovoltaic Specialists Conference*, 1976, **1**, pp. 607–612.

[20] Y. Poissant, "Status and Trends of PV Technology in Canada," *Next Generation Solar 2013 Conference*. [Online]. Available: http://www.youtube.com/watch?v=W-I5RN2d31c.

[21] E. Christensen, "Electricity from photovoltaic solar cells. Flat-Plate Solar Array Project of the US Department of Energy's National Photovoltaics Program: 10 years of progress," *NASA STI/Recon Technical Report N* **88**, p. 12188, 1985.

[22] J. Perlin, *From space to earth: the story of solar electricity*. Earthscan, 1999.

[23] M. R. Mack, "Solar power for telecommunications," *Telecommunication Journal of Australia* **29**, pp. 20–44, 1979.

[24] Nrel, "Best Research - Cell Efficiencies," 2013. [Online]. Available: http://www.nrel.gov/ncpv/images/efficiency_chart.jpg. [Accessed: 16-Apr-2013].

[25] "What is sustainable development? Environmental, economic and social well-being for today and tomorrow." [Online]. Available: http://www.iisd.org/sd/. [Accessed: 16-Apr-2013].

[26] G. Raisbeck, "The Solar Battery," *Scientific American* **193**, pp. 102–110, 1955.

[27] H. Fischer and W. Pschunder, "Low-cost solar cells based on large-area unconventional silicon," *IEEE T. Electron. Dev.* **24** (4), pp. 438–442, Apr. 1977.

[28] J. S. Li and G. Q. Chen, "Energy and greenhouse gas emissions review for Macao," *Renew. Sustain. Energy Rev.* **22**, pp. 23–32, 2013.

[29] A. Goetzberger and C. Hebling, "Photovoltaic materials, past, present, future," *Sol. Energ. Mat. Sol. C.* **62** (1), pp. 1–19, 2000.

[30] G. S. Kinsey and K. M. Edmondson, "Spectral response and energy output of concentrator multijunction solar cells," *Prog. Photovolt. Res. Appl.* **17** (5), pp. 279–288, 2009.

[31] Y. Sakurada, Y. Ota, and K. Nishioka, "Simulation of Temperature Characteristics of InGaP/InGaAs/Ge Triple-Junction Solar Cell under Concentrated Light," *Jpn. J. Appl. Phys.* **50** (4), p. 04DP13, 2011.

[32] Y. P. Varshni, "Temperature dependence of the energy gap in semiconductors," *Physica* **34** (1), pp. 149–154, 1967.

[33] W. W. Weiss, *Solar heating systems for houses: a design handbook for solar combisystems*. James & James Science Publishers, 2003.

[34] K. Rajeshwar, R. D. McConnell, and S. Licht, *Solar hydrogen generation: toward a renewable energy future*. Springer Science+ Business Media, 2008.

[35] R. L. Kurucz and E. H. Avrett, "Solar spectrum synthesis. I. A sample atlas from 224 to 300 nm," *SAO Special Report* **391**, 1981.

[36] B. Suresh, S. Schlag, and Y. Inogucji, "Chemical economics handbook marketing research report," *SRI Consulting*, 2004.

[37] J. Fontenla, O. R. White, P. A. Fox, E. H. Avrett, and R. L. Kurucz, "Calculation of solar irradiances. I. Synthesis of the solar spectrum," *The Astrophysical Journal* **518** (1), p. 480, 1999.

[38] R. L. Kurucz, "SYNTHE spectrum synthesis programs and line data," *Kurucz CD-ROM, Cambridge, MA: Smithsonian Astrophysical Observatory,| c1993, December 4, 1993* **1**, 1993.

[39] F. Vignola, J. Michalsky, and T. Stoffel, *Solar Resource Instrumentation*. CRC Press, 2012.

[40] Wikipedia, "Equation of time --- Wikipedia, The Free Encyclopedia." 2013.

[41] E. C. McCullough and W. P. Porter, "Computing clear day solar radiation spectra for the terrestrial ecological environment," *Ecology*, pp. 1008–1015, 1971.

[42] "NOAA Solar Calculator." [Online]. Available: http://www.esrl.noaa.gov/gmd/grad/solcalc/. [Accessed: 04-May-2013].

[43] R. A. Rohde, "Radiation Transmitted by the Atmosphere," *http://www.globalwarmingart.com/*, 2007. [Online]. Available: http://www.globalwarmingart.com/wiki/File:Atmospheric_Transmission_png. [Accessed: 16-Apr-2013].

[44] Emcore, "Utility-Scale Concentrator Photovoltaic (CPV) System," 2011. [Online]. Available: www.emcore.com%2Fwp-content%2Fthemes%2Femcore%2Fpdf%2FGen%2520III_2011.pdf.

[45] P. J. Verlinden and J. B. Lasich, "Energy rating of Concentrator PV systems using multi-junction III--V solar cells," in *Photovoltaic Specialists Conference, 2008. PVSC'08. 33rd IEEE*, 2008, pp. 1–6.

[46] P. Mints, "Solar electricity: 2009 surprise success," *Renewable Energy Focus* **11** (3), pp. 42–47, May 2010.

[47] SolFocus, "SolFocus Concentrator Photovoltaic (CPV) Systems," *Energy*, 2010. [Online]. Available: http://www.solfocus.com/en/downloads/sustainability/sustainability-flyer.pdf. [Accessed: 16-Apr-2013].

[48] J. Jaus, G. Peharz, A. Gombert, J. Rodriguez, F. Dimroth, F. Eltermann, O. Wolf, M. Passig, G. Siefer, A. Hakenjos, and others, "Development of Flatcon® modules using secondary optics," in *Photovoltaic Specialists Conference (PVSC), 2009 34th IEEE*, 2009, pp. 1931–1936.

[49] SolFocus, "Featured SolFocus Deployments," 2011. [Online]. Available: http://www.solfocus.com/en/installations/. [Accessed: 16-Apr-2013].

[50] M. Wilkins, R. Beal, J. E. Haysom, J. F. Wheeldon, P. Mulet, G. Jamieson, N. Youssef, D. Balachandreswaran, J. Fan, T. Hall, and others, "Design of a multiplexer to characterize individual optics at a concentrating photovoltaic test site," in *Photonics North 2011*, 2011, p. 800725.

[51] Eppley Inc, "Precision Spectral Pyranometer." [Online]. Available: http://www.eppleylab.com/PrdPrecSpectralPyrmtr.htm. [Accessed: 16-Apr-2013].

[52] L. Harrison and J. Michalsky, "Objective algorithms for the retrieval of optical depths from ground-based measurements.," *Applied optics* **33** (22), pp. 5126–32, Aug. 1994.

[53] L. T. Wong and W. K. Chow, "Solar radiation model," *Applied Energy* **69** (3), pp. 191–224, Jul. 2001.

[54] C. Gueymard, *SMARTS2: a simple model of the atmospheric radiative transfer of sunshine: algorithms and performance assessment*. Florida Solar Energy Center Cocoa, FL, 1995.

[55] F. Kasten, "A new table and approximation formula for the relative optial air mass," *Theoretical and Applied Climatology*, 1965.

[56] R. R. King, D. C. Law, K. M. Edmondson, C. M. Fetzer, G. S. Kinsey, H. Yoon, R. A. Sherif, and N. H. Karam, "40% efficient metamorphic GaInP/ GaInAs/ Ge multijunction solar cells," *Appl. Phys. Lett.* **90**, p. 183516, 2007.

[57] S. Kurtz, "Opportunities and challenges for development of a mature concentrating photovoltaic power industry (revision)," 2012.

[58] B. Prior and C. Seshan, "Concentrating Photovoltaics 2011: Technology, Costs and Markets," *GreenTech Media Market Research Report*, 2011.

[59] P. Perez-Higueras, E. Munoz, G. Almonacid, and P. G. Vidal, "High Concentrator PhotoVoltaics efficiencies: Present status and forecast," *Renew. Sustain. Energy Rev.* **15** (4), pp. 1810–1815, 2011.

[60] F. Dimroth, C. Baur, A. W. Bett, M. Meusel, and G. Strobl, "3-6 junction photovoltaic cells for space and terrestrial concentrator applications," in *Photovoltaic Specialists Conference, 2005. Conference Record of the Thirty-first IEEE*, 2005, pp. 525–529.

[61] G. S. Kinsey, W. Bagienski, A. Nayak, M. Liu, R. Gordon, and V. Garboushian, "Advancing Efficiency and Scale in CPV Arrays," *IEEE J. Photovolt.* **3** (2), pp. 873–878, Apr. 2013.

[62] M. Campbell, "LEVELIZED COST OF ENERGY FOR UTILITY-SCALE PHOTOVOLTAICS," *Solar Cells and Their Applications* **217**, p. 251, 2010.

[63] C. A. Gueymard and S. M. Wilcox, "Spatial and temporal variability in the solar resource: Assessing the value of short-term measurements at potential solar power plant sites," 2009.

[64] M. D. Yandt, J. F. Wheeldon, J. Cook, R. Beal, A. W. Walker, O. Thériault, H. Schriemer, T. J. Hall, and K. Hinzer, "Estimating cell temperature in a concentrating photovoltaic system," in *AIP Conference Proceedings*, 2012, **1477**, p. 172.